Aus dem Institut für Humangenetik
der Universität zu Köln
Direktorin: Universitätsprofessorin Dr. rer. nat. B. Wirth

# The role of AIS proteins ANKG and TRIM46 in TAU sorting and microtubule organization in human neuronal models

Inaugural-Dissertation zur Erlangung der Doktorwürde
der Medizinischen Fakultät
der Universität zu Köln

vorgelegt von
Helen Breuer
Aus Münster

promoviert am 08. Mai 2026

Gedruckt mit Genehmigung der Medizinischen Fakultät der Universität zu Köln
2026

Dekan: Universitätsprofessor Dr. med. G. R. Fink

1. Gutachterin: Universitätsprofessorin Dr. rer. nat. B. Wirth
2. Gutachter: Universitätsprofessor Dr. med. T. van Eimeren

Erklärung

Ich erkläre hiermit, dass ich die vorliegende Dissertationsschrift ohne unzulässige Hilfe Dritter und ohne Benutzung anderer als der angegebenen Hilfsmittel angefertigt habe; die aus fremden Quellen direkt oder indirekt übernommenen Gedanken sind als solche kenntlich gemacht.

Bei der Auswahl und Auswertung des Materials sowie bei der Herstellung des Manuskriptes habe ich Unterstützungsleistungen von folgenden Personen:

Dr. Dr. rer. nat. Hans Zempel
Dr. rer. nat. Michael Bell-Simons

Weitere Personen waren an der Erstellung der vorliegenden Arbeit nicht beteiligt. Insbesondere habe ich nicht die Hilfe einer Promotionsberaterin/eines Promotionsberaters in Anspruch genommen. Dritte haben von mir weder unmittelbar noch mittelbar geldwerte Leistungen für Arbeiten erhalten, die im Zusammenhang mit dem Inhalt der vorgelegten Dissertationsschrift stehen.

Die Dissertationsschrift wurde von mir bisher weder im Inland noch im Ausland in gleicher oder ähnlicher Form einer anderen Prüfungsbehörde vorgelegt.

Der Großteil in dieser Arbeit angegebenen Experimente sind von mir selbst ausgeführt und ausgewertet worden. Ausgenommen davon sind: die Zellkultur von iPSCs (insb. Frieren, Ausplattieren, Differenzierung) wurde von der medizinisch-technischen Assistentin Jennifer Klimek durchgeführt. Die iPSC-Erhaltung und experimentellen Verfahren an iPSCs (Fixierung, Färbung, Transfektion, Transduktion, Mikroskopie, qPCR) wurden von mir selbst durchgeführt. Die der Abbildung 5.2. zugrunde liegende Experimente (Zellkultur, Immunfluoreszenz, und Auswertung) der AIS-Entwicklung in primären Mausneuronen und SH-SY5Y-abgeleiteten Neuronen wurden von Michael Bell-Simons durchgeführt (entsprechend Abb. 5.2: A2, A3, B2, B3, in Teilen C), und waren Teil eines wissenschaftlichen Artikels, der an entsprechender Stelle zitiert wird.
Die der Abbildung 5.3. zugrunde liegende Experimente (Zellkultur, Immunfluoreszenz, und Auswertung) der axonalen TAU/MAP2-Sortierung in primären Mausneuronen, SH-SY5Y-abgeleiteten Neuronen (entsprechend Abb. 5.3: A3, A4) und iPSC-abgeleiteten Neuronen wurden von Michael Bell-Simons durchgeführt. Die Auswertung des AEF erfolge durch Michael Bell-Simons und mich (entsprechend Abb. 5.3: B). Die entsprechenden Daten waren Teil zweier wissenschaftlicher Artikel, die an entsprechender Stelle zitiert werden.

Erklärung zur guten wissenschaftlichen Praxis:

Ich erkläre hiermit, dass ich die Ordnung zur Sicherung guter wissenschaftlicher Praxis und zum Umgang mit wissenschaftlichem Fehlverhalten (Amtliche Mitteilung der Universität zu Köln AM 132/2020) der Universität zu Köln gelesen habe und verpflichte mich hiermit, die dort genannten Vorgaben bei allen wissenschaftlichen Tätigkeiten zu beachten und umzusetzen.

Köln, den 05.09.2025

Unterschrift: .....

# Danksagung

Ich möchte mich herzlich bei Michael Bell-Simons bedanken, der mein Projekt von den ersten Tagen im Labor bis zur letzten Korrektur des Manuskripts begleitet hat, für die geduldige Einarbeitung, klugen Rückmeldungen und gesellige Zusammenarbeit. Ich danke ebenfalls Hans Zempel für die enthusiastische Betreuung, dafür dass er bei Problemen oder Fragen immer zur Verfügung stand und mich stets motiviert hat meine Dissertation weiterzuentwickeln. Ich danke allen Mitgliedern der AG Zempel und AG Wirth, mit denen ich während meiner Promotion schöne und lustige Momente erleben konnte, darunter Jacqui, Lena, Jana, Michael, Sarah, Nadine, Aghyad, Çağla, Nur, Felix, Jenny, Daniel, Hanin und Thilo.

Ich danke außerdem meinen Freunden und meiner Familie für gemeinsame Uni-Tage, erfrischende Mittagspausen, unterstützende Telefonate und die nötige Ablenkung.

Für meine Eltern, Mona und Nele

# Table of contents

## List of abbreviations

+*TIP* *microtubule plus-end tracking protein*
-TIP *microtubule minus-end targeting protein*
0/1/2N *No (0N), one (1N) or two (2N) N-terminal inserts*
3/4R *Three (3R) or four (4R) C-terminal repeat domains*
3'UTR *three prime untranslated region*
AD *Alzheimer's Dementia*
ADL *activities of daily living*
$AEF_{MAP2}$ *Axonal enrichment factor for MAP2*
$AEF_{Tau}$ *Axonal enrichment factor for TAU*
AIS *axon initial segment*
AIS $EF_{ANKG}$ *AIS enrichment factor for ANKG*
AIS $EF_{TRIM46}$ *AIS enrichment factor for TRIM46*
ALS *Amyotrophic lateral sclerosis*
ANKG *Ankyrin G*
ANK3 *Ankyrin 3*
AP *action potential*
APP *Amyloid precursor protein*
ARIA *Amyloid-related Imaging Abnormality*
ASD *Autism spectrum disorder*
Aβ *Amyloid beta*
BDNF *brain-derived neurotrophic factor*
CAMs *cell adhesion molecules*
CAMSAP2 *Calmodulin Regulated Spectrin Associated Protein Family Member 2*
CBD *Corticobasal degeneration*
CDK5 *Cyclin-Dependent Kinase 5*
CLIP *Cytoplasmic linker protein*
CMT *Charcot-Marie-Tooth disease*
CNS *Central nervous system*
CSF *Cerebrospinal fluid*
CTE *chronic traumatic encephalopathy*
dX *day X after differentiation*
DAPI *4',6-diamidino-2-phenylindole*
DIV *days in vitro*
DMEM *Dulbecco's modified eagle medium*
DRG *dorsal root ganglion*
EB *end binding protein*
EMA *European Medicines Agency*
F.I. *arbitrary fluorescence intensity units*
fAD *familial Alzheimer's Dementia*
FTD *Frototemporal dementia*
FTDP-17 *Frontotemporal dementia and parkinsonism linked to chromosome 17*
GFP *green fluorescent protein*
GSK-3 *glycogen synthase kinase-3*
HEK *Human Embryonic Kidney*
HSP *Hereditary spastic paraplegia*
ICC *immunocytochemistry*
iPSC *induced pluripotent stem cell*
KIF3A kinesin family member 3A
KO *knockout*
MAPs *microtubule-associated proteins*
MARK *Microtubule Affinity-Regulating Kinase*
MCI *mild cognitive impairment*

MFI *mean fluorescence intensity*
MT *Microtubule*
MTBR *MT-binding region*
MTOC *microtubule organizing center*
Ndel1 *NudE Neurodevelopment Protein 1 Like 1*
NeuN. *Neuronal Nuclei, Fox-3, Rbfox3*
NFT *neurofibrillary tangles*
NF186 *neurofascin 186*
NGF *nerve growth factor*
NGN2 *Neurogenin 2*
NMDA *N-methyl-D-aspartate*
NMM *neuronal maturation medium*
NPC *neuronal precursor cell*
NSE Neuron-specific enolase
P-rich *Proline-rich*
PET *Positron emission tomography*
PFA *paraformaldehyde*
PHF *paired helical filament*
PP2A *Protein Phosphatase 2A*
PSD-95 *postsynaptic density protein 95*
*PSEN1 Presenilin-1*
*PSEN2 Presenilin-2*
PSP *Progressive supranuclear palsy*
PTM *post-translational modifications*
RA *retinoic acid*
ROI *Region of interest*
sAD *sporadic Alzheimer's Dementia*
SAP97 synapse-associated protein 97
SD *Standard deviation*
SHM-0 *SH-SY5Y cell medium without serum*
SHM-10 *SH-SY5Y cell medium with 10% fetal bovine serum*
shRNA *small hairpin RNA*
SNPs *single nucleotide polymorphisms*
TRIM46 *Tripartite Motif Containing 46*
TTL *tubulin tyrosine ligase*
VGLUT1 *vesicular glutamate transporter*

# 1. Zusammenfassung

Das Protein TAU ist ein neuronales Protein, das die Stabilität und Polymerisierung von Mikrotubuli (MT) reguliert. TAU ist normalerweise überwiegend im Axon lokalisiert, kann jedoch unter pathologischen Bedingungen in das somatodendritische Kompartiment fehlsortiert werden. Diese Fehlverlagerung stellt einen frühen Schritt in der pathophysiologischen Kaskade von Tauopathien dar, zu denen unter anderem die Alzheimer-Krankheit (AD) und die frontotemporale Demenz (FTD) zählen. Fehlverteiltes TAU führt im weiteren Verlauf zu einer Destabilisierung von Mikrotubuli, Störungen des axonalen Transports, synaptischer Toxizität und letztlich zu Neurodegeneration.

Um TAU-Fehlsortierung gezielt entgegenzuwirken, müssen die physiologischen Sortierungsmechanismen verstanden werden, die eine Anreicherung von TAU im Axon ermöglichen. Das Axon-Initialsegment (AIS) ist eine spezialisierte Struktureinheit im proximalen Axon, die eine Schlüsselrolle bei der Aufrechterhaltung der neuronalen Polarität – also der Trennung des axonalen und dendritischen Kompartiments – einnimmt. Daher wurde das AIS als möglicher Regulator der axonalen TAU-Sortierung vorgeschlagen. Darüber hinaus ist die Untersuchung des neuronalen MT-Netzwerks von zentraler Bedeutung, da es zum einen ebenfalls an verschiedenen Mechanismen der TAU-Sortierung beteiligt ist und zum anderen selbst direkt von TAU-Fehlsortierung betroffen ist.

Bislang wurden sowohl neuronale Polarisierung (inklusive AIS-Etablierung, MT-Struktur und TAU-Verteilung) als auch physiologische und pathologische TAU-Funktionen hauptsächlich in primären Nagetierneuronen und Tauopathie-Mausmodellen untersucht. Aufgrund verschiedener Einschränkungen dieser Modelle (insb. unterschiedliche TAU-Isoformen und Sequenzen, Überexpressionsartefakte, fehlende endogene Tau-Pathologie) lassen sich viele der beschriebenen Mechanismen jedoch nicht auf das menschliche zentrale Nervensystem (ZNS) übertragen, was sich auch in den bislang geringen therapeutischen Erfolgen im Bereich der Tauopathien widerspiegelt.

Das Ziel der vorliegenden Arbeit bestand daher in der Etablierung eines humanen Zellmodells, das eine zuverlässige Modellierung der TAU-Sortierung, AIS-Bildung und MT-Organisierung erlaubt und sich sowohl für die Untersuchung physiologischer als auch pathologischer TAU-Funktionen eignet. Zudem untersuchten wir den Beitrag des AIS zur axonalen TAU-Sortierung mit besonderem Fokus auf zwei zentralen AIS-Proteinen: (a) Ankyrin G (ANKG), dem Hauptorganisator des AIS, und (b) TRIM46, einem AIS-spezifischen Protein der Mikrotubuli-Organisation. Dazu setzten wir aus humanen induzierten pluripotenten Stammzellen (iPSC) abgeleitete Neuronen sowie neuronal differenzierte humane SH-SY5Y-Neuroblastomzellen

ein und verglichen sie mit primären Mausvorderhirnneuronen, die ein etabliertes Modell für neuronale Polarisierung und AIS-Studien darstellen.

Unsere Analysen mittels Immunfluoreszenz und qPCR zeigen, dass iPSC-abgeleitete Neuronen innerhalb der ersten ~40 µm des Axons ein typisches AIS ausbilden, gekennzeichnet durch die synchrone Akkumulation und Kolokalisation von ANKG und TRIM46. Die vollständige Integration dieser Proteine in das proximale Axon benötigte rund 1,5 Wochen und korrelierte mit der fortschreitenden Anreicherung axonalen TAUs sowie der strukturellen Polarisierung der iPSC-Neuronen. Die AIS-Struktur, neuronale Polarisierung und TAU-Sortierung waren mit denen primärer Mausneuronen vergleichbar.
Im Gegensatz dazu fehlte SH-SY5Y-Neuronen ANKG und damit ein klassisches AIS. Zwar exprimierten sie nach neuronaler Differenzierung TRIM46, jedoch in geringerem Maße als iPSC- und Mausneuronen. Dennoch erreichten auch AIS-defiziente SH-SY5Y-Neuronen zelluläre Polarität und eine axonale TAU-Verteilung, wenn auch mit reduzierter Effizienz.

Darüber hinaus etablierten wir ein Protokoll zur Visualisierung von Mikrotubuli-Polymerisierung in iPSC- und SH-SY5Y-Neuronen mittels EB3-Live-Cell-Imaging. Dadurch konnten wir das MT-Netzwerk von iPSC- und SH-SY5Y-Neuronen im proximalen und distalen Axon sowie in den Dendriten analysieren. Beide Zelltypen zeigten die für differenzierte Neuronen typische MT-Polarisierung: unidirektionale MTs im Axon (~95 % Plus-Ende der MTs nach außen) und gemischte Polarität in Dendriten (~75 % Plus-Ende der MTs nach außen). SH-SY5Y-Zellen wiesen dynamischere MTs auf, während die Polymerisationsgeschwindigkeit in beiden humanen Zelltypen ähnlich war und deutlich höher lag als in verschiedenen Tiermodellen aus früheren Studien.

Um die funktionelle Rolle von ANKG und TRIM46 weiter zu prüfen, wurden ergänzend shRNA-Knockdown-Experimente in iPSC-Neuronen mittels liposomaler Transfektion und lentiviraler Transduktion durchgeführt. Zwar ließ sich die lentivirale Transduktion insgesamt als effiziente Methode zur Expression von shRNA und Reportergenen in iPSC-Neuronen etablieren, ein spezifischer Knockdown der AIS-Proteine wurde jedoch nicht erreicht, was vermutlich auf methodische Limitationen im shRNA-Design, die Langlebigkeit der AIS-Proteine oder mögliche Off-Target-Effekte zurückzuführen ist.

Insgesamt deuten unsere Ergebnisse jedoch darauf hin, dass die MT-Polarisierung und die axonale TAU-Sortierung nicht primär von ANKG abhängen, da diese Prozesse regelhaft in SH-SY5Y-Neuronen stattfanden. Stattdessen scheint TRIM46, wie in vorherigen Studien gezeigt, die anterograde MT-Ausrichtung im Axon zu steuern und könnte damit die

Anreicherung von TAU durch aktiven Transport ermöglichen. ANKG hingegen trägt offenbar in reifen Neuronen eher zur Aufrechterhaltung der Polarität und neuronalen Erregbarkeit bei, ohne die axonale TAU-Anreicherung direkt zu beeinflussen.

Während SH-SY5Y-Zellen ein praktikables und leicht zu vermehrendes Modell für grundlegende Studien zu MT-Dynamik und TAU-Sortierung darstellen, bieten iPSC-abgeleitete Neuronen bessere Voraussetzungen für vertiefte TAU-Studien, die etwa das AIS, synaptische Interaktionen oder isoformspezifische TAU-Funktionen einbeziehen.

Zusammenfassend wurden in dieser Arbeit (a) quantitative Parameter zu AIS-Aufbau, MT-Dynamik und TAU-Sortierung in zwei humanen Zellmodellen etabliert, (b) ein Protokoll zur Visualisierung der Mikrotubuli-Polymerisierung in lebenden menschlichen Neuronen mittels EB3-Live-Cell-Imaging entwickelt, (c) gezeigt, dass MT-Polarisierung und basale axodendritische TAU-Polarität unabhängig von ANKG möglich sind, und (d) iPSC-Neuronen als geeignetes Modell für die Erforschung neuronaler Polarisierung und TAU-(Fehl)sortierung hervorgehoben, welches vielfältige Anwendungen in der Tauopathieforschung ermöglicht.

## 1.1. Abstract

The neuronal protein TAU regulates microtubule (MT) stability and polymerization. Under physiological conditions, TAU is predominantly localized to the axon, but under pathological circumstances it can mislocalize to the somatodendritic compartment. This mislocalization represents an early step within the pathophysiological cascade of tauopathies, including Alzheimer's disease (AD) and frontotemporal dementia (FTD). Mislocalized TAU leads to MT destabilization, impaired axonal transport, synaptic toxicity, and ultimately neurodegeneration. To counteract TAU missorting, it is essential to understand the physiological mechanisms that enable its enrichment in the axon. The axon initial segment (AIS) is a specialized structural domain in the proximal axon that plays a key role in maintaining neuronal polarity – that is, the structural and functional separation of the axonal and dendritic compartment. In addition, AIS alterations were observed in AD mouse models and human postmortem brain tissue from AD patients. The AIS has therefore been proposed as a potential regulator of axonal TAU sorting. In addition, the neuronal MT network is of central importance for TAU polarity, as it is also involved in several mechanisms of TAU sorting and is itself directly affected by TAU missorting. So far, neuronal polarization (including AIS formation, MT organization and TAU distribution) as well as physiological and pathological TAU functions have mainly been studied in primary rodent neurons and tauopathy mouse models. However, due to limitations of these models many of the described mechanisms cannot be transferred to the human central nervous system (CNS), contributing to the limited therapeutic progress in tauopathies.

The aim of this study was therefore to establish a human neuronal model that reliably recapitulates TAU sorting, AIS formation and MT organization, and to use this model to resolve the contribution of the AIS to axonal TAU sorting. Our experiments focused on two key AIS proteins: (a) Ankyrin G (ANKG), the master organizer of the AIS, and (b) TRIM46, an AIS-specific MT-organizing protein. For this, we used human induced pluripotent stem cell (iPSC)-derived neurons and neurons derived from the human SH-SY5Y neuroblastoma cell line in comparison to primary mouse forebrain neurons, a well-established AIS and TAU sorting model.

We discovered that iPSC-derived neurons develop a typical AIS within the first ~40 µm of the axon, marked by the synchronized accumulation and colocalization of TRIM46 and ANKG. The gradual integration of both proteins in the proximal axon required a considerable time of ~1.5 weeks and correlated with progressive axonal TAU enrichment and structural polarization. The AIS structure, cellular polarization and extent of TAU sorting in iPSC-derived neurons were comparable to those of primary mouse neurons. In contrast, we found that SH-SY5Y-derived neurons lacked ANKG and thereby a classical AIS, but expressed *TRIM46* upon neuronal differentiation. However, TRIM46 was less enriched at the proximal axon than in iPSC-derived

neurons and primary mouse neurons. Despite AIS-deficiency, SH-SY5Y-derived neurons attained axonal outgrowth and polarized TAU sorting, with a slightly lower efficiency than iPSC- and primary mouse neurons.

We analyzed MT organization of SH-SY5Y- and iPSC-derived neurons in the proximal axon, distal axon and dendrite using EB3 live-cell imaging. Both neuron types showed a polarized MT structure characteristic of differentiated neurons, with unidirectional (~95% plus-end out) MTs in axons and mixed MT polarity (~75% plus-end out) in dendrites. SH-SY5Y-derived neurons exhibited more dynamic MTs than iPSC-derived neurons, while MT polymerization speeds were similar in both human neuron types and exceeded reported velocities in rodent and non-mammalian neurons.

In conclusion, our findings indicate that MT polarization and axonal TAU sorting do not primarily depend on ANKG, as these processes were also observed in SH-SY5Y neurons. Instead, we propose that TRIM46 is responsible for anterograde MT orientation in axons, which may enable axonal TAU enrichment by means of active transport, while ANKG maintains neuronal polarity and excitability in mature neurons without directly influencing axosomatic TAU distribution.

While we found SH-SY5Y-derived neurons as a practical and proliferative model for the basic study of human MT dynamics and TAU sorting, iPSC-derived neurons represent a more mature model applicable for more profound TAU studies involving aspects such as the AIS, synapses and TAU-isoform-specific functions.

In summary, this study (a) established quantitative measures of AIS assembly, MT dynamics and TAU (mis)sorting in two human neuronal models, (b) developed a protocol for live-cell imaging of MT polymerization in human neurons, (c) showed that MT polarization and basal axodendritic TAU polarity can be established independently from ANKG, and (d) characterized iPSC-derived neurons as a well-suited model for the study of neuronal polarization and TAU (mis)sorting that offers many future applications in tauopathy research.

# 2. Introduction

## 2.1. The TAU protein

TAU is a key microtubule-associated protein (MAP) in the central nervous system (CNS), which controls MT stability and polymerization [1,2]. Under normal conditions, TAU is mainly found in axons. In disease states, however, it can detach from MTs, relocate to the somatodendritic region, and accumulate in insoluble deposits known as neurofibrillary tangles (NFTs) [1-3]. These tangles are a characteristic pathological feature of tauopathies, which include Alzheimer's Disease (AD), corticobasal degeneration (CBD), progressive supranuclear palsy (PSP), and other neurodegenerative diseases [2,3]. The mislocalization of TAU results in the disintegration of the MT system, impaired axonal transport, synaptic dysfunction and ultimately neurodegeneration [3,4]. Although the effects of TAU mislocalization have been widely studied, less is known about the triggers that drive TAU missorting, as well as the physiological mechanisms that ensure the axonal sorting of TAU under healthy conditions [3].

### 2.1.1. Physiology of TAU

TAU is encoded by the *MAPT* gene, which is located on chromosome 17 and comprises 16 different exons [1,2]. Structurally, TAU can be divided into four domains: The C-terminal domain, the "MT-binding region" (MTBR), a proline-rich domain in the middle, and the N-terminal "projection domain" (Fig. 2.1) [1,2]. The MTBR contains numerous tubulin binding sites and is thus – together with its adjacent domains – responsible for the MT assembly, whereas the N-terminal domain does not bind to MTs [1,2]. Six different TAU isoforms are found in the human CNS as a result of alternative splicing of *MAPT* exons 2, 3, and 10. They are distinguished by possessing either three or four tubulin-binding repeat domains (R) and by having one or two N-terminal inserts (N) (Fig. 2.1) [5].

The expression pattern of these six isoforms depends on the neurodevelopmental stage and the brain region [6,7]. The smallest TAU isoform 0N3R, "fetal TAU", is later replaced by the longer and more mature isoforms, with the 3R and 4R isoforms being present in a 1:1 ratio in most brain regions [6,7]. Moreover, only in adult primates, all TAU isoforms are found, whereas in other mammals, such as mice or rats, 3R isoforms are primarily abundant during development, with only 4R isoforms present in adulthood [2]. Importantly, the six TAU isoforms display distinct subcellular sorting patterns [8-11], have different interaction partners [12], vary in their phosphorylation sites and aggregation propensities [13-15] and are differentially involved in several tauopathies [2,9].

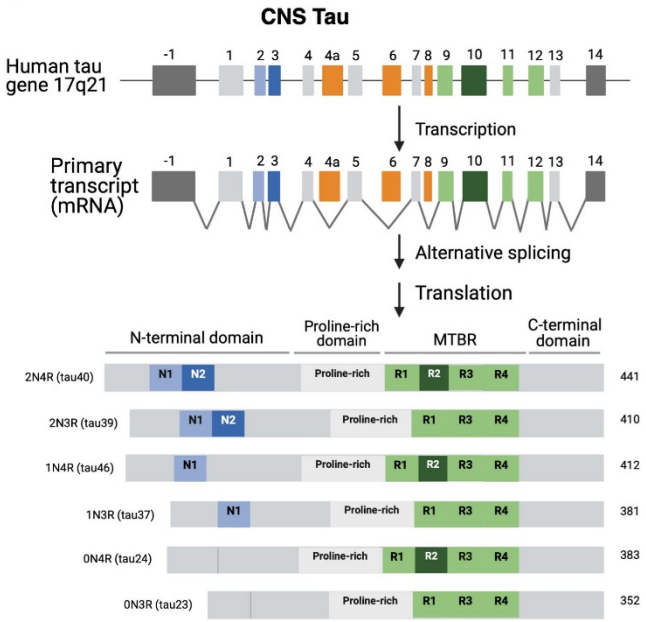


**Figure 2.1: Human *MAPT* gene and the six TAU isoforms generated by alternative mRNA splicing.**
The *MAPT* gene is located on chromosome 17q21. The mRNA transcript comprises 16 exons. The alternative splicing of exon 2, 3, 10 results in the generation of six different isoforms with a size of 441-352 amino acids, which are termed regarding the number of N-terminal inserts (N) and repeat domains (R): 0N3R, 0N4R, 1N3R, 2N3R, 2N4R. The repeat domains (R1-4) contain a highly repetitive amino acid sequence and are encoded by exon 9-12. The N-terminal inserts (N1, N2) result from translation of exon 2 and 3. Figure reproduced from [16].

TAU's binding to MTs requires not only the repeat domains (R1-R4), but also the sequences flanking these repeats and the neighboring proline-rich domain [2]. TAU stabilizes MTs by binding with its tubulin-binding sites to the β-tubulin at the inner surface of MTs, whereas the proline-rich domain lies on the outer MT surface and N-terminal projection domain points away from them [1,2]. The N-terminal domain regulates tubulin assembly indirectly via interaction with signaling and scaffolding proteins (e.g., Fyn kinase), as well as spacing between adjacent MTs and the plasma membrane [1,2]. Moreover, it has a regulatory function on axonal transport and the subcellular location of TAU within the neuron [1].

By regulating the MT network, TAU maintains fundamental cellular functions, e.g., morphogenesis and neurite outgrowth in the developing neuron as well as active transport of signaling proteins, organelles, or neurotrophic factors [4]. Moreover, TAU mediates variable functions beyond MT stabilization, termed "non-canonical functions", which involve a variety of different binding partners aside from MTs, e.g., membrane, motor, scaffolding and signaling proteins [2]. Of note, a smaller portion of TAU is also found in dendrites and the soma [17]. Dendritic TAU promotes maturation of dendrites and spines and is known to regulate synapse formation and activity [17]. In the nucleus, TAU protects DNA and RNA integrity [18,19]. It was also proposed that TAU influences subcellular signaling pathways by acting as a "sticky" binding platform for associated partners [2].

The primary function of TAU – stabilizing the axonal MTs – might indicate that the MAP is tightly and steadily bound to the MTs. Importantly, this is not the case: TAU stands in a constant equilibrium with dynamic binding/detachment to/from the MTs. The ability of TAU to bind to MTs is mainly determined by phosphorylation, which in turn is controlled by an interplay of phosphatases and kinases acting on TAU's phosphorylation sites. There are 85 reported phosphorylation sites in the 2N4R isoform, of which most are located in the neighboring regions of the tubulin-binding sites [2]. Additionally, other post-translational modifications (PTMs) are known to regulate TAUs MT affinity, among them acetylation, glycation, ubiquitylation and nitration [1].

Conclusively, TAU is the most prominent MAP in axons and exists in six isoforms generated by alternative splicing. While TAU's primary function is the stabilization of MTs and regulation of MT assembly, it has additional functions beyond the cytoskeleton, including cell signaling, synaptic regulation, and transcriptional regulation. TAU's binding to microtubules is highly dynamic and regulated by PTMs such as phosphorylation.

## 2.2. Microtubules

### 2.2.1. Microtubules: the basics

In eukaryotic cells, the cytoskeleton is built by three main components: actin filaments, intermediate filaments and microtubules, in order of ascending size [20].

The demands on the neuronal cytoskeleton are enormous, considering that neurons undergo drastic changes in their morphology, axons must grow out over distances in the millimeter to meter range, and neurons have to migrate over long distances to establish synaptic connections with their target cells.

Microtubules fulfill a range of functions. They are essential for the initial polarization of neurons, as they are required for outgrowth and branching of their neurites during neuronal development [21,22]. They form the "rail network" on which cellular cargo moves over long distances, e.g., targeting the pre- or postsynaptic membrane [23]. They are further involved in the regeneration of injured axons and neuronal migration within the CNS [24,25].

### 2.2.2. Structure and dynamics of microtubules

MTs are long tubes composed of heterodimers of α and β tubulin. α- and β-tubulin line up to form linear protofilaments, 13 of which assemble side-to-side to create the MT tube with a diameter of 20-30 nm [22]. They are in a constant state of alternating slow growth (polymerization) and rapid shrinkage (depolymerization) [26]. The growing end of the "MT tube" flanked by β-tubulin is termed "plus-end", the merely growing end flanked by α-tubulin is termed the "minus-end". The formation of the nascent MT from the minus end begins at the

microtubule organizing center (MTOC), which contains a γ-tubulin ring and can be represented by several structures depending on the cell type, often the centrosome in dividing cells [27]. The elongation of the MTs at the plus end is accomplished by adding GTP-bound heterodimers. The hydrolysis of GTP to GDP provides the energy needed to integrate the new tubulin into the growing structure. The constant addition of GTP-tubulin leads to an accumulation of GTP at the plus end, called "GTP-cap" that stabilizes the plus end. By this mechanism, the MTs can grow to a length of a few to hundreds of micrometers until they lack new heterodimers to add and all bound GTP at their tip has hydrolyzed. At this state the protofilaments splay apart – called "catastrophe" – which in turn provides new heterodimers for the repolymerization – called "rescue" – of the MTs. The constant shift between these two phases is called "dynamic instability" [21].

Microtubule-associated proteins (MAPs, see 2.2.4.) can influence the dynamic instability by enhancing or decreasing the stability of the plus end, thus reducing (e.g., TAU) or increasing (e.g., EB1) the catastrophe frequency, augmenting the growth speed (e.g., TAU) or boosting the repolymerization (e.g., TRIM46) [28].

### 2.2.3. **Microtubule organization in neurons**

Neuronal microtubules have distinct features compared to other somatic cell types to enable neuronal functions (e.g., long-distance transport, neuronal migration, neurite growth and regeneration) that are demanded by their extreme cell polarity and cell shape [21,22].

First, unlike spherical somatic cells, such as fibroblasts or unpolarized neural progenitors, whose MTs typically radiate outward from a central centrosome, post-mitotic neurons no longer maintain a central MTOC during differentiation [3,22]. Alternatively, neuronal MTs are nucleated throughout the whole neuron at non-centrosomal sites, such as Golgi outposts in dendrites, the MT-associated protein CAMSAP2 in the axon or preexisting MTs via the Augmin complex [3,29-34].

Another defining feature of neuronal MTs is their polarity [22]. In the axon, MTs show a uniform orientation with plus ends extending outward from the soma (~100%), whereas in dendrites, MTs have a mixed orientation [3,22]. The ratio of anterograde and retrograde MTs in dendrites varies across the neuronal type and species [3,35]. For example, anterograde MTs constitute approximately 6-12% in *Drosophila* [36], 55% in hippocampal rat neurons [31], 65% in mice *in vivo* [37] and 72-85% in humans [3,38]. The different polarity of MTs in dendrites and axons has functional implications: Firstly, the consistent plus-end-out arrangement in axons is essential axonal specification and outgrowth [39]. Secondly, microtubule polarity plays a key role in directing intracellular trafficking in neurons. Plus-end-directed kinesin motors mainly carry cargo into axons, while minus-end-directed dynein motors are predominantly responsible for transporting cargo along dendritic MTs. [3,22,40].

Neuronal MTs are also unusually stable compared to those in dividing cells, a property reinforced by MT-associated proteins such as TAU and MAP2 as well as PTMs. MT stability differs within the neuronal compartments: Stable MTs predominate in the axonal shaft, while dendrites contain more dynamic MTs throughout their arbor as well as the growth cone of the distal axon. This stability is reflected by fewer growth events in +TIP imaging experiments [38,41-43], resistance to MT depolymerization drugs [43,44], slower recovery after FRAP experiments [43] and the predominance of acetylated MTs (a marker of stability) over tyrosinated MTs [41,43,45]. Importantly, these differential PTMs on tubulin influence the affinity of MAPs [22] and axodendritic transport [45,46]. For example, axonal MTs are enriched in detyrosinated tubulin, which allows kinesin-1 to preferentially enter and move along axons [46].

Finally, specialized neuronal subcompartments harbor distinct MT features: In growth cones and dendritic spines, MTs are highly dynamic and only transiently invade actin-rich regions to support axonal guidance and synaptic plasticity. In the AIS, MTs are also more dynamic than in the axonal shaft [10,43]. Baas et al. reported that stable MTs are formed in the proximal axon, from where they could possibly be transported into the axonal shaft [47]. Electron microscopy shows that AIS MTs are tightly bundled and cross-linked, unlike in dendrites [48]. Both cross-linking and anterograde orientation in the proximal axon are mediated by TRIM46. Consequently, TRIM46 depletion leads to dendrite-like reorientation of MTs and a reduced fraction of bridged MTs [48,49].

In sum, neuronal MTs have unique characteristics, including non-centrosomal nucleation, MT polarity, differential stability and subcompartmental regulation, to sustain neuronal morphology and function. Differences in orientation, stability, and posttranslational modifications between axonal and dendritic MTs reflect the polarized organization of the microtubule network.

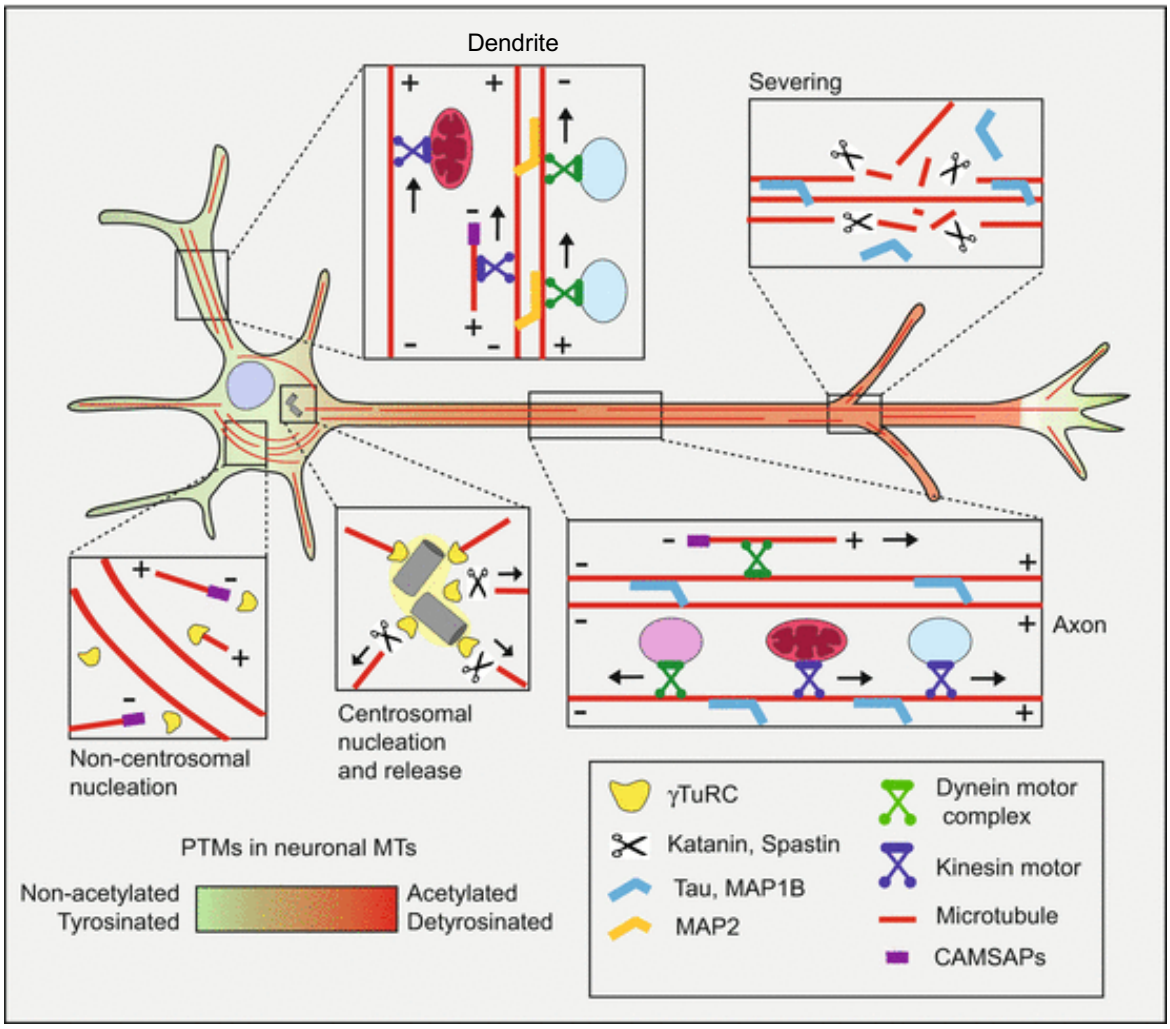


**Figure 2.2: Organization of the microtubule network in neurons.**
In axons, MTs have a consistent plus-end-out orientation and associate predominantly with TAU (see Axon). In contrast, dendritic microtubules exhibit mixed polarity and are associated mainly with MAP2 (see Dendrite).
MTs can originate from the centrosome or non-centrosomal nucleation sites such as Golgi outposts, CAMSAP2 or preexisting MTs. Intracellular cargo is transported by kinesin or dynein motors, which mediate retrograde and anterograde movement, respectively. MTs in the axon are more acetylated and less tyrosinated than dendritic MTs and thus more stable. Newly formed MTs are derived from the soma or from severing of preexisting MTs in the neurites and transported to their destination. Figure reproduced from [34,50].

### 2.2.4. **Microtubule-associated proteins (MAPs)**

Microtubule-associated proteins (MAPs) are proteins that interact with the microtubules and fulfill a variety of tasks mostly in terms of (re)organization of the MT network or active transport along the MT "railway". MAPs can be divided into six different groups based on their function [22]: (1) +TIP MAPs bind to the growing plus end which influences catastrophe, rescue frequency and MT growth rate. They are essential during neuronal development and communication with other cell structures, e.g., CLIP-170 with the plasma membrane. A key group of +TIPs is the end-binding (EB) protein family, which can autonomously associate with the plus end and facilitate the recruitment of other +TIPs, motors and binding partners. Furthermore, the proteins

EB1 and EB3 have gained a methodological importance in research, because the transfection of their fluorescently tagged versions allows to visualize the growing MT plus ends in live-cell imaging [42]. The counterpart is composed of -TIP (2) MAPs, which decorate the minus end and associate the MTs with their MTOC, thus being essential for cell shaping and mitosis, among many others. The -TIP protein CAMSAP2 stabilizes minus ends independently from MTOC or γ-tubulin in the proximal axon [32,51]. The third group of MAPs (3) binds along the MT lattice, like TAU, MAP1, MAP2 or MAP4. Structural MT-lattice MAPs mainly crosslink, bundle and stabilize MTs – TAU in the axon, MAP2 in the somatodendritic compartment. A fourth group (4) of MAPs is responsible for PTMs of tubulin subunits, such as the tyrosination by tubulin tyrosine ligase (TTL) which influences the stability of MTs and their interaction with other MAPs. The fifth MAP group (5) includes proteins that directly influence the integrity of MTs, e.g., the MT-severing enzymes spastin or katanin, which are essential for MT reorganization in axon outgrowth, dendrite branching or axonal regeneration after injury, but are also implied in MT degradation in tauopathy contexts [35]. Finally, the last MAP group (6) defines the MT motor proteins, including the kinesin and dynein family. Kinesins move in the direction of the plus end and have a preference for axonal MTs while dynein-carried cargo moves towards the minus end and preferentially along the dendrites.

### 2.2.5. **Microtubule dysfunction in disease**

Given the extensive roles of microtubules in maintaining neuronal structure, intracellular transport, and synaptic function, their dysregulation can have profound effects on neural function and development. Dysfunction of the neuronal MT system is associated with various neurodegenerative disorders, including AD [22,52,53]: In tauopathies such as AD and FTD, the loss of TAU's MT-stabilizing function contributes to axonal degeneration, synaptic dysfunction, and ultimately neurodegeneration [4]. In synucleinopathies like Parkinson's Disease or Multiple System Atrophy, intracellular protein aggregates interfere with transport along axonal MTs, whereas defects in motor proteins are found in intellectual disabilities, Charcot-Marie-Tooth Disease or Hereditary Spastic Paraplegia [52,54,55]. In ALS, mutations in tubulin genes cause protein aggregates which result in degeneration of MTs in motor neurons [56]. In addition, mutations in MT-associated genes can disrupt the cytoskeletal remodeling required for proper neuronal development, which has been implicated in autism spectrum disorders, or impair neuronal migration, as observed in lissencephaly [3,57]. Conclusively, the study of the neuronal MT system plays a pivotal role in research on neurodegenerative and neurodevelopmental disorders.

## 2.3. The axon initial segment (AIS)

The axon initial segment (AIS) is a unique structural region in neurons at the beginning of the axon. At the AIS, ion channels are densely clustered and here the action potential is formed before it propagates along the axonal membrane. Besides enabling neuronal excitability, the AIS also acts as a boundary between the axonal and the somatodendritic compartment, consisting of the cell body and the dendrites [58]. The morphological and functional segregation of these compartments is referred to as neuronal polarity [58]. Within this functional asymmetry of neurons, dendrites receive inputs and axons send synaptic release towards their target cells. The exclusive identity of the axon is maintained by the AIS, as demonstrated by knockdown experiments of *Ank3* and *Trim46*, which lead to the disruption of neuronal polarity [49,59,60].

### 2.3.1. Structure of the axon initial segment (AIS)

The AIS has a length of about 20 to 60 µm and is composed of a complex scaffold spanning from the dense MT bundles in the center to the plasma membrane, of which the protein Ankyrin G (ANKG), alternatively referred to as Ankyrin-3 (ANK3), is the master organizer [58,61,62]. The other main components of the AIS scaffold are the cytoskeletal proteins actin and spectrin, ion channels ($Na_v$, $K_v$), cell adhesion molecules (CAMs) such as NF-186 or NrCAM, and several connecting microtubule-associated proteins (MAPs) (see Fig. 2.3) [61].

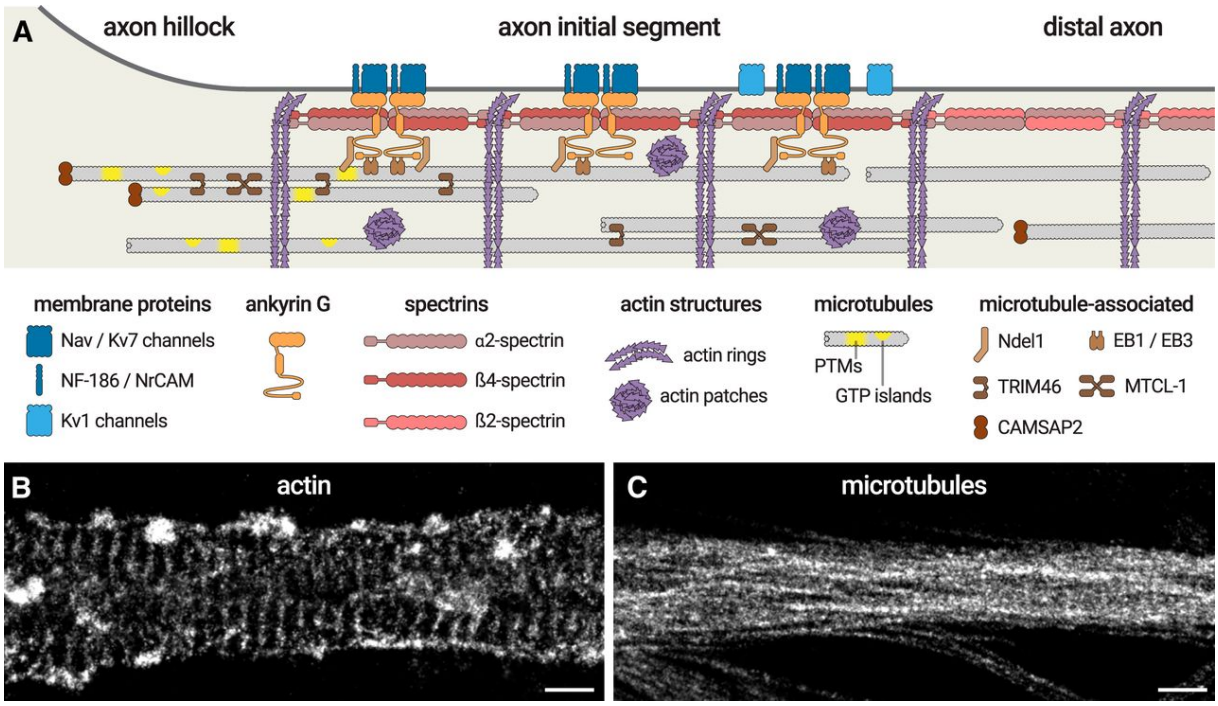


**Figure 2.3: Structure of the axon initial segment (AIS).**
**(A)** Schematic illustration of the AIS. ANKG (brown) anchors membrane proteins, including ion channels ($Na_v$ and $K_v7$) and cell adhesion molecules (NF-186 and NrCAM), at the plasma membrane. αII- and βIV-spectrins form tetramers which lie horizontally under the axolemma and attach to periodically spaced actin rings, resulting in a dense cytoskeletal submembrane complex. ANKG binds centrally to these αII/ßIV-tetramers. The tail domain of

ANKG binds to central MTs on behalf of the MAPs EB1, EB3 and Ndel1. TRIM46 connects adjacent MTs into bundles. MTs of the AIS are rich in PTMs and are oriented with their plus end towards the periphery, while the minus end is anchored by CAMSAP2. **(B)** STORM image of actin structures: Actin is found at the AIS in rings with a defined spacing of 190nm, as well as in scattered patches. **(C)** STORM image of MTs which are tightly bundled in the central AIS. Scale bar: 0.5 µm. Figure reproduced from [61].

ANKG is encoded by the *ANK3* gene, whose expression in neurons results in several ANKG isoforms (480kDa, 270kDa, 190kDa), of which the biggest isoform (480kDa) is responsible for the formation and maintenance of the AIS [63]. ANKGs N-terminal side is attached to the axolemma via interaction with the submembrane actin/spectrin complex and anchors the AIS membrane proteins, while the C-terminal domain binds to the MT bundles, which are located in the center of the axon, via several MAPs, such as end-binding protein 1 (EB1), end-binding protein 3 (EB3) and Ndel1 [63,64].

The cytoskeletal proteins actin and spectrin form a submembrane layer with a periodic pattern in the AIS, consisting of actin rings (Fig. 2.3.B) connected by tetramers of α2-/β4-spectrin [62]. ANKG is placed halfway between the actin rings, where it brings the ion channels and CAMs into position via interaction with its membrane-binding domain. $Na_v$ channels are concentrated approximately 30-fold higher in the AIS than in the somatic membrane, which enables the initiation of the action potential (AP). $K_v$ channel clustering in turn modulates intrinsic excitability and AP firing [58].

The CAMs located at the AIS, including NF-186 and NrCAM, recruit and interact with the axolemma surrounding extracellular matrix [65].

In myelinated axons, the majority of these AIS membrane proteins is also found at the Nodes of Ranvier, where they sustain the propagation of the AP along the axon.

On the cytosolic site, the carboxyterminal end of ANKG binds to central MT bundles. Specifically, ANKG's tail domain binds to the EB proteins EB1 and EB3 that in turn are attached to the axonal MTs. EBs normally act as +TIP proteins on growing MT ends but have an additional function in the AIS where they concentrate locally along the MT lattice [64]. The MTs in the AIS show some unique features (see 2.2.3): they are bundled into closely spaced fascicles, are rich in post-translational modifications and are oriented uniformly outwards from the soma [62].

ANKG clusters to the proximal part of young axons early during development, e.g., between embryonic day 18 and birth in rodents [66,67], or from DIV3 on in cultured rat hippocampal neurons [68], and subsequently recruits the other AIS components [59,66,69,70]. Knockdown of *Ank3* demonstrated the function of the AIS in maintaining neuronal polarity: *Ank3* shRNA treatment in polarized neurons leads to loss of most AIS proteins [59], axonal invasion of MAP2 and the appearance of dendritic spines in axons 1.5 weeks post-knockdown *in vitro* [59] and *vivo* [60].

The tripartite motif containing (TRIM) protein TRIM46 was recently identified as an AIS-specific protein, involved in the bundling and polarization of MTs in the proximal axon [49].

Generally, members of the TRIM protein family function within larger protein complexed that exhibit ubiquitin-protein ligase (E3) activity [71]. In contrast, neuronal TRIM46 acts as a crosslinker on axonal MT at the AIS and thereby builds parallel MT fascicles with uniform anterograde orientation in the axon. TRIM46 can be detected as early as DIV2-5 in cultured rat hippocampal neurons and is one of the earliest markers of axon specification [48,72]. As the neuron matures, TRIM46 accumulation is quickly followed by AIS assembly [49,73]. Several studies have highlighted the importance of TRIM46 in MT organization, axon formation and neuronal polarity [48,49,74-76]. Depletion of TRIM46 in primary rodent neurons led to a loss of polarized MT bundles in the AIS, impaired control of directional cargo transport and failure of axonal TAU sorting [48,49,74,75].

### 2.3.2. **Axon initial segment plasticity and disease**

Once anchored, the position of membrane proteins within the AIS remains overwhelmingly stable and their turnover is low [59,77,78]. Despite the outstanding stability of the AIS, this subunit maintains the ability to adapt to physiological and pathological changes. This plasticity includes, for example, changes in position during neuronal development [38], or in response to altered electrophysiological activity [79]. Also, the composition of ion channels can respond to changes in the excitation/inhibition balance, which adapts the neuron's excitability to its surrounding network [79].

Notably, AIS alterations were observed in disease contexts: In human post-mortem neocortex of AD patients, both TAU pathology and APP elevation correlated with changes in AIS structure on a cellular level [80,81]. Furthermore AD mouse models showed diminished ANKG abundance, disintegration of the AIS [82,83] and disruption of the AIS's barrier function in protein trafficking [82]. Re-expression of *Ank3* in the AD mouse model was able to restore its filter function and partly cognitive deficits [82]. One study reported that APP physically invades the AIS and associates with Ankyrin-G and βIV-spectrin in neurons of AD models [81]. ANKG-deficient mice showed deficits in memory and spatial learning as well as depressive and anxious behavior [83,84], all of which are typical features of AD. Similarly, RNAi knockdown of the *ANK3* homologue *Ank2* in *Drosophila* resulted in memory defects [85]. Furthermore single nucleotide polymorphisms (SNPs) in the *ANK3* gene were detected in genotyping studies of patients with late-onset AD [86].

Moreover, *ANK3* mutations are detectable in patients with intellectual disability [85] as well as bipolar disorder and schizophrenia [87]. Furthermore, the perturbation of several AIS proteins is detectable in epilepsy [88] and their gene loci are risk factors in a variety of other neurodevelopmental disorders [89]. Finally, neuronal injury – ischemic and mechanical – induced

AIS degradation [78], which could explain why cardiovascular risk factors or traumatic brain injury are associated with dementia.

On the other hand, TRIM46 abundance is diminished in brains of AD and Huntington's disease patients [90]. Moreover, in utero electroporation of *Trim46* shRNA, led to disturbed neural migration and axon formation in neonatal mice [49], implying a central role in early neurodevelopment. *Trim46* knockout rats showed smaller hippocampus sizes, altered neuronal architecture (fewer neurite arborization and dendritic spines, AIS shortening, downregulation of neurotransmitter receptors) and even hypoactive behaviors [90].

Altogether, these findings hint at a pathomechanistic role of the AIS in tauopathies and other neurodegenerative diseases.

## 2.4. Neuronal polarity

Cell polarity is the establishment of morphological and functional asymmetry between the compartments of a cell. No other cell in the human body undergoes such a strong polarization as neurons. They accomplish the drastic transformation from a spherical neural progenitor to an asymmetric neuron with multiple dendrites and an axon that can obtain a length in the millimeter- to meter-range. The structural discrepancies are accompanied by basic functional segregation, with dendrites receiving input and axons sending signals to target cells. Neuronal polarity includes the axodendritic segregation of membrane proteins, such as transmitter receptors, CAMs or ion channels. Moreover, it comprises the differential organization of MTs (unidirectional in axons vs. bidirectional in dendrites, see 2.2.3) and actin formations (actin rings and patches in the AIS vs. actin bulbs in dendritic spines). Finally, axodendritic separation of cytosolic proteins like MAPs (TAU in the axon vs. MAP2 in the dendrites) or signaling molecules is part of neuronal polarity. It is also reflected in the formation of compartment-specific subdomains, e.g., postsynaptic densities and spines in dendrites vs. presynaptic terminals, the AIS and nodes of Ranvier in axons [91].

Among the mechanisms enabling this drastic transformation are cytoskeletal rearrangements of the actin and microtubule network, directed transport, distinct overexpression of polarity factors and extracellular cues, which work in concert [91].

The AIS is considered as the main gatekeeper of this polarity. This was demonstrated in knockdown experiments of *Ank3* that resulted in the dismantling of the AIS, redistribution of MAP2 and TAU and the appearance of dendritic spines in axons 1.5 weeks post-knockdown *in vitro* [59] and *vivo* [60].

However, to what extent the AIS contributes to the establishment of neuronal polarity is under debate. The observation that SH-SY5Y-derived neurons form morphologically distinct axon and dendrites and enrich TAU in the axon without the presence of ANKG [92] and that polarized protein trafficking is maintained despite *Ank3 knock*down [63] motivated us to further investigate

the interplay between the AIS and neuronal polarity. Since *Trim46* was reported to be expressed in parallel with axogenesis [72] and to enable axon formation via MT rearrangements [49], we hypothesized that this protein was indeed essential for initial polarization. The comparison of a cell model with (iPSC-derived neurons) and a cell model without (SH-SY5Y-derived neurons) an ANKG-organized AIS, as well as selective knockdown of *ANK3* and *TRIM46* would help to understand if these AIS components are required for the establishment of neuronal polarity. As correct TAU sorting directly depends on AIS-mediated neuronal polarity [49], this would allow fundamental insights into molecular mechanisms of tauopathies.

So far, neuronal polarity was mainly studied in primary rodent neurons, either embryonic hippocampal rat neurons [93] or postnatal cerebellar granule neurons [94]. Rat hippocampal neurons are isolated from embryonic day 18 brains and undergo a well-defined course of 5 stages from spherical progenitors (stage 1) into polarized neurons with synapses (stage 5), initially defined by Banker and others [93]. Whether polarization mechanisms from these models overlap with polarization in human remains elusive, thus studies in human neuronal systems are necessary.

Finally, understanding neuronal polarity in human model systems is clinically relevant: Given the widespread importance of neuronal polarity in general cell function, it is not surprising that polarity defects can lead to various neurodegenerative (e.g., AD, FTD, ALS) and neurodevelopmental diseases (e.g., autism spectrum disorders, lissencephaly, schizophrenia). These defects lie in transcription factors (*TBR1* in ASD), polarity factors involved in neuronal migration and axon-dendrite differentiation (*LIS1* in lissencephaly, *PAR* proteins in neuropsychiatric disorders), MT-based transport proteins (*KIF5A* in ALS), other MAPs (*MAPT* in tauopathies) and scaffold proteins (*DISC1* in schizophrenia) [2,95-99].

## 2.5. TAU pathology

### 2.5.1. TAU missorting

When TAU detaches from the axonal MTs, it misfolds and aggregates in multiple steps, progressing from soluble “pretangles” over “paired helical filaments” (PHF) to “neurofibrillary tangles” (NFT). NFTs are hallmark lesions of tauopathies and are the basis of neuropathological disease staging in AD patients [100]. However, TAU-mediated neurodegeneration in tauopathies is not solely due to NFT accumulation but results from both (a) loss of TAU’s normal function and (b) the toxic gain-of-function effects of aberrant TAU and its aggregates [4].

**I. Consequences of TAU missorting**

**a. Loss of function:**

The lack of TAU in the axon leads to the breakdown of the MT network and subsequent disrupted axonal transport and synaptic dysfunction [4,55]. Neurons of AD patients show reduced MT density, length and stability [2].

The central role of MT disruption in the pathological cascade is underscored by studies demonstrating that treatment with MT-stabilizing drugs restores axonal transport and rescues the disease phenotype in tauopathy mouse models [2,101].

However, the fact that reduction of axonal MTs does not correlate with the number of PHF [4] and that *Mapt*-knockout mice only show few MT-related defects [102], strongly indicates that TAU detachment from MTs does not alone explain MT loss but that toxic gain-of-functions of missorted, hyperphosphorylated TAU play an important role in the pathological cascade.

**b. Toxic gain-of-function:**

Aberrant TAU exerts toxic effects in the form of NFT but also in its prefibrillar state. Earlier, it was thought that NFTs mediate toxicity by physically blocking cellular transport, sequestering normal TAU in a positive feedback mechanism [4] or by triggering neuroinflammation [103]. However, tauopathy mouse models showed synapse loss and microglial inflammation before the assembly of NFTs [104] and cleavage of transgenic TAU in these models improved memory function without influencing NFT levels [4,105]. These findings suggest that soluble, prefibrillar TAU – rather than TAU aggregates – is the primary driver of early neurotoxicity, whereas PHFs and NFTs represent late stage disease pathology. Prefibrillar TAU – primarily in the form of soluble oligomers, misfolded monomers and early aggregation intermediates – exerts neurotoxicity in various ways: It impairs axonal transport, induces synaptic and mitochondrial dysfunction, disrupts calcium homeostasis and leads to the interneuronal spread of TAU pathology [106].

However, several studies showed that an important mechanism of TAU toxicity, independent of aggregation, is the cellular missorting of TAU. When TAU accumulates in the somatodendritic compartment, it can directly interfere with synaptic function in dendritic spines [17,107]. In the presence of Aβ, dendritic TAU recruits the Fyn kinase to postsynaptic NMDA receptors, causing NMDA receptor phosphorylation and excitotoxicity [17]. Moreover, TAU mislocalization to dendritic spines was shown to impair synaptic targeting of AMPA and NMDA receptors [107]. Thus, postsynaptic TAU mediates synaptic dysfunction and excitotoxicity caused by amyloid beta in AD [17,108,109]. Moreover, missorted TAU induces MT degradation in dendrites, as it results in the relative overactivity of MT-severing enzymes katanin and spastin [110,111]. The dendritic localization of TAU might contribute to redistribution of its associated binding partners, e.g., Fyn, TTLL6, which then execute pathological functions in the “wrong” compartment [110]. Finally, missorted TAU impairs the ubiquitin-proteasome system at synapses [112] as well as translation by interacting with ribosomal proteins [113]. *MAPT* mutations associated

with missorting are also associated with chromosomal instability [114]. Strikingly, missorted TAU was also shown to spread trans-synaptically to neighboring neurons, which is believed to mediate disease progression [17].

Importantly, synaptic degradation correlates with the axodendritic redistribution of TAU and occurs before TAU aggregation, underlining that TAU missorting is an early mediator of neurotoxicity independently of TAU aggregation [115].

## II. Causes of TAU missorting

In order to prevent the described effects of abnormal TAU distribution, researchers have particular interest in the upstream events that cause TAU missorting. One is the aberrant hyperphosphorylation of TAU due to a disequilibrium of kinase and phosphatase activity [107,116]. Hyperphosphorylation reduces TAU's affinity for MT binding, causing it to detach and accumulate in the somatodendritic region. Moreover, exposure of Aβ leads to mislocalization of TAU and subsequent neuronal degradation *in vitro* and *in vivo* [117,118], possibly characterizing amyloid pathology as an upstream link to TAU pathology in AD. Among other direct causes are gene mutations in the *MAPT* gene [119] which result in TAU variants that are more prone to aggregation and somatodendritic accumulation. Over 60 of these *MAPT* mutations were identified in FTD patients [120]. Since *MAPT* mutations have a high potential to induce TAU missorting and aggregation, they are frequently used to model tauopathies in mouse models. Exonic TAU gene mutations such as P301L are aberrantly localized to dendrites [107], show reduced MT polymerization efficiency [121,122] and MT binding [123-125]. It was proposed that reduced MT binding impaired axonal retention. However, a recent study found that TAU lacking its MT-binding domain still localized correctly to the axon [126]. Instead, reduced MT polymerization and axonal transport deficits due to *MAPT* mutations [125,127,128] possibly disturb axonal TAU transport itself.

Several *MAPT* mutations (e.g., V337M, G272V and P301L) promote TAU aggregation, either by enhancing its intrinsic aggregation propensity [129] or by making TAU a more favorable target for phosphorylation by protein kinases, which subsequently decreases its MT affinity and facilitates its self-aggregation [130]. The mechanisms by which TAU aggregation itself results in somatodendritic TAU accumulation are not fully understood. In addition, the TAU mutant R406W showed impaired ability to bind to the plasma membrane which was linked to reduced trapping of TAU in axonal neurite tips [131]. Gauthier-Kemper et al. proposed that axonal targeting of TAU depends on its membrane binding via annexin A2 [131].

Besides this, there are rather indirect causes of TAU missorting that alter the TAU-MT interaction, among them other PTMs such as acetylation [132], $Ca^{2+}$- influx inducing stressors [118], oxidative stress [133] and inflammation [103]. Zhao et al. reported that TAU cleavage by caspase-2 led to mislocalization of TAU to dendritic spines [134]. Moreover, mechanical stress, as

causative in the tauopathy chronic traumatic encephalopathy (CTE), can induce TAU missorting [135].

Finally, it was shown that the disruption of the AIS can lead to TAU missorting. Knockdown of the AIS members *Ank3* and *Trim46* in cultured rat hippocampal neurons results in moderate redistribution of TAU and MAP2 to the opposite compartment [49]. Furthermore, Aβ exposure leads to disruption of the AIS and diminishes the polarized distribution of TAU [136,137]. Levels of ANKG were reduced in brains of AD patients [138] and mutations in *ANK3*, the gene encoding ANKG, lead to cognitive disorders and neuropsychiatric diseases [85]. Also, AIS disruption occurs in ischemic or mechanical brain injury which are known risk factors of dementia [78]. It was also reported that the knockdown of *Trim46* allowed retrograde diffusion of TAU [75] and altered directional cargo transport [49]. *Trim46* knockout in rodent models results in diminished hippocampus sizes and hypoactive behaviors [90]. Altogether, these findings make the AIS a possible candidate contributing to TAU missorting. However, *in vivo* studies demonstrating that AIS disruption alone leads to TAU missorting and subsequent biochemical, histopathological, and behavioral phenotype of tauopathies are still missing. Also, AIS-dependent TAU sorting was never studied in human neuronal models.

Taken together, TAU-mediated neurodegeneration comprises TAU missorting, hyperphosphorylation and aggregation. Somatodendritic missorting is an early mediator of neurotoxicity as it leads to the loss of its MT-stabilizing function in the axon and subsequent transport deficits, as well as toxic-gain of functions at the synapse and nucleus. In AD, dendritic TAU drives Aß-induced synaptic excitotoxicity, whereas Aß in turn promotes dendritic accumulation of TAU. TAU missorting is further caused by hyperphosphorylation, *MAPT* mutations and disruption of the AIS.

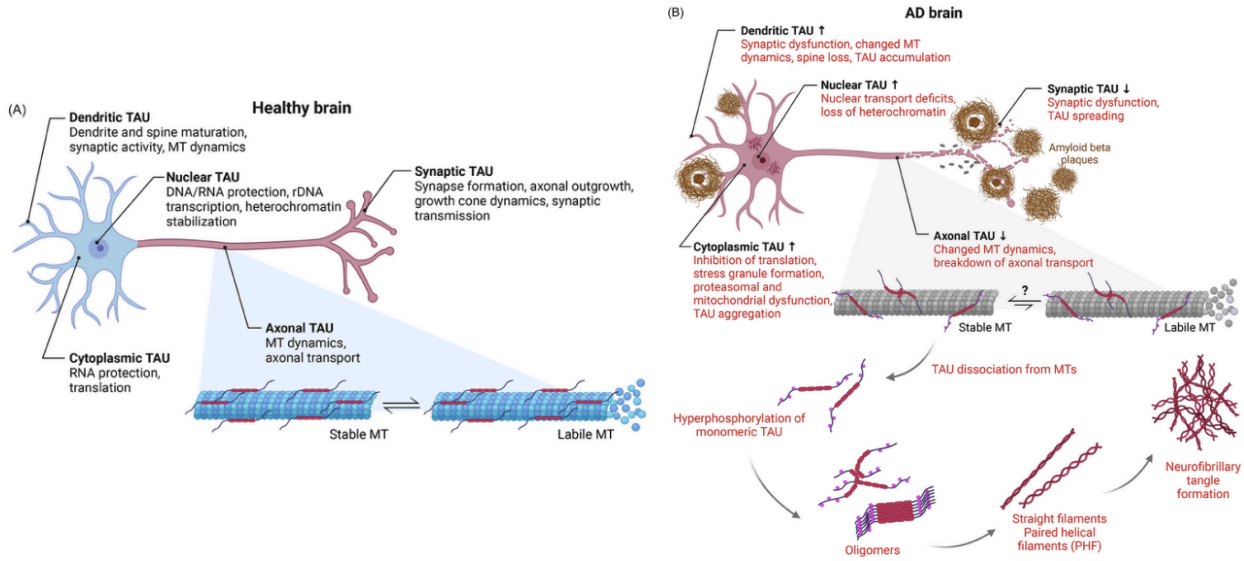


**Figure 2.4: Physiological and pathological functions of TAU.**

**(A)** In neurons under physiological conditions, TAU is predominantly concentrated in the axon, where it associates with MTs and regulates their dynamic instability. Moreover, axonal TAU regulates axonal transport and facilitates axonal outgrowth. Smaller amounts of TAU are found in the nucleus, dendrites and soma, where it fulfills additional functions. In dendrites, TAU promotes maturation of spines and synapse formation. Nuclear TAU influences transcription and translation as it helps to maintain DNA and RNA integrity. **(B)** Under pathological conditions (e.g., amyloid beta exposure, neuroinflammation, ischemic or mechanical injury, $Ca^{2+}$ influx), TAU detaches from axonal MTs and accumulates within the somatodendritic compartment. During this process, TAU becomes hyperphosphorylated, undergoes conformational changes and aggregates in a stepwise process to NFTs. When TAU can no longer properly regulate microtubule stability, axonal MTs become disorganized, disrupting intracellular transport which promotes synaptic deficits that eventually lead to neuronal loss. In addition, dendritic TAU causes MT degradation and dysregulation of NMDA receptors in dendritic spines. Missorted TAU can also interfere with protein degradation through the ubiquitin-proteasome system as well as translation at ribosomes. Notably, missorted TAU can propagate trans-synaptically to neighboring neurons, contributing to disease progression. Figure adapted from [9].

### 2.5.2. **TAU sorting**

TAU's selective accumulation in the axon is one of the earliest molecular events coinciding with the onset of neuronal polarity and loss of its polarized distribution leads to neurodegeneration in the context of tauopathies. The proper localization of TAU to the axon is essential for its function in MT stabilization, axonal trafficking and neuronal development. Several mechanisms have been proposed to explain TAU's axonal targeting, including:

1. **Axonal mRNA localization and local translation.**
2. **Differential retention of TAU in axons and dendrites** – due to distinct MT properties, post-translational modifications (PTMs), and local enzymatic activity.
3. **Predominant transit of TAU into the axon** – via diffusion or active transport along MTs.
4. **A selective barrier in the axon initial segment (AIS)** preventing the retrograde redistribution of TAU into the soma and dendrites.

Early studies identified axon targeting sequences in the 3'UTR region of *MAPT* mRNA suggesting axonal TAU sorting through local translation [139]. However, later findings contradicted this model: *MAPT* mRNA was also found in the somatodendritic compartment, and *MAPT* overexpression constructs lacking the 3' UTR still localized correctly to the axon [10]. Moreover, when TAU and MAP2 are microinjected into the soma, TAU rapidly diffuses into both axons and dendrites, but subsequently only persists in axons [140] and MAP2, vice versa, in the soma and dendrites. This suggested that a differential turnover and selective stabilization of the MAPs accounted for their compartmentalization.

The selective stabilization of TAU in the axon could depend on its interaction with the local MTs. Mutations in the MT-binding domain, such as P301L, reduce TAU's binding affinity to MTs, leading to its mislocalization. Similarly, the MT-destabilizing drug nocodazole leads to retrograde distribution of TAU, whereas MT-stabilization by taxol increases axonal TAU

enrichment [115]. The preferential stabilization of TAU in the axon might also be explained by the compartment-specific equilibrium of axonal phosphatases and kinases. Specifically, the overweight of kinases – e.g., Glycogen Synthase Kinase-3 (GSK-3), Cyclin-Dependent Kinase 5 (CDK5), Microtubule Affinity-Regulating Kinases (MARKs) – in the somatodendritic compartment reduces, whereas the predominance of phosphatases in the axonal compartment – like Protein Phosphatase 2A (PP2A) – increases the TAU-MT affinity. [141]

Moreover, TAU might have an exclusive affinity for axonal MTs due to the distinct MT properties in axons and dendrites, including PTMs, spacing or directionality. As an example, Boucher et al. demonstrated that TAU's MT affinity is regulated depending on the number of polyglutamylation modification of tubulin. [142].

Another possibility is that TAU preferentially transits into the axon rather than dendrites. TAU's mobility involves multiple mechanisms, including free diffusion in the cytosol, diffusion along the MT lattice and active transport [143]. The latter is substantially dependent on MT polarity. The structural difference of MTs in axons (uniformly oriented with plus-ends facing outwards) and dendrites (mixed orientation, ~50-70% plus-end out) may create a selective transport mechanism, where TAU preferentially associates with axonal MTs, while dendritic cargo is excluded [144].

Finally, there is evidence that the AIS plays a critical role in the polarized distribution of TAU: The knockdown of both *Ank3* and *Trim46* in cultured rodent neurons leads to moderate redistribution of TAU and MAP2 in the opposite compartment [49,59,60]. The role of the AIS in TAU sorting could be explained by several mechanisms: The AIS might control the above-mentioned properties of local MTs, e.g., PTMs, spacing, orientation. TRIM46 controls MT spacing as a cross-linker and ensures unidirectional alignment of MTs to the periphery (>95% plus end out) unlike in dendrites (no crosslinking, 50-70% plus-end out). Strikingly, knockdown of *Trim46* leads to bidirectionality of axonal MTs, partial inversion of cargo direction and augmentation of retrograde TAU diffusion into the soma [49,74,75].

Alternatively, the AIS could restrict the retrograde diffusion of TAU into the somatodendritic domain. Live-cell imaging of photoconvertible TAU showed that retrograde diffusion is specifically inhibited at the AIS and that this retrograde barrier was impaired by TAU phosphorylation and acetylation [115,138]. It is already known that the AIS restricts the axodendritic diffusion of membrane proteins [145] and lipids [146], but this is not applicable for TAU as a cytosolic protein. The AIS scaffold could act as physical filter restricting the free diffusion of TAU as it was described for other proteins of approximately the same size [145].

Importantly, the efficiency of TAU sorting is not uniform across all isoforms. While the 0N isoforms are enriched in the axon, the larger 1N and 2N isoforms are partly retained in soma and dendrites [10,147]. Thus, isoform-specific interaction partners, MT-binding affinity and PTMs could navigate TAU's subcellular localization [9].

In sum, cellular TAU polarity is likely controlled by multiple, potentially overlapping mechanisms. While early models emphasized local translation, a combination of protein-based sorting mechanisms seems more probable. Axonal retention of TAU could result from enhanced MT affinity, controlled by local enzymatic activity, or from interaction with local membrane-bound binding partners. Cumulating evidence hints at MT-dependent anterograde transport of TAU into the axon, either through diffusion along the MT lattice or motor-driven active transport. Additionally, the AIS could control axonal TAU sorting by maintaining overall cell polarity, by limiting retrograde diffusion, as well as by shaping the axonal MT architecture.

### 2.5.3. **Tauopathies**

Tauopathies are a heterogeneous group of different neurodegenerative diseases that share the aberrant deposition and aggregation of the TAU protein. This group of about twenty neurodegenerative diseases includes “primary” tauopathies, where TAU pathology is the main driver of disease, as well as “secondary” tauopathies, where TAU pathology is a pathomechanistic cofactor alongside a primary pathology [148].

The most common form of tauopathies and dementia, which accounts for 50-75% of all dementia cases is Alzheimer’s disease [149]. AD is classified as a secondary tauopathy, since the pathophysiology is determined not only by aberrant TAU tangles but also by aggregates of amyloid beta (Aβ) peptides. Currently about 57 million (constituted 2019) people of the world’s population aged over 60 years are affected with dementia and an increase of 166% to over 150 million people in 2050 is expected, mainly due to population ageing and population growth [150]. Furthermore, dementia is ranked among the top 10 of the most burdensome diseases worldwide and forecasted global costs are suspected to cross the threshold of 2 trillion US $ in 2030 (compare GDP of Germany in 2022: ~4 trillion US$), thus constituting an immense burden on the aging society [151].

Primary tauopathies include frontotemporal dementia (FTD), corticobasal degeneration (CBD) and progressive supranuclear palsy (PSP) and of which the latter two are categorized as atypical parkinsonian syndromes. Most tauopathies are of sporadic nature, only a small proportion shows genetic causes, for example *MAPT* mutations in familial cases of FTD [2].

Another example of secondary tauopathies, aside from AD, is chronic traumatic encephalopathy (CTE), in which TAU pathology results from repetitive head trauma, a dementia often found among boxers, American football or ice hockey players and hence referred to as "fistfighters dementia" [152].

These tauopathies can be classified regarding affected brain regions, neuronal subtypes, neuronal cell compartment and involved TAU isoforms in aggregation [148,153]. For example, in AD, TAU aggregates of both 3R and 4R isoforms in form of pretangles and NFTs are

predominant in neurons, while TAU aggregates in CBD consist of 4R isoforms, are less filamentous and present mainly in astrocytes.

### 2.5.4. **Alzheimer's disease: pathophysiology, clinics and treatments**

The majority of neurodegenerative diseases is defined by aggregates of proteinaceous fibrillary substances [4]. In AD, these comprise (a) intracellular NFTs, consisting of aberrant TAU and (b) so-called extracellular "senile plaques" (SP), made up from the β-amyloid peptide (Aβ). The Aβ peptide results from the proteolytic cleavage of its precursor protein APP [154].

The interplay of pathological APP/Aβ and TAU pathways is extensively studied: Although TAU mutations alone are capable of causing neurodegeneration, there is evidence that Aβ aggregation acts as an upstream trigger for TAU pathology [4]. However, the extent of TAU pathology has a stronger correlation with synapse loss and cognitive decline and [155]. Thus, TAU might be the substantial factor driving disease progression. In addition to promoting TAU hyperphosphorylation and mislocalization, Aβ oligomers mediate neurotoxicity by triggering oxidative stress and microglia- and astrocyte-mediated inflammation. Moreover, the amyloid pathway results in functional impairments of the endoplasmic reticulum, mitochondria and endosomes [156-159].

In AD, NFTs spread throughout the brain regions in a stereotypical hierarchy, which is described by the neuropathologic staging system of Braak [100]. Braak first described the entorhinal cortex as the initial detection site of NFTs, which subsequently progress to the hippocampus and the limbic system, and finally to primary sensory and motor areas of the neocortex. The six Braak stages correlate with the cognitive decline, with initial symptoms appearing typically at stage 3 to 4 [2]. Later it was found that subcortical nuclei, e.g., the locus coeruleus, are affected even earlier by TAU pathology, with tangles and pretangles already detectable in young individuals [2].

AD classically presents with cognitive impairment in short-term memory, but also speech, visuospatial processing and executive functions. Stereotypically these defects manifest progressively in patients >70 years, preceded by a preclinical period of mild cognitive impairment (MCI), where affected individuals still maintain the ability to perform the activities of daily living (ADL).

Most of AD cases (>95%) in patients >65 years (late-onset) are of sporadic nature, called sporadic AD (sAD). In less than 5% of AD cases, single genetic mutations can cause familial AD (fAD), which manifests already in younger patients (30-65 years, early-onset). The most common mutations causing fAD occur in the genes of *APP* or the APP-processing proteases *PSEN1 or PSEN2* and follow an autosomal dominant inheritance pattern. In contrast, the aetiology of fAD is multifactorial: Risk factors include age, the allele ε4 of apolipoprotein E

(*APOE*) gene, co-morbidities (hypertension, obesity, diabetes, viral infections, traumatic brain injury (TBI), depression) as well as lifestyle factors (smoking, physical inactivity) [154].

The diagnostic tools for AD comprise neuropsychological tests, but also analysis of TAU and Aβ levels in the cerebrospinal fluid (CSF) and PET imaging illustrating hypometabolism of affected brain regions [154].

So far, AD is mainly treated with symptomatic drugs, which comprise three cholinesterase inhibitors (donepezil, rivastigmine and galantamine) and the NMDA receptor antagonist memantine [154]. Their effect is limited to postponing symptom progression for approximately 6-12 months, whereas disease-modifying drugs target underlying pathologic processes of AD to slow down disease progression. Most disease-modifying AD drugs in the pipeline target the Aβ (15%) and TAU (11%) cascade or other disease mediators such as neuroinflammation or oxidative damage [160]. To date, three disease-modifying drugs have been approved in the U.S. – Aducanumab (2021) [161], Lecanemab (2023) [162], Donanemab (2024) [163] – which are monoclonal antibodies that target different species of Aβ aggregates.

These agents are highly effective in reducing Aβ plaque load (e.g., Lecanemab: 76% reduction of amyloid load in PET), but the preventive effect on cognitive decline is mild: In an 18-month trial, Lecanemab reduced the clinical AD rating score "CDR-SB" (scale range 0-18, with higher scores indicating greater impairment) progression only by 1.21 compared to 1.66 points with placebo, corresponding roughly to a 6-month delay in disease progression [162]. However, the effects seem to be higher if admitted over a prolonged timespan or if started earlier in less-severely affected subgroups (patients with low/medium TAU levels) [164,165]. The approval of these drugs in the European Union was first refused due to the European Medicines Agency (EMA) arguing that the observed effect on delaying cognitive decline did not outweigh the risk of serious adverse events, particularly amyloid-related imaging abnormalities (ARIA) which include cerebral edema and hemorrhage. However, in November 2024 the EMA re-examined its initial opinion and recommended a limited market authorization for a subpopulation of AD patients (non-homozygous *APOE4* genotype) [166].

Drugs in clinical trials targeting TAU comprise active vaccinations, monoclonal antibodies, small molecules reducing TAU phosphorylation, aggregation or TAU-mediated MT depolymerization as well as RNA-based therapies (antisense oligonucleotides and siRNAs) lowering *MAPT* expression [160].

Conclusively, against the background of growing AD prevalence, the holistic understanding of the Aβ and TAU cascade is imperative, whether to search for alternative therapeutic targets or to develop more precise biomarkers of disease progression and therapeutic outcome.

## 2.6. Experimental models in tauopathy research

### 2.6.1. Lack of reliable experimental models in AD and tauopathy research

The incidences of neurodegenerative CNS diseases are rising along with the aging of the worldwide population but the development of therapeutic drugs lags behind: therapeutics in the CNS field (a) take longer, (b) cost more, and (c) are less likely to be developed and approved compared to almost all other therapeutic areas[167,168]. This holds especially true for AD therapeutics, as there were no drug approvals for almost two decades (between memantine approval in 2003 and approval of the disease-modifying treatment aducanumab in 2021).

Among the reasons that have hindered successes in the field of AD drug development are the multifactorial nature of AD, the lengthy duration of clinical trials, the lack of clear biomarkers in earlier studies partly resulting in patient heterogeneity (before implementation of A/T/N biomarker system), and the lack of appropriate experimental models [169,170]. So far mainly human post-mortem brain tissue and rodent neurons have served as cell systems to unravel disease mechanisms and therapeutic targets. Post-mortem tissue does not allow inference of causalities and is inaccessible for experimental interventions.

Mice, on the other hand, are available for a variety of genetic manipulations [171] and suitable for various applications from basic research to drug interventions. Even though they have provided much mechanistic insight, they inherit multiple disadvantages.

Unlike humans, mice do not naturally develop age-related diseases such as Alzheimer's disease (AD). They do not spontaneously form amyloid plaques and TAU tangles [169]. To induce these features, researchers genetically modify mice to express mutant human genes under strong promoters, such as mutated amyloid precursor protein (*APP*) or presenilin gene (*PSEN1/PSEN2*) associated with fAD, as well as *MAPT* variants associated with FTD (e.g., *MAPT* with P301, P301S, V337, R406W mutations) [169,170,172,173]. Transgenic APP mice are able to recapitulate Aβ plaque formation. However, they do not exhibit TAU pathology or neuronal loss and cognitive decline correlates with Aβ load – unlike in humans [169,170,172]. To overcome this, newer mouse models overexpress mutant forms of *APP*, *PSEN*, and *MAPT* (triple transgenic) which show both tangle and plaque formation, age-dependent synaptic dysfunction and cognitive deficits [169,170,172]. Still, this overexpression leads to artificially high levels of TAU or Aβ and potentially introduces artificial toxicity not seen in human disease. Also, these mutations are associated with fAD and FTD, and do not reflect the heterogeneous etiology of most AD cases, which are sporadic (~95%) and result from a complex interplay of genetic, e.g., *APOE4*, *TREM2*, and *BIN1* mutations, and environmental risk factors including aging, diet, and vascular health [170].

Moreover, rodent proteins differ significantly from their human counterparts: many do not reach physiological abundance, are found in different cellular compartments, or show altered amino

acid sequences and isoforms [174,175]. The amino acid sequence of proteins encoded by several sporadic AD risk genes overlaps only to 50% in humans and mice [176]. Murine TAU shares only 89% sequence homology with human TAU, mainly due to the absence of a specific motif in the N-terminal domain in murine TAU [174,177]. A recent study also showed substantial differences in the interactome of human and murine TAU [178]. Moreover, rodents lack all 3R TAU isoforms, but the six different TAU isoforms have distinct roles in MT regulation [179,180], vary in their subcellular sorting [8-11] and have different interaction partners [12], phosphorylation sites and aggregation propensities [13-15]. The isoforms are implicated differentially in several tauopathies (e.g., 3R TAU in behavioral variant FTD vs. 4R TAU in PSP and CBD) or result in tauopathies when in imbalance (FTDP-17) [2,9,181]. To introduce human TAU isoforms in mice, humanized *MAPT*-knockin mouse models have been established (hTAU mice), but the 1:1 isoform ratio (3R/4R), as seen in humans, is not maintained [182].

Finally, while the broader symptomatology in AD mouse models can be correlated to the human condition and corresponding tests have been designed to do so (e.g., reference memory, working memory and executive function), some cognitive domains impaired in dementia patients are either less-studied (e.g., attention or episodic memory) or simply not assessable in mice (e.g., language, self-awareness) [183].

Ultimately, these limitations in rodent models are reflected in the poor translational success of AD drugs, which show successful results in animal models but fail in human clinical trials [169]. This suggests that current rodent models do not fully capture the complexity of human AD pathology. Given these limitations, there is an urgent need for human-relevant models to improve our understanding of AD and develop effective treatments.

### 2.6.2. **iPSC-derived neurons as a cell model for AD and tauopathy research**

A promising approach to a human neuronal cell system has emerged in 2007, which are induced pluripotent stem cells (iPSCs). In this approach, somatic cells, such as fibroblasts, are genetically reprogrammed into pluripotent stem cells, which can then be converted into various human cell types, including neurons and their subtypes [184,185]. For generation of neurons, iPSCs are mostly converted into neuronal precursor cells (NPC) and eventually into neurons by exposing them to external morphogens that guide them towards a neuronal fate, which is referred to as “directed differentiation”. An alternative method is “direct reprogramming” or “lineage conversion”, in which the donor cells – often fibroblasts – are converted directly into the cell lineage of desire by overexpressing certain transcription factors (e.g., *BRN2*, *ASCL1*, *MYTL1*, *NEUROD1* or *NGN2* for neuronal conversion), thereby bypassing the pluripotent precursor cell stages [184].

In the present dissertation, we used human WTC11 iPSCs that carry the doxycycline-inducible transgene *NGN2*, whose overexpression leads to differentiation into layer 2/3 glutamatergic

cortical neurons, bypassing the NPC state [3,186,187]. Additionally, cell culture media include pro-neuronal morphogens like N2, B27, BDNF.

These iPSC-derived neurons have several striking advantages: For the first time, patient-specific neurons can be generated that display the particular genetic profile of the donor's disease – sAD, fAD as well as other tauopathies – and be compared to iPSCs-derived neurons from healthy individuals – which might unravel altered pathways or neuronal subtypes affected [188]. One can differentiate iPSCs into various neuronal subtypes, allowing the study of AD or tauopathies in the subtype most associated with the disease, such as cortical neurons or basal forebrain cholinergic neurons in AD. Moreover, iPSC-based co-cultures of neurons with astrocytes and/or microglia enable the study of intercellular pathomechanisms relevant to AD, including neuroinflammation, Aβ processing, synaptic connectivity, cell-to-cell propagation of TAU pathology, and neurotransmitter homeostasis. [189-191]. IPSCs of a pool of heterogeneous individuals can be differentiated into genetic variable neurons to monitor, e.g., broad compatibility of a drug treatment [184]. In human iPSC-derived neurons, the full range of human TAU isoforms is detectable, however with a predominance of those associated with early neurodevelopment during the first weeks of differentiation [186,192].

In sum, iPSC-derived neurons could serve as an appropriate model to study human TAU (dys)functions relevant for tauopathies and other neurodegenerative diseases. The observation of neuronal differentiation in iPSCs could also demonstrate key aspects of human neurodevelopment *in vitro*, including the establishment of neuronal polarity, AIS formation, TAU sorting and MT dynamics, relevant to the pathogenesis of these conditions.

### 2.6.3. **SH-SY5Y-derived neurons as a human neuronal cell system**

An additional human neuronal model is provided by secondary neuronal cell lines originating from neural tumors, such as the human neuroblastoma line SH-SY5Y. When exposed to differentiation agents, such as nerve growth factor (NGF), brain-derived neurotrophic factor (BDNF) or retinoic acid (RA), these cells transform into excitatory neuronal cells [193,194]. In this study, we employed a RA/BDNF-based protocol to that drives SH-SY5Y cells toward a neuronal morphology and marker profile within two to three weeks [3,187,193].

Because SH-SY5Y cells are pre-mitotic, they can generate large numbers of neuronal cells suitable for experimental applications. Their differentiation procedures are generally quicker, more economical, and often yield more robust cultures compared to iPSC-derived neurons [3,193]. In their undifferentiated state, SH-SY5Y cells exhibit catecholaminergic traits but upon differentiation, they acquire dopaminergic, noradrenergic and cholinergic features [3,195]. However, the suitability of SH-SY5Y-derived neurons to study TAU (mis)sorting and AIS- or MT-related defects has not been addressed.

## 2.7. Aims of the study

The MT-associated protein TAU is highly enriched in axons of mature neurons, where it regulates MT stability and axonal integrity. In AD and related tauopathies, TAU undergoes pathological modifications, most notably somatodendritic mislocalization, hyperphosphorylation and aggregation. Somatodendritic missorting of TAU constitutes an early and critical event in disease pathogenesis, leading to disruption in axonal transport, postsynaptic toxicity and ultimately neuronal degeneration.

Given this pathological cascade, strategies that prevent TAU missorting could have significant therapeutic potential. However, the mechanisms that govern the efficient axonal sorting of TAU under healthy conditions remain incompletely understood. Both AIS- and MT-based mechanisms were proposed to control axonal TAU sorting. The AIS is a specialized domain in the proximal axon and controls neuronal polarity, which includes axodendritic differences in neurite architecture, MT organization and MAP sorting (MAP2/TAU). Whereas the role of ANKG in maintenance of overall cell polarity and TRIM46's role in organizing axonal MTs was investigated in animal models [49,59,60], their distinct involvement in TAU (mis)sorting in human neurons has not directly been addressed. Moreover, the functional interplay of both AIS proteins remains uncertain.

It was furthermore proposed that axonal TAU enrichment depends on properties of MTs in the axon [196-200]. Neuronal MT polarity could drive TAU sorting via preferential transport in axons and dendrites. However, MT polarity was barely studied in human neuronal models.

Finally, this study investigates AIS structure, MT organization and TAU sorting in human *in vitro* models. In doing so, we aim to overcome limitations of rodent models currently used in TAU research, including (a) different TAU isoform composition [9], (b) different TAU interaction partners [178], (c) impaired TAU sorting behavior following *MAPT* overexpression in rodent models [126], (d) incomplete recapitulation of AD phenotype in transgenic mouse models [169,170,172], and (e) limited translatability of findings from animal models to humans [169].

Therefore, in this study, we aimed to:

- **AIM 1)** investigate neuronal polarization and AIS development in human neuronal models
- **AIM 2)** explore the role of the AIS proteins ANKG and TRIM46 in MT organization, TAU sorting and neuronal polarization
- **AIM 3)** characterize the compartmental MT organization in human neuronal models
- **AIM 4)** discuss the suitability of iPSC- and SH-SY5Y-derived neurons for AD and tauopathy research.

By addressing these questions, we aim to understand mechanisms of physiological TAU sorting in human neuronal models. By investigating AIS development, MT polarization and neuronal polarization in human neurons, we aim to provide a basic characterization of two human neuronal models potentially suitable for extended research of tauopathies and neurodegenerative diseases.

# 3. Materials and methods

## 3.1. Materials

### 3.1.1. Cell culture

#### 3.1.1.1 Cell lines

For most experiments the *NGN2*-WTC11 hiPSCs were used as generated by Wang et al. [186], as well as the human neuroblastoma cell line SH-SY5Y. SH-SY5Y cells were kindly provided by the group of Dr. Rudolf Wiesner (Veg. Physiology II, University Hospital Cologne). Mouse primary forebrain neurons were extracted from embryonic FVB/N wildtype mice brain at embryonic day 13.5 (E13.5), kindly provided by the group of Dr. Min Kye (Institute for Human Genetics, University Hospital Cologne). Furthermore, human embryonic kidney (HEK) 293T cells (ATCC, CRL-3216) were used.

#### 3.1.1.2 Media and reagents

**Table 1: List of solutions for cell culture**

| Solution | Company, Product ID | Comments |
|---|---|---|
| Geltrex LDEV-Free, hESC-Qualified, Reduced Growth Factor Basement Membrane Matrix | TFS, A1413302 | Thawed overnight at 4 °C, handling on ice, mixed 1:1 with KO-DMEM, 300 µl aliquots, stored at -20 °C. |
| 10 mM Thiazovivin | Axon Med Chem, 1535 | 5mg dissolved in 1605 µl, DMSO, stored at -20 °C in 50 µl aliquots |
| Dulbecco's Phosphate Buffered Saline (DPBS) | Merck, D8537 | |
| Versene | TFS, 15040066 | |
| KnockOut DMEM | TFS, 10829018 | |
| KnockOut Serum Replacement (KSR) | TFS, 10828028 | |
| Antibiotic-Antimycotic Solution 100x | Merck, A5955 | |
| Accutase | Merck, A6964 | |
| StemMACS iPS-Brew XF 50x | Miltenyi Biotec, 130-104-368 | 10 ml were added to 500 ml iPSC maintenance medium before usage |

| | | |
|---|---|---|
| KO DMEM/F-12 | TFS, 12660012 | |
| DMEM | TFS, 31966047 | |
| DMEM/F-12 | TFS, 11320033 | |
| DMEM/F-12 + GlutaMAX™ | TFS, 10565018 | |
| Neurobasal Medium | TFS, 21103-049 | |
| GlutaMAX™ Supplement 100x | TFS, 35050061 | |
| B27 Supplement, 50x, serum-free | TFS, 17504044 | Stored at -20 °C |
| Neuropan 2 Supplement, 100x | Pan-Biotech, P07-11010 | Stored at -20 °C |
| 10 µg/ml Recombinant Human BDNF | Peprotech, 450-02 | 10 µg dissolved in 1 ml DPBS+0.1% BSA, aliquoted and stored at -20 °C. |
| 10 µg/ml Recombinant Human NT-3 | Peprotech, 450-03 | 10 µg dissolved in 1 ml DPBS+0.1% BSA, aliquoted and stored at -20 °C. |
| 6 mg/ml Cultrex 3D Culture Matrix Laminin I | Biotechne, 3446-005-01 | Aliquoted and stored at -20 °C. |
| Laminin from Engelbreth-Holm-Swarm murine sarcoma basement membrane | Sigma, L2020 | Laminin concentration is batch-dependent. Stored at -20 °C. |
| Non-essential amino acids (NEAA) | TFS, 11140035 | |
| 1 mg/ml Doxycycline hyclate | Merck, D9891 | 10 mg dissolved in 10 ml dd$H_2O$, aliquoted and stored at -20 °C. |
| Trypan Blue | Bio-Rad, 1450021 | |
| 1 mg/ml Poly-D-Lysine | Merck, P7886 | 10 mg dissolved in 10 ml DPBS. Stored 1 ml aliquots at -20 °C. |
| Trypsin 0.5%/EDTA 0.2% in PBS, w/o: Ca and Mg, 10x | Pan-Biotech, P10-024100 | |
| Fetal Bovine Serum (FBS) | Biochrom AG, S 0615 | Stored at -20 °C |

| | | |
|---|---|---|
| Antibiotic-Antimycotic Solution 100x | Merck, A5955 | |
| Retinoic acid (RA) | Sigma-Aldrich | Stored at -20 °C |
| Lipofectamine™ 2000 transfection reagent | TFS | |
| PolyJet™ in vitro DNA Transfection Reagent | SignaGen® Laboratories, #SL100688 | |
| Polyethylenimine (PEI) transfection reagent | Polysciences, 23966 | |

### 3.1.1.3 **Medium recipes**

**Table 2: List of media**

| **Medium** | **Ingredients** |
|---|---|
| cBrew | • StemMACSTM iPS-Brew XF with supplement<br>• 1x Antibiotic-Antimycotic solution |
| Pre-differentiation medium | • 1x Antibiotic-Antimycotic solution<br>• 1x Neuropan-2 Supplement<br>• 1x non-essential amino acids<br>• 10 ng/ml BDNF<br>• 10 ng/ml NT-3<br>• 1.5 µg/ml Laminin<br>• 2 µg/ml Doxycycline<br>• KO DMEM/F-12 |
| Neuronal maturation medium | • 0.5x B27 Supplement<br>• 0.5x Neuropan-2 supplement<br>• 1x Antibiotic-Antimycotic solution<br>• 1x non-essential amino acids<br>• 1.5 µg/ml Laminin<br>• 10 ng/ml BDNF<br>• 10 ng/ml NT-3<br>• 2 µg/ml Doxycycline<br>• 50% DMEM/F-12<br>• 50% Neurobasal Medium |
| iPSC-freezing medium | • 9 ml KSR<br>• 3 ml Brew<br>• 3 ml DMSO |
| HEK-293T maintenance medium | • DMEM, high glucose, GlutaMAX Supplement, pyruvate (TFS, 31966047)<br>• 10% FBS<br>• 1x Antibiotic-Antimycotic solution |

| | |
|---|---|
| SH-SY5Y cell culture medium with 10% serum (SHM-10) | • 500 ml DMEM/F-12 + GlutaMAX 1 (1X)<br>• 5 ml Antibiotic-Antimycotic solution (100X)<br>• 50 ml FBS |
| SH-SY5Y cell culture medium without serum (SHM-0) | • 500 ml DMEM/F-12 + GlutaMAX 1 (1X)<br>• 5 ml Antibiotic-Antimycotic solution (100X) |
| SH-SY5Y cell freezing medium | • 90% FBS<br>• 10% DMSO |

### 3.1.2. **Molecular biology**

#### 3.1.2.1 **Kits**

**Table 3: List of commercial kits for molecular biology**

| **Name** | **Company** | **Purpose** |
|---|---|---|
| PureYield™ Plasmid Miniprep System | Promega, A1223 | Plasmid isolation from bacteria cultures |
| PureYield™ Plasmid Midiprep System | Promega, A2492 | Plasmid isolation from bacteria cultures |
| PureYield™ Plasmid Maxiprep System | Promega, A2392 | Plasmid isolation from bacteria cultures |
| NucleoSpin™ Gel & PCR Clean up Kit | Macherey Nagel, 740609.50 | PCR clean up and gel extraction |
| PureLink RNA mini kit (TFS) | TFS, 12183018A | RNA isolation |
| ProtoScript II First Strand cDNA Synthesis kit (NEB) | NEB, E6560 | cDNA synthesis via reverse transcription |

#### 3.1.2.2 **Reagents**

**Table 4: List of reagents for molecular biology**

| **Reagent** | **Company** |
|---|---|
| Agarose | Sigma Life Sciences |
| TBE Buffer (10x) | AppliChem |
| Gel Loading Dye Purple (6x) | NEB |
| GelRed® Nucleic Acid Gel Stain (10.000X) | Biotium |
| Quick-Load® 1 kb Plus DNA Ladder | NEB |
| Restriction Enzymes<br>• BamHI: #R0136<br>• HindIII: #R0104 | NEB |

| | |
|---|---|
| • EcoRI: #R0101<br>• PacI: #R0547 | |
| T4 DNA Ligase (M0202L) | NEB |
| *Taq* DNA polymerase with Standard *Taq* buffer (M0495) | NEB |
| SYBR Green Master Mix (A46012) | TFS |

### 3.1.2.3 Solutions

**Table 5: List of solutions for molecular biology**

| Solution | Ingredients |
|---|---|
| Bacterial culture medium (LB medium) | 10g NaCl, 10g tryptone, 5g yeast extract, filled up to 1 liter with H2O |
| Blocking and Permeabilization solution (B+P solution) | 1% (w/v) BSA, 0.5% (v/v) Triton X-100 in PBS |
| Fixation solution | 7.4% (v/v) Formaldehyde in PBS |
| Storage solution | 55% (v/v) Glycerol in PBS |
| Ampicillin | - |
| Kanamycin | - |

### 3.1.2.4 Oligonucleotides for transfection and transduction

**Oligomer sequence for shRNAs in pRNAT**:

Forward oligomer: 5'-GATCCCC – target sequence – TTCAAGAGA – target sequence antisense – TTTTTG-3'

Reverse oligomer: 5'- AGCTCAAAAA – target sequence – TCTCTTGAA – target sequence antisense – cagttccttctccatgttcGGG-3'

**Oligomer sequence for shRNAs in pLKO.3G**

Forward oligomer: 5'-AATT— target sequence —CTCGAG— target sequence antisense— TTTTTTTAT-3'.

Reverse oligomer: 5'-AAAAAAA— target sequence —CTCGAG— target sequence antisense-3'

**Table 6: List of shRNAs**

| shRNA | Target Sequence |
|---|---|
| *TRIM46* shRNA 1 | GAACATGGAGAAGGAACTG |
| *TRIM46* shRNA 2 | GCTGACAGAGCTTAACTTA |

| | |
|---|---|
| *TRIM46* shRNA 3 | GAACATGGAGAAGGAACTGTT |
| *TRIM46* shRNA 4 | GCTGACAGAGCTTAACTTATT |
| *ANK3* shRNA 1 | GTTGTCTACACCATCTTCT |
| *ANK3 shRNA* 2 | GCATTTAAGTCAATTATTA |
| *ANK3 shRNA* 3 | GACATTATGAGTAATATAA |
| *ANK3 shRNA* 4 | GTGATTATGGAAATATTTA |
| *ANK3 shRNA* 5 | GCATTTAAGTCAATTATTATT |
| *ANK3 shRNA* 6 | GACATTATGAGTAATATAATT |
| Scrambled shRNA | TAATGGTGCGAATAGTACA |

### 3.1.2.5 **Primer**

**Table 7: List of primers**

| **Primer name** | **Sequence (5' → 3')** |
|---|---|
| *TRIM46* Primer 1 | GCAGCTGCACAACAGGATTG |
| *TRIM46* Primer 2 | ATCATAGGCAAAGGTGCGCT |
| *ANK3* Primer 1 | GTCTGAGCAAAAGCAGGGAGA |
| *ANK3* Primer 2 | ACCGTTCGCTGTTACGAGTG |
| *HPRT* Primer 1 | GCTATTGTAATGACCAGTCAACAGGGGAC |
| *HPRT* Primer 2 | CCTTGACCATCTTTGGATTATACTGCC |

### 3.1.2.6 **Plasmids**

**Table 8: List of plasmids**

| **Plasmid name** | **Backbone** | **Promoter** | **Reporter** | **Resistance** | **Insert** | **Reference** |
|---|---|---|---|---|---|---|
| ***pUltra*** | pUltra | UbC | eGFP | Ampicillin | None | Addgene #24129 |

| | | | | | | |
|---|---|---|---|---|---|---|
| ***pLKO3.G.*** | pLKO3.G. | U6 | eGFP | Ampicillin | None | Addgene plasmid #14748 |
| ***pRNAT*** | pRNAT-H1.1/Hygro | H1 | GFP | Hygromycin | None | Gene Script #SD1214 |
| ***pRNAT-TRIM46 KD1*** | pRNAT-H1.1/Hygro | H1 | GFP | Hygromycin | *TRIM46* shRNA 1 | This study |
| ***pRNAT-TRIM46 KD2*** | pRNAT-H1.1/Hygro | H1 | GFP | Hygromycin | *TRIM46* shRNA 2 | This study |
| ***pRNAT-ANK3 KD1*** | pRNAT-H1.1/Hygro | H1 | GFP | Hygromycin | *ANK3 shRNA* 2 | This study |
| ***pRNAT-ANK3 KD2*** | pRNAT-H1.1/Hygro | H1 | GFP | Hygromycin | *ANK3 shRNA* 3 | This study |
| ***pLKO-Shscramble*** | pLKO.3G | U6 | eGFP | Ampicillin | Scrambled shRNA | This study |
| ***pLKO-TRIM46 KD1*** | pLKO.3G | U6 | eGFP | Ampicillin | *TRIM46* shRNA 3 | This study |
| ***pLKO-TRIM46 KD2*** | pLKO.3G | U6 | eGFP | Ampicillin | *TRIM46* shRNA 4 | This study |
| ***pLKO-ANK3 KD1*** | pLKO.3G | U6 | eGFP | Ampicillin | *ANK3 shRNA* 5 | This study |
| ***pLKO-ANK3 KD2*** | pLKO.3G | U6 | eGFP | Ampicillin | *ANK3 shRNA* 6 | This study |
| ***p_tdTomato*** | pCMV | CMV | tdTomato | Ampicillin | None | Zempel et al. (2017) |
| ***p_tdTomato-EB3*** | tdTomato-N1 | CMV | tdTomato | Kanamycin | *MAPRE3* (EB3) | Addgene #50708 |
| ***pMD2.G*** | pMD2.G (envelope) | CMV | - | Ampicillin | *VSV-G* envelope | Addgene #12259 |

| | | | | | | |
|---|---|---|---|---|---|---|
| ***psPAX2*** | psPAX2 (packaging) | CMV | - | Ampicillin | None | Addgene #12260 |

### 3.1.2.7 Bacterial strains

**Table 9: List of bacterial strains**

| Name | Company |
|---|---|
| *E. coli* TOP10 | Invitrogen, C404006 |
| *E. coli* Stbl3 | Invitrogen, C737303 |

## 3.1.3. Microscopy

### 3.1.3.1 Antibodies

**Table 10: List of antibodies**

| Name | Origin | Dilution | Company |
|---|---|---|---|
| **Primary antibodies** | | | |
| Anti-TRIM46, polyclonal | rabbit | 1:1000 | Synaptic Systems, 377003 |
| Anti-AnkyrinG, monoclonal | mouse | 1:500 | Neuromab (Biozol), 75-146 |
| Anti-MAP2, polyclonal | chicken | 1:2000 | Abcam, ab5392 |
| Anti-TAU, polyclonal | rabbit | 1:1000 | Dako, A0024 |
| Anti-TAU, monoclonal | mouse | 1:1000 | SantaCruz, sc-390476 |
| **Secondary antibodies** | | | |
| Anti-rabbit IgG-Alexa Fluor 488 | donkey | 1:1000 | TFS, A21206 |
| Anti-rabbit IgG-Alexa Fluor 568 | goat | 1:1000 | TFS, A11011 |
| Anti-rabbit IgG-Alexa Fluor 647 | donkey | 1:1000 | TFS, A3157 |
| Anti-chicken IgG-Alexa Fluor 488 | goat | 1:1000 | TFS, A11039 |
| Anti-chicken IgG-Alexa Fluor 568 | donkey | 1:1000 | TFS, A78950 |

| | | | |
|---|---|---|---|
| Anti-chicken IgG-Alexa Fluor 647 | goat | 1:1000 | TFS, A21449 |
| Anti-mouse IgG-Alexa Fluor 488 | donkey | 1:1000 | TFS, A21202 |
| Anti-mouse IgG-Alexa Fluor 568 | goat | 1:1000 | TFS, A11004 |
| Anti-mouse IgG-Alexa Fluor 647 | goat | 1:1000 | TFS, A32728 |

#### 3.1.3.2 Solutions

**Table 11: List of solutions for microscopy experiments**

| Solution | Company / Ingredients |
|---|---|
| Fixation solution | 7.4% (v/v) Formaldehyde in PBS |
| Storage solution | 55% (v/v) Glycerol in PBS |
| Blocking and Permeabilization solution (B+P solution) | 1% (w/v) BSA, 0.5% (v/v) Triton X-100 in PBS |
| PolyMount™ | Polysciences |
| Hoechst 33342 (NucBlue™) | TFS |

#### 3.1.3.3 Software

**Table 12: List of used software**

| Software | Purpose | Company |
|---|---|---|
| ZenBlue Pro imaging software (V2.6) | Image acquisition | Zeiss |
| LasX Life Sciences | Live Image acquisition | Leica Microsystems |
| Fiji/ImageJ | Image analysis | OpenSource |
| GraphPad Prism 8.2.0. | Statistical analysis | GraphPad Software Inc. |
| StepOne™ Software | qPCR | TFS |
| Microsoft Office 2016 | Data analysis, writing, thesis layout | Microsoft |
| Mendeley Reference Manager 2.84.0 | Citation | Mendeley Ltd. |
| Kymograph Reslice Wide Plug-in | MT Dynamics Analysis | Katrukha E. 2020 |
| GENtle | Sequence analysis | OpenSource |

| | | |
|---|---|---|
| SnapGene Viewer | Sequence analysis | OpenSource |

### 3.1.4. **Laboratory equipment**

**Table 13: List of laboratory equipment**

| Equipment | Notation | Company |
|---|---|---|
| Cell incubator | MCO-20AIC | PHCbi |
| Cell counter | TC20 | Bio-Rad |
| Cell counter slides | 145-0011 | Bio-Rad |
| Cell culture plates: | | |
| Well plates | 6-well, 24-well | Falcon |
| Flasks | T75, T25 | Falcon |
| Chambers | 35 mm high, grid-500 | Ibidi |
| Cell culture hood | Herasafe KS12 | Heraeus |
| Cell scraper | Blade 25 | Sarstedt |
| Centrifuges | Avanti J-20XPI | Beckman Coulter |
| | Centrifuge 5418 | Eppendorf |
| Coverslips (glass) | 631-1577, 12 mm | VWR |
| | 631-1584, 25 mm | VWR |
| Cryo container | Mr. Frosty | VWR |
| Electrophoresis chambers | MGV-620T | Beckman Coulter, |
| | SGE-020-02 | Beckman Coulter, |
| | E-H6 | Febicon |
| Forceps | BD047R | Aesculap |
| | FM002R | Aesculap |
| Heating block | Thermomixer Pro | Cell Media |
| Horizontal shaker | Unimax 1010 | Heidolph |
| Imaging system | ChemiDoc XRS | Bio-Rad |
| Microplate reader | Safire² | Tecan |
| Microscopes | Widefield fluorescence | Zeiss |
| | Axiocam 503 | Zeiss |
| | Eclipse Ti | Nikon |
| | UGA-40 illumination system | Rapp OptoElectronic |
| | Leica Dmi8 S Platform | Leica Microsystems |
| Microscope slides | 631-1553 | VWR |
| Microwave | R-898 (AL-)A | Sharp |
| PCR Plate (96-well) | MSP9601 | Bio-Rad |

| | | |
|---|---|---|
| Photometer | NanoDrop 1000 | PeqLab |
| Pipettes | 0.1 µl - 1000 µl<br>Research / Research plus<br>Pipetteboy accujet-pro | <br>Eppendorf<br>Integra Biosciences |
| Real-Time qPCR system | StepOnePlus System | TFS |
| Scales | EW 6000-1M<br>Analytical balance (fine) | Beckman Coulter<br>Sartorius |
| Thermocyclers | C1000 Touch | Bio-Rad |
| Vortex mixer | 444-1372 | VWR |
| Water bath | 1083 | GFL |

### 3.1.5. **Chemicals**

**Table 14: List of chemicals**

| **Chemical** | **Company** |
|---|---|
| Agarose | Sigma-Aldrich |
| Bovine Serum Albumin (BSA) | Sigma |
| Dimethyl sulfoxide (DMSO) | Sigma-Aldrich |
| Ethanol (≥ 99.5%) | AppliChem |
| Formaldehyde (FA, 37%) | AppliChem |
| Glycerol | AppliChem |
| Hydroxymethylaminoethane (Tris) | AppliChem |
| Phosphate buffered saline (PBS) | TFS |
| Sucrose | AppliChem |
| TBE buffer (10x) | AppliChem |
| Triton X-100 | AppliChem |

## 3.2. Methods

### 3.2.1. Cell culture

Both human SH-SY5Y neuroblastoma cells and human iPSCs were differentiated into neuronal cultures over two to three weeks. Cells were grown in 6-, 12-, or 24-well plates (VWR) and in imaging dishes (ibidi), with some containing coverslips (VWR) for microscopy. Unless indicated differently, volumes were 2 ml per well in 6-well plates, 1 ml in 12-well plates, and 0.5 ml in 24-well plates. Media were prewarmed to 37 °C, and cells were maintained at 37 °C in a humidified 5% $CO_2$ incubator.

#### 3.2.1.1 SH-SY5Y-derived neurons

##### 3.2.1.1.1 Preparation of cell culture plates:

Undifferentiated SH-SY5Y cells were maintained in uncoated T75 or T25 flasks (VWR). For neuronal differentiation, they were plated in culture dishes (VWR) pretreated with 20 µg/ml Poly-D-Lysine (PDL, AppliChem). The PDL solution was prepared by diluting a 1 mg/ml stock (1 ml) in 50 ml sterile DPBS (TFS). This coating mixture was applied to the plates and incubated for at least 3 h at 37 °C, after which it was removed and the wells were rinsed three times with DPBS. For imaging, glass coverslips (VWR) were placed in the wells (25 mm in 6-well plates, 12 mm in 24-well plates) before the coating was added.

##### 3.2.1.1.2 Cultivation, passaging and seeding

SH-SY5Y cells were passaged when reaching a confluence of about 80%. For cells grown in a T75 flask, the medium was removed and the culture was rinsed once with 5 ml DPBS. Cells were detached from the flask by adding 3 ml Trypsin/EDTA (0.05%) for 3-5 minutes. Trypsinization was monitored under bench-side microscopy and when finished, 7 ml of SHM-10 medium was added to stop the enzymatic reaction. The suspension was then transferred to a 15 ml Falcon tube and centrifuged at 1000 g for 3 minutes. After aspirating the supernatant, the pellet was resuspended in 10 ml SHM-10 medium. For passaging, the suspension was diluted 1:10 and placed into a fresh T75 flask containing 10 ml SHM-10 medium.

In order to passage SH-SY5Y cells for differentiation the same procedure was carried out one (d-1) or two days (d-2) before starting the differentiation (d0), but cells were seeded onto PDL-coated culture plates. Cells were counted and seeded with the desired density depending on the start of differentiation: on d-2 50.000 cells per well for a 6-well plate or an imaging dish or 10.000 cells per well for a 24-well plate and on d-1 75.000 cells per well for a 6-well plate or an imaging dish or 15.000 cells per well for a 24-well. SHM-10 medium was exchanged every 3 to 4 days.

#### 3.2.1.1.3 Neuronal differentiation of SH-SY5Y cells

Neuronal differentiation of SH-SY5Y cells were performed over a two-week period using sequential medium changes with retinoic acid (RA) and brain-derived neurotrophic factor (BDNF) supplements. On days 0, 3, and 5, SH-SY5Y cells were cultured in SHM-10 containing 10 µM RA. On day 7, the RA medium was removed, the cells were rinsed once with DPBS, and SHM-0 supplemented with 10 µM BDNF was added. A second exchange with SHM-0 + BDNF was performed on day 10. On day 14, the medium was switched back to unsupplemented SHM-10. Cultures were then maintained in SHM-10 with medium changes every three days and used for experiments for up to three weeks [3]. Differentiation efficiency yielded about 75% [195].

#### 3.2.1.1.4 Freezing

For later use, undifferentiated SH-SY5Y cells were cryopreserved. Cells were collected from T75 flasks following trypsinization and centrifugation, as described above. Cells were re-suspended in freshly prepared freezing medium (1 ml of freezing medium per cryovial), transferred rapidly into cryovials (Cryo.S™, Greiner Bio-One) and stored in a cryo container (Mr. Frosty™, VWR) to ensure a freezing rate of -1 °C / minute down to -80 °C. Cells were kept at -80 °C for long-term storage.

#### 3.2.1.1.5 Thawing

Frozen cells were thawed by placing the vials inside a water bath of 37 °C for one to two minutes. Cell suspension was rapidly transferred to 9 ml of SHM-10, spun down at 500 × g for three minutes, re-suspended in SHM-10 to desired density and seeded in T75 cell culture flasks (VWR), filled up with SHM-10 medium to a total volume of 10 ml.

### 3.2.1.2 Human induced pluripotent stem cell (iPSC)-derived neurons

Human iPSCs were differentiated into cortical glutamatergic neurons using a protocol modified from Wang et al. [3,186,187,201]. The WTC11 iPSC line used in this study contains a doxycycline-inducible Neurogenin-2 (*NGN2*) transgene. The forced expression of pro-neuronal transcription factor *NGN2* drives rapid neuronal conversion [186,202].

#### 3.2.1.2.1 Preparation of cell culture plates

Cell plates for undifferentiated iPSCs were coated with Geltrex (TFS) on the day of use. Notably, we found that storing well plates before seeding may significantly reduce cell survival during pre-differentiation. For coating, a 300 µl aliquot of Geltrex was thawed at 4 °C and diluted with 14 ml KnockOut DMEM (KO-DMEM, TFS) to a concentration of 200 µg/ml. 1 ml

(6-well plate or imaging dish) respectively 0.3 ml (24-well plate) of Geltrex coating solution were added per well and incubated for at least 30 minutes at 37 °C.

For cultivation of differentiating iPSCs, well plates were sequentially coated with PDL and Cultrex laminin (Biotechne) starting one day before the start of differentiation (d-1). Wells were coated with 20 µg/ml PDL in DPBS (as described for SH-SY5Y cells) and incubated at 37 °C overnight. On the next day, Cultrex laminin aliquots were thawed at 4° and diluted to 20 µg/ml in DPBS. PDL coating solution was removed, wells were washed once with DPBS and coated with the Cultrex laminin solution for another hour at 37 °C. Plates were used within 24 hours and washed twice with DPBS before seeding the iPSCs.

#### 3.2.1.2.2 **Cultivation, seeding and passaging**

For routine culture, undifferentiated iPSC colonies were cultured in cBrew on Geltrex-coated 6-well plates, with medium changed every two to three days. Spontaneously differentiating cells were removed manually before starting induced differentiation. Colonies were passaged at roughly 80% confluence.

For passaging, cells were rinsed with DPBS and incubated with 1 ml Versene (TFS) per well for 3-5 minutes at room temperature. After removing Versene, 1 ml cBrew was added, colonies were gently lifted with a scraper and collected in a 15 ml tube. Cell clumps were partially broken up by triturating with a Pasteur pipette. The cell suspension was diluted in cBrew at about 1:10, supplemented with Thiazovivin (1:5000), and replated. The next day, medium was replaced with cBrew without Thiazovivin. Cultures generally regained 80% confluence within 3-4 days.

#### 3.2.1.2.3 **Neuronal differentiation of iPSCs**

IPSCs were differentiated into cortical glutamatergic neurons using a predifferentiation phase (d-3 to d0) and a subsequent maturation period (d0 to d21 or longer).

On day -3, iPSCs were plated onto Geltrex-coated dishes. After one DPBS wash, 1 ml Accutase (Merck) was added per well and cells were incubated for 5-8 minutes at 37 °C. Dissociation was terminated by applying 3 ml DPBS, and cells were harvested, centrifuged at 400 g for 5 minutes, and resuspended in 1 ml cBrew. They were then diluted in predifferentiation medium to 1.5-2 x $10^6$ cells per well of a 6-well plate. Each well received 3 ml predifferentiation medium containing Thiazovivin (1:5000). Medium was exchanged on day -2 and day -1 using predifferentiation medium without Thiazovivin.

On day 0, cells were transferred to PDL/Cultrex-coated plates using the same Accutase dissociation and centrifugation steps, except that the pellet was resuspended in neuronal maturation medium (NMM). Cells were diluted in NMM freshly supplemented with Geltrex (1:100) to 0.5-0.8 x $10^6$ cells per well in 24-well plates or 2.5-4 x $10^6$ cells per well in 6-well plates or imaging dishes. Higher densities were used for transfection, transduction, or qPCR. Lower densities for ICC or live imaging. Half of the NMM volume was replaced weekly (d7, d14, d21) as cells differentiated into iPSC-derived neurons.

#### 3.2.1.2.4 **Freezing**

iPSCs were frozen when reaching a confluence of 70%. Dissociation with Versene and cell collection was carried out as described above, but without extensive triturating to preserve cell clumps. Each cryovial was filled up with 0.9 ml of cell suspension and another 0.9 ml of freshly prepared freezing medium was added. The cryovials were rapidly transferred to the freezing device and frozen at -80 °C for weekly storage or at -180 °C for long-term storage over multiple weeks.

#### 3.2.1.2.5 **Thawing**

Cryovials were thawed for 1-2 minutes in a 37 °C water bath and mixed rapidly with 10 ml of KO-DMEM. The suspension was centrifuged for 5 minutes at 400g, the supernatant aspirated and the cell pellet was dissolved carefully in 5 ml cBrew. 1 µl Thiazovivin was added to the 5 ml cell suspension (ratio 1:5000), which was then distributed on Geltrex-coated culture plates (2.5 ml cell suspension/well). On the following day the medium was exchanged to fresh cBrew.

### 3.2.1.3 **Primary mouse neurons**

Mouse primary forebrain neurons were extracted from embryonic FVB/N wild type mice at embryonic day 13.5 (E13.5). In brief, after removal of brainstem and meninges, cortices were digested with trypsin, and the resulting cell suspension was plated in prewarmed Neurobasal™ medium (TFS) supplemented with 1 % FBS, 1X penicillin/streptomycin and amphotericin B (Anti/Anti, TFS), 1X GlutaMAX™ (TFS) and 1X NS-21 (PAN Biotech). We refer to former studies for further details ([10,92]), as no cell culture work of primary mouse neurons was carried out by the author.

### 3.2.1.4 **Cell counting**

When passaging and seeding cells for differentiation, cells were counted by mixing cell suspension and Trypan Blue (Bio-Rad) in a ratio of 1:1. 10 µl of the dyed cell suspension were transferred into chambers of cell counting slides (Bio-Rad) and counted with an automated cell counter (TC20™, Bio-Rad). The desired cell density for the experiments was as follows:

- SH-SY5Y cells:
    - 75.000 cells/well for a 6-well plate or an imaging dish
    - 15.000 cells/well for a 24-well plate
- iPSC-derived neurons:
    - 250 - 400.000 cells/well in a 6-well plate or an imaging dish
    - 50 - 80.000 cells/well in a 24-well plate
- HEK-293T cells:
    - 4.000.000 cells/T75 flask

#### 3.2.1.5 **Transfection**

SH-SY5Y-derived neurons were transfected at day 7 using polymer-based PolyJet reagent (SignaGen). Half of the conditioned medium was first collected and kept at 37 °C/5% $CO_2$. For a well of a 24-well plate, 0.33 µg plasmid DNA was mixed with 25 µl DMEM (Mix A), and 1 µl PolyJet with 25 µl DMEM (Mix B). After combining Mix A and B and incubating for 10-15 minutes, the mixture was added dropwise to the cells. For 6-well plates or imaging dishes, 0.66 µg DNA with 50 µl DMEM and 2 µl PolyJet with 50 µl DMEM were used. After 3 hours, cells were rinsed with DMEM and returned to the collected medium supplemented with fresh SHM-10.

iPSC-derived neurons were transfected 2-4 days before experiments using LipoStem transfection reagent (TFS). As above, half of the conditioned medium was collected and kept at 37 °C/5% $CO_2$. For a well of a 24-well plate, 0.5 µg plasmid DNA in 25 µl Opti-MEM (Mix A) was combined with 0.5 µl LipoStem in 25 µl DMEM (Mix B) and incubated for 10 minutes. For 6-well plates or imaging dishes, 2.5 µg DNA in 125 µl Opti-MEM and 2 µl LipoStem in 125 µl DMEM were used. The mix was added dropwise and incubated for 24 hours. Cells were then rinsed with KO-DMEM and maintained in the stored medium topped up with fresh neuronal maturation medium.

#### 3.2.1.6 **Transduction**

For transduction of iPSC-derived neurons viral aliquots were thawed on ice and diluted with NMM to the desired concentration. The medium of the iPSC-derived neurons was collected, neurons were covered with the virus-containing medium (250 µl/well for a 24-well plate or 600 µl/well for a 6-well plate) and incubated overnight at 37 °C, 5% $CO^2$. After 16 hours the viral medium was aspirated, neurons were washed once with prewarmed KO-DMEM and the medium was changed back to virus-free maturation medium (½ conditioned medium from the previous day + ½ fresh medium). neurons were observed within the following days for detection of GFP under a fluorescence microscope.

Viral aliquots were thawed no more than two times, since multiple freezing/thawing cycles were reported to diminish the viral titer. The viral solutions were kept on ice after harvest and frozen within 10 minutes at -80 °C. Contact between the different viral constructs when pipetting was strongly prevented.

The optimal virus concentration was initially determined by performing a dilution series of different virus concentrations ranging from: 3:1 (virus:medium) to 1:100. For most constructs the optimal dilution ranged from 1:3 to 1:10 depending on the viral titer and the inserted construct. Notably, inserts within the transduced pLKO.3G vector reduced its transduction efficiency significantly compared to empty backbone viruses pUltra and pLKO.3G, so that higher viral concentrations were needed. Differentiated neurons tolerated transductions from day 4 onwards.

#### 3.2.1.7 **Transfection and transduction efficiency**

For quantification of transfection or transduction efficiency, neurons were fixed, stained with DAPI, imaged under fluorescence microscopy and counted. Successful transfection or transduction resulted in detectable fluorescence from GFP (pRNAT, pLKO3.G, pUltra) or tdTomato (p_tdTomato). The efficiency was calculated as follows:

$$\%\ \boldsymbol{transduced\ cells} = \left(\frac{\boldsymbol{fluorescent\ cells}}{\boldsymbol{DAPI + cells}}\right)\boldsymbol{x100}$$

The transfection efficiency depended on the used plasmid and target cell type: ~10% for tdTomato and empty pRNAT, ~0.01% for pRNAT-T1, -T2, -A1, -A2 (see Fig. 3.1).
The transduction efficiency depended also on the viral titer used (see Fig. 3.2). Using 1:3 viral dilution we yielded a transduction efficiency of ~99% for pUltra and ~98% for shRNA-carrying pLKO.3G plasmids.

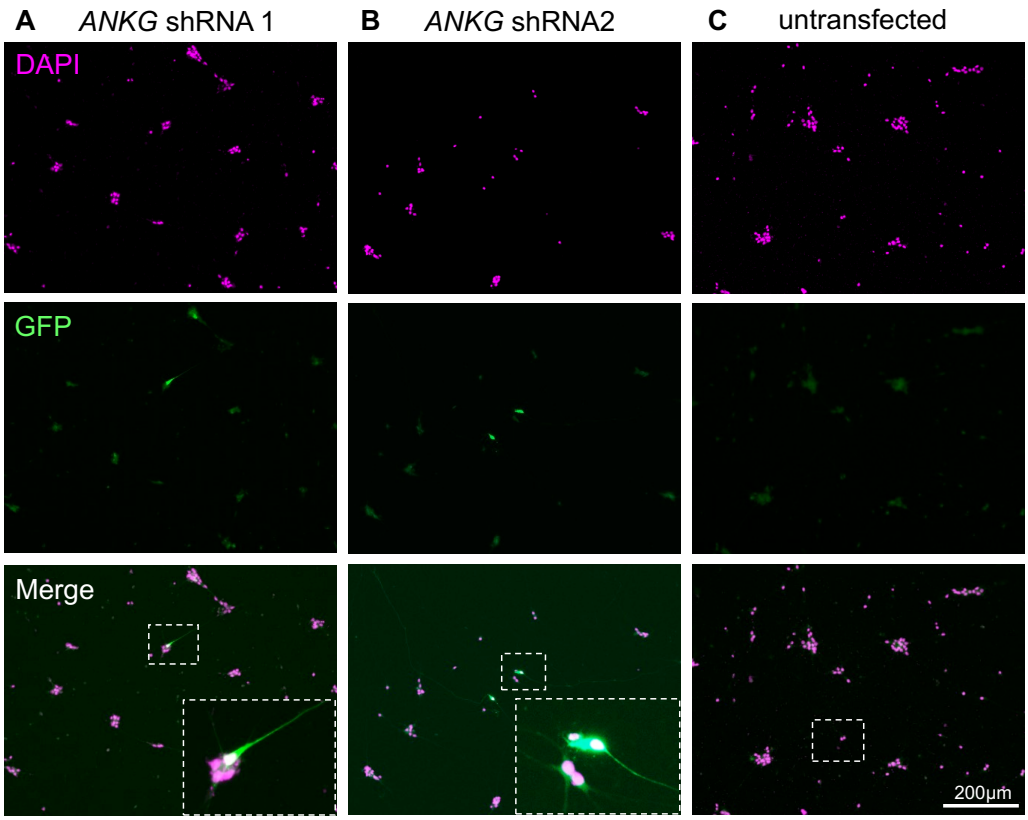


**Figure 3.1: shRNA-mediated *ANK3 knock*down via transfection in iPSC-derived neurons.**
Representative images of iPSC-derived neurons transfected with pRNAT vector with *ANK3 shRNA* 1 (A) and 2 (B) insert, compared to untransfected control (C). GFP+ cells (green) indicate transfected cells, DAPI staining (magenta) marks the nucleus of all cells. Successfully transfected neurons appear with white nucleoli in the merged image. (see magnification A-B) Note only two single GFP+ cells in A-B.

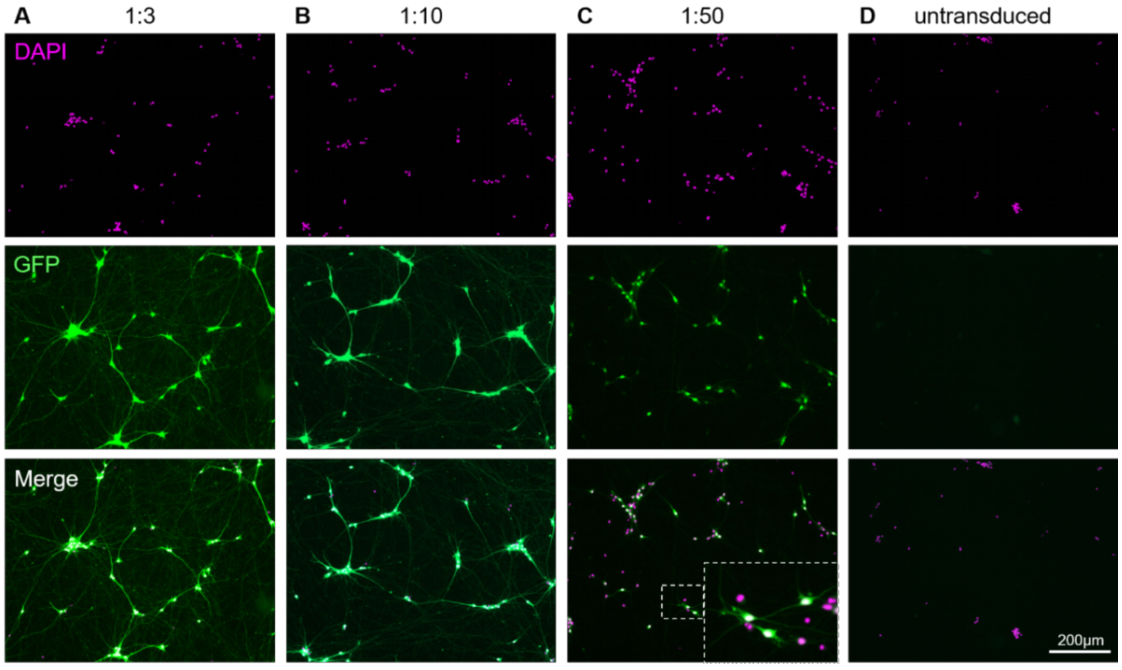


**Figure 3.2: shRNA-mediated *ANK3 knock*down via lentiviral transduction in iPSC-derived neurons.**
Representative images of iPSC-derived transduced with pLKO.3G plasmid with *ANK3 shRNA*1 insert in different dilutions. GFP+ cells (green) indicate transduced cells, DAPI staining (magenta) marks the nucleus of all cells. Successfully transduced neurons appear with white nucleoli in the merged image. Note decreasing transduction efficiency from A-D: 98% (A), 91% (B), 30% (C), 0% in untransduced cells (D).

### 3.2.2. **Imaging methods**

#### 3.2.2.1 **Immunofluorescence experiments**

For fixation, cells medium was either replaced by 3.7% paraformaldehyde (PFA) in PBS or 7.4% PFA was added directly to the well to reach a final concentration of 3.7%. After an 18-minute incubation, samples were either stored in 55% glycerol/PBS at -20 °C or washed three times with PBS for immediate staining.

For immunofluorescence, PFA or glycerol solution was removed and cells, followed by three PBS washes and a 10-minute incubation in blocking/permeabilization solution. After another PBS wash, primary antibodies diluted in PBS were applied by placing the coverslips face-down on drops of antibody solution on parafilm. Coverslips were kept overnight at 4 °C in a dark, humid chamber.

The following day, after three PBS washes, coverslips were incubated another three hours with secondary antibodies in the dark. After three more PBS washes, nuclei were stained with Hoechst 33342 (one drop/ml, NucBlue™, TFS) for 25 minutes at room temperature. Coverslips were rinsed twice with deionized water, mounted with Poly-Mount (Polysciences), dried for at least 24 hours, and stored at 4 °C until imaging.

The same washing and staining steps were performed for cells in imaging chambers, except for direct application of antibody solutions into the chambers instead of flipping the coverslips onto the antibody solutions on a parafilm surface.

#### 3.2.2.2 **Fluorescence microscopy**

Fluorescence images were acquired using a widefield microscope (Zeiss) equipped with a Colibri 7 LED light source (Zeiss) and an Axiocam 503 fluorescence camera (Zeiss). Imaging was performed with the Zen Blue Pro software (Zeiss). Magnifications of 200×, 400×, and 630× were obtained using 10×, 20×, and 40× air objectives, as well as a 63× oil-immersion lens (Immersol 518F, Zeiss). Exposure settings and illumination intensity were adjusted to avoid signal saturation, and identical parameters were maintained within each experiment for reliable fluorescence quantification.

#### 3.2.2.3 **Live-cell imaging**

To analyze microtubule dynamics by live imaging, SH-SY5Y- and iPSC-derived neurons were transfected with a tdTomato-EB3 plasmid (p_tdTomato-EB3) using the protocols described in section 3.2.1.5 [3,187]. SH-SY5Y cells were transfected on day 7 and imaged on days 14-18, whereas iPSC-derived neurons were transfected on days 12-15 and imaged on days 16-18. Fluorescent EB3-tdTomato signals typically appeared after 2-3 days.

EB3 comet movement was recorded on a Leica DMi8 S Platform microscope with a DFC9000 camera using Las X Life Sciences software (Leica Microsystems). Throughout imaging, precautions were taken to limit cell stress caused by mechanical manipulation, changes in temperature or $CO_2$ levels and illumination. Before preparing cells, the microscope was set to 37 °C with 5% $CO_2$ and equipped with the appropriate specimen holder.

Cells grown in glass-bottom imaging dishes were placed directly on the stage, whereas coverslips from 6-well plates were transferred into a live-cell chamber (ALA Scientific) filled up with 250-500 µl medium. Samples were kept under the incubation hood and light-protected for 15 minutes before imaging.

EB3-tdTomato comets were visualized using a 555 nm laser. A 40x air objective was used for initial assessment of transfection efficiency and cell viability, and a 63x water-immersion lens for recording of EB3-tdTomato comets. Time-lapse videos were captured at one frame every 2 seconds for 2 minutes. Exposure settings and excitation intensity were minimized to avoid photobleaching, and spatial binning (e.g., 2×2) was used to improve sensitivity. Autofocus maintained a stable z-position during acquisition [3,187].

### 3.2.3. **Data analysis**

#### 3.2.3.1 **EB3 microtubule analysis**

The video recordings were acquired using LasX, followed by analysis and quantification in ImageJ/Fiji. A 30 µm linear region of interest (ROI) was defined along the proximal axon and dendrite, and a 50-200 µm ROI along the distal axon (≥400 µm from the soma). Kymographs of EB3 comet movement were generated with the Kymograph Reslice Wide plugin and evaluated for comet number per 30 µm/min, direction (anterograde or retrograde), and speed (µm/s), with speed derived from the slope of each comet track [3,187].

For comparison of MT dynamics across neuronal compartments, we distinguished axons and dendrites using morphological features and immunolabeling. Axons were identified based on established morphological features such as smaller diameter, greater length, distal branching, and characteristic 90° branch points [203]. When morphology was uncertain, cells were stained for axonal (AIS proteins TRIM46 and ANKG) or somatodendritic markers (MAP2) after the live-cell imaging. To do so, the x/y-coordinates of each filmed cell within the gridded imaging chamber were registered, cells were fixed and immunostained and relocated under a fluorescence microscope and then checked for the actual identity of the imaged neurites.

### 3.2.3.2 **AIS development**

To analyze the abundance of AIS proteins iPSC-derived neurons were fixed and stained for TRIM46, ANKG and MAP2 at multiple timepoints during the differentiation: d3, d5, d7, d10, d14, d17 and d21 after starting differentiation. An 80 µm line ROI was drawn along the beginning of the axon and measured for its fluorescence intensity. To exclude background noise, the fluorescence intensity of an identical ROI next to the neurite was subtracted from the axonal fluorescence intensity.

For each timepoint, fluorescence intensities of the three experimental replicates were averaged. Additionally, the fluorescence intensities for each timepoint were normalized to the maximum of day 17 (Fig. 5.1). To ensure comparability of fluorescence intensities replicates from the different timepoints were stained simultaneously with the same antibody solutions, blocking and incubation time.

### 3.2.3.3 **AIS enrichment factor (AIS EF) for TRIM46 and ANKG**

To assess TRIM46 and ANKG enrichment at the AIS, we calculated a ratio between peak fluorescence intensity and baseline fluorescence within the first 80 µm of the axon, termed AIS enrichment factor (AIS EF). The peak intensity ($MFI_{peak}$) was defined as the mean of all values exceeding 70% of the maximal signal across the peak region of length x. The baseline intensity ($MFI_{baseline}$) was obtained from the mean fluorescence over the same distance x at the distal end of the 80 µm ROI. The AIS EF was then calculated as AIS EF = $MFI_{peak}$ / $MFI_{baseline}$ for TRIM46 and ANKG respectively [3].

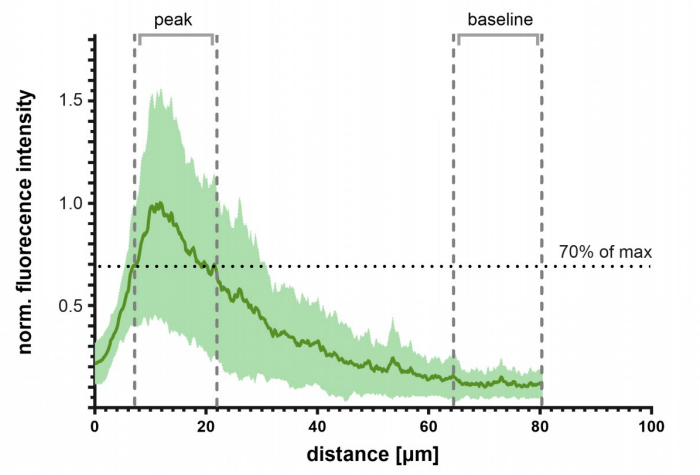


**Figure 3.3: Calculation of the AIS enrichment factor.**

### 3.2.3.4 **Axonal enrichment factor (AEF) for TAU and MAP2**

To asses the axonal enrichment of TAU and MAP2 relative to the soma, we calculated an axonal enrichment factor ($AEF_{TAU}$, $AEF_{MAP2}$). Mean fluorescence intensity (MFI) were measured in ROIs drawn in the soma ($MFI_S$), axon ($MFI_A$) (>100 µm distal from the AIS) as

well as in adjacent background regions near the soma ($MFI_{bgS}$) and axon ($MFI_{bgA}$), to normalize for background noise. The soma ROI was positioned to avoid nuclear fluorescence. To correct for background signal, we subtracted $MFI_S$ - $MFI_{bgS}$ (=$MFI_{Soma}$), respectively $MFI_A$ - $FI_{bgA}$ (=$MFI_{Axon}$). Axon-to-soma ratios were then calculated ($MFI_{Axon}$ /$MFI_{Soma}$) for TAU and MAP2 seperately. To correct for volume-related differences in fluorescence, these ratios were normalized to the axon-to-soma ratio of a uniformly distributed volume marker (tdTomato or GFP) (e.g., $AEF_{Tau} = \frac{(\mathrm{MFI}_{Axon}/\mathrm{MFI}_{Soma})_{Tau}}{(\mathrm{MFI}_{Axon}/\mathrm{MFI}_{Soma})_{tdTomato}}$ ). Identical ROIs were used for TAU, MAP2, tdTomato and GFP [3].

### 3.2.4. **Microbiology methods**

#### 3.2.4.1 **Cloning**

##### 3.2.4.1.1 **Design of shRNAs**

ShRNAs for knockdown of *TRIM46* and *ANK3* were designed with the shRNA design tools of NCBI Primer Blast [204], Broad Institute [205] and TFS BLOCK-iT™ RNAi Designer [206]. Constructs were designed so that they covered all human isoforms of TRIM46 (NM_025058.5, NM_001256599.2, NM_001256601.1, NM_001282378.2) and ANKG (NM_020987.5, NM_001149.4, NM_001204403.2, NM_001320874.2, NM_001204404.2), found within the RefSeq mRNA Database [207]. The shRNA length ranged from 19 to 21 nucleotides, which were combined with a 5' restriction site for BamHI, a 6 nt connecting loop sequence and a 3' restriction site for HindIII to enable annealing and integration into digested pRNAT vector. When designing shRNA sequences for lentiviral pLKO.3G vector the 5' loop sequence and the restriction sites were fitted to EcoRI and the 3' restriction site to PacI.
Primers were tested for predicted self-annealing and dimerization with OligoCalc [208]. For *TRIM46* and *ANK3 knock*down, two, respectively four shRNAs were designed and cloned into the respective plasmid.

##### 3.2.4.1.2 **Digestion of vectors**

For the digestion of 1 µg of pRNAT / pLKO.3G* vector the following reaction mix was created.

| **Component** | **Amount** |
|---|---|
| pRNAT vector / pLKO.3G* | X µl ≙ 1 µg |
| CutSmart Buffer | 5 µl |
| BamHI / EcoRI* | 1 µl |
| HindIII / PacI* | 1 µl |
| dd$H_2O$ | X µl up to total reaction volume of 50 µl |

| | |
|---|---|
| **Total volume** | **50 µl** |

The reaction mix was incubated for 60 minutes at 37 °C followed by 20 minutes at 65 °C for heat inactivation.

#### 3.2.4.1.3 Gel Electrophoresis

The reaction mix for vector digestion was run on 0.7% agarose gel to isolate the digested vector. 0.7 g agarose was dissolved in 100 mL 1x TBE buffer and boiled for 2 to 3 minutes in a microwave until the agarose was dissolved. The gel solution was cooled down and 8 µl of GelRed (Biotium) were added. The gel solution polymerized in a gel chamber with a 12 mm comb within 30 to 45 minutes. The comb was removed and the chamber was filled with 1x TBE buffer until the electrodes were covered. The digested vector solution as well as the undigested vector as a negative control were mixed with purple Gel loading dye (Biolabs) in a ratio of 1:6. The undigested vector, the digested vector and a Quick-Load® 1 kb Plus DNA Ladder were loaded into the pockets of the gel and were run at a voltage of 120 V for 20 to 30 minutes. Afterwards the separated components were visualized under UV light, cut out and purified with NucleoSpin™ Gel & PCR Clean up Kit (Macherey Nagel) according to the manufacturer's protocol.

#### 3.2.4.1.4 Annealing of oligonucleotides

For annealing the corresponding oligonucleotides of the sense and antisense strand, 5 µl of each 100 µM oligonucleotide were joined to create a premix. The complementary annealing was performed with the following reaction mix.

| **Component** | **Amount** |
|---|---|
| Oligonucleotide premix (sense + antisense) | 2 µl |
| 10x T4 Ligase Buffer NEB | 1 µl |
| $ddH_2O$ | 7 µl |
| **Total volume** | **10 µl** |

The reaction mix was incubated at 95 °C for 5 minutes with subsequent cooling to 45 °C at a cooling rate of 5 °C/min on a thermocycler.

#### 3.2.4.1.5 Ligation of shRNA insert and digested vector

Annealed oligonucleotides (see 3.2.4.1.4) were diluted 1:100 in $ddH_2O$. They were integrated into the digested vector by creating the following reaction mix. The T4 Ligase was added last to the reaction mix.

| Component | Amount |
|---|---|
| Annealed oligonucleotide dilution (1:200) | 1 µl |
| Digested vector (pRNAT or pLKO.3G) | X µl ≙ 50ng |
| 10x T4 Ligase Buffer (TFS) | 1 µl |
| T4 Ligase (TFS) | 1 µl |
| $ddH_2O$ | X µl up to total reaction volume of 10 µl |
| **Total volume** | **10 µl** |

The reaction mix was left for 30 minutes at room temperature to achieve ligation.
A reaction mix was setup with the undigested vector which would function as a negative control during the following steps.

#### 3.2.4.1.6 Transformation and plating of bacteria

To amplify the generated vector containing the shRNA construct of interest, one had to transform it into chemically competent bacteria. Chemically competent *E. coli* TOP10 bacteria were thawed on ice for 15 minutes. For each vector, 50 µl of ice-cold bacteria were mixed with 6 µl of ligated vector or undigested vector reaction (negative control) in an Eppendorf tube and incubated for 15 to 20 minutes on ice. Afterwards the mixture was placed into a 42 °C water bath for 45 seconds. This “heat shock” allowed the transfer of DNA into the bacteria via transformation. The tubes were put back on ice to cool down and 1 ml of prewarmed LB medium was added. The transformed bacteria were grown in a 37 °C shaking incubator for 45 to 60 minutes.
The bacterial suspension was spun at 4000g for 4 minutes. After removing 950 µl of the supernatant, the bacterial pellet was resuspended in the 150 µl of residual medium. The concentrated bacterial suspension was evenly spread on agar plates containing 100 µg/ml Ampicillin with a spatula. The plates were incubated for 16 to 18 hours at 37 °C.
All work with bacteria was performed close to a Bunsen burner flame to prevent contamination.

#### 3.2.4.1.7 Plasmid amplification and sequencing

After 16-18 hours bacterial colonies were observed on the agar plates. Approximately 4 colonies per plate were picked and 5 ml of LB media containing 0.1% Ampicillin was inoculated with each colony in a 15 ml tube. Bacteria within the tubes were grown again for 16-18 hours in a shaking incubator at 37 °C at a speed of 210 rpm.
For extraction of the amplified vector of interest from the grown bacterial suspension PureYield™ Plasmid Miniprep System (Promega) was used following the manufacturer’s protocol. At the end, the concentration of the eluted plasmid was measured with NanoDrop photometer (PeqLab) and was sequenced by Microsynth Seqlab (Göttingen, Germany).

Sequence results were checked for successful shRNA integration into the desired vector using the software GENtle and SnapGene Viewer.
A glycerol stock for backup storage of the bacterial colony was created by mixing 500 µl of the 5 ml bacterial suspension (see above) with 500 µl of glycerol and stored at -80 °C, so that the plasmid could be reproduced and extracted at later times.
To yield a higher amount of the desired plasmids, 1 ml of the 5 ml bacterial suspension or one tip of its glycerol stock were used to inoculate 50 ml of LB medium with 0.1% Ampicillin. Afterwards, the plasmid DNA was extracted from bacteria by performing "MidiPrep" with PureYield™ Plasmid Midiprep System (Promega) according to the manufacturer's protocol. For pLKO.3G with integrated shRNA the plasmid was extracted from a bacterial suspension of 250 ml volume using PureYield™ Plasmid Maxiprep System. The eluted plasmid was stored at -20 °C for long-term use.

#### 3.2.4.2 Lentiviral production

pLKO.3G is a lentiviral vector designed for expressing shRNA via transduction in cells of interest. It contains a GFP tag that allows to visualize transduced cells and determine transduction efficiency. In order to produce lentiviral particles with the shRNA of interest, one had to express pLKO.3G containing the shRNA with a packaging and an envelope plasmid in HEK-293T cells (GenHunter #Q401). Lentiviral particles can be collected from the media of infected HEK-293T cells and be used later on to transduce the target cells by adding it directly to their medium.

##### 3.2.4.2.1 Cloning of pLKO.3G with shRNA inserts

Cloning of pLKO.3G was performed as described above (see 3.2.4.1). Loop and restriction sites were adapted to pLKO.3G specific sequences. When performing transformation and amplification it is recommended to use *E. coli* TOP10 instead of *E. coli* Stbl3 to yield a higher concentration of the pLKO.3G plasmids.

##### 3.2.4.2.2 Production of virus particles

For each plasmid to be produced one T75 flask of HEK-293T cells was seeded and cultivated in 10 ml of HEK-293T cell medium at 37 °C, 5% $CO^2$ overnight in a sterile incubator. The density and day of seeding was chosen so that HEK-293T cells would reach a confluence of 60-70% on the day of transfection (day 1).
On day 1 the HEK-293T cells were transfected with the shRNA-containing pLKO.3G, the envelope vector pMD2.G and the packaging vector psPAX2 using polyethylenimine (PEI) transfection reagent (Polysciences). The following amounts of plasmids, transfection reagent and medium were used to create the transfection mix:

| Component | Amount |
|---|---|
| pLKO.3G | 10 µg |
| psPAX2 | 9 µg |
| pMD2.G | 1 µg |
| PEI transfection agent | 20 µl |
| DMEM (serum-free, antibiotic-free) | X µl up to total volume of 400 µl |
| **Total volume** | **400 µl** |

The transfection mix was incubated for 20 minutes at room temperature. The HEK-293T cells were washed once with PBS and covered with 5 ml of new medium. The transfection mix was added to HEK-293T cells and they were further incubated for 12-15 hours at 37 °C, 5% $CO^2$ in a sterile incubator. On day 2, 3 ml of fresh HEK-293T medium were added to the cells without removing the medium from the previous day. On day 3, the whole medium was aspirated and changed to 10 ml of fresh HEK-293T medium. On day 4 and 5, the virus was harvested by collecting the medium from the infected HEK-293T cells.
To ensure that HEK-293T cells were infected, cells were inspected under fluorescence bench-side microscope, detecting green fluorescence among the infected cells. The viral medium covering the HEK-293T cells was collected from the T75 flasks and transferred into a 15 ml falcon. The medium was then centrifuged for 4 minutes at 400g and filtered through a 0.45 µm filter to remove any remaining cells. The cell-free virus solution was then aliquoted in 1 ml Eppendorf tubes and stored immediately at -80 °C. HEK-293T cells were again covered with 8 ml of HEK-293T medium and incubated overnight so that virus could be harvested on day 5 in the same way as on day 4 from the HEK-293T medium. All work from day 1 on was performed under S2 safety regulations.

#### 3.2.4.3 **qPCR**

We carried out a quantitative RT-qPCR to evaluate the expression of *TRIM46* and *ANK3* in different cell types and in iPSC-derived neurons subjected to knockdown via lentiviral transduction. Cells were harvested, lysed and total RNA was isolated, which was then converted into cDNA via reverse transcription. The transcribed cDNA and gene-specific primers were used to quantify mRNA levels of *TRIM46* and *ANK3* in qPCR. The *HPRT* gene was used to normalize expression during analysis.

##### 3.2.4.3.1 **Cell harvest**

HEK-293T cells, undifferentiated SH-SY5Y cells, SH-SY5Y-derived neurons, transduced iPSC-derived neurons and non-transduced wildtype (WT) iPSC-derived neurons were harvested for qPCR. For each experimental condition at least 2-3 wells of a 6-well plate were

harvested. To do so, cell medium was aspirated and each well was filled with 2 ml ice cold DPBS. Cells were detached using a cell scraper and the cell suspension was filled into a 15 ml tube. The tubes were centrifuged for 5 minutes at 2500g, the supernatant was discarded and cell pellets were stored at -80 °C.

#### 3.2.4.3.2 RNA isolation

Cell lysis and RNA isolation was carried out using PureLink RNA Mini Kit (TFS). The isolated RNA was eluted in 60-80 µl nuclease free water and the concentration was measured with NanoDrop photometer. The RNA was stored at -80 °C until proceeding with cDNA synthesis.

#### 3.2.4.3.3 cDNA synthesis

The isolated RNA was transcribed into cDNA using ProtoScript II First Strand cDNA Synthesis Kit (NEB) following the manufacturer's protocol. From each sample 200-400ng of RNA were transcribed. Furthermore "No reverse transcriptase" (No RT) controls were set up to assess undesired cDNA contamination of the probes. The reaction mix from the kit was run on a thermocycler for 5 minutes at 25 °C, 1h at 42 °C and 5 minutes at 80 °C.

#### 3.2.4.3.4 Primer design

Several matching primers for *TRIM46* and *ANK3* were designed and tested before using one suiting set for amplification of the cDNA in the final qPCR. The NCBI Primer Blast website [204] was conducted to generate primers with a PCR product size of 80-200 base pairs, spanning exon-exon junctions and covering the mRNAs of all human isoforms of the target proteins. For *TRIM46*, 8 primer sets and for *ANK3* 4 primer sets were tested for proper amplification in normal PCR, aiming to generate one single band with the expected size without amplification in the "No RT" control. For primer control, cDNA generated from wildtype iPSC-derived neurons at d11 of differentiation was used.

The following reaction mix for PCR was setup:

| **Component** | **Amount** |
|---|---|
| 10x Taq Buffer | 5 µl |
| 50 mM MgCl2 | 1.5 µl |
| dNTPs | 1 µl |
| Forward Primer | 1 µl |
| Reverse Primer | 1 µl |
| DMSO | 1 µl |
| Taq Polymerase | 0.5 µl |

| | |
|---|---|
| $ddH_2O$ | 34 µl |
| cDNA template | 5 ng (here ≈ 1 µl) |
| **Total Volume** | **46 µl** |

The PCR reaction was run on a thermocycler with the following program:

| Temperature (C) | Time | Number of Cycles |
|---|---|---|
| 95° | 0:30 min | 1 |
| 95° | 0:10 min | 30 |
| 58.5° | 0:30 min | |
| 68° | 1:00 min | |
| 68° | 5:00 min | 1 |
| 4° | ∞ | |

The PCR products were mixed with purple Gel Loading dye and loaded onto a 2% agarose gel. Gel electrophoresis was run for 25 min at 120V. The resulting bands on the agarose gel were analyzed under UV light to meet the above-mentioned criteria.

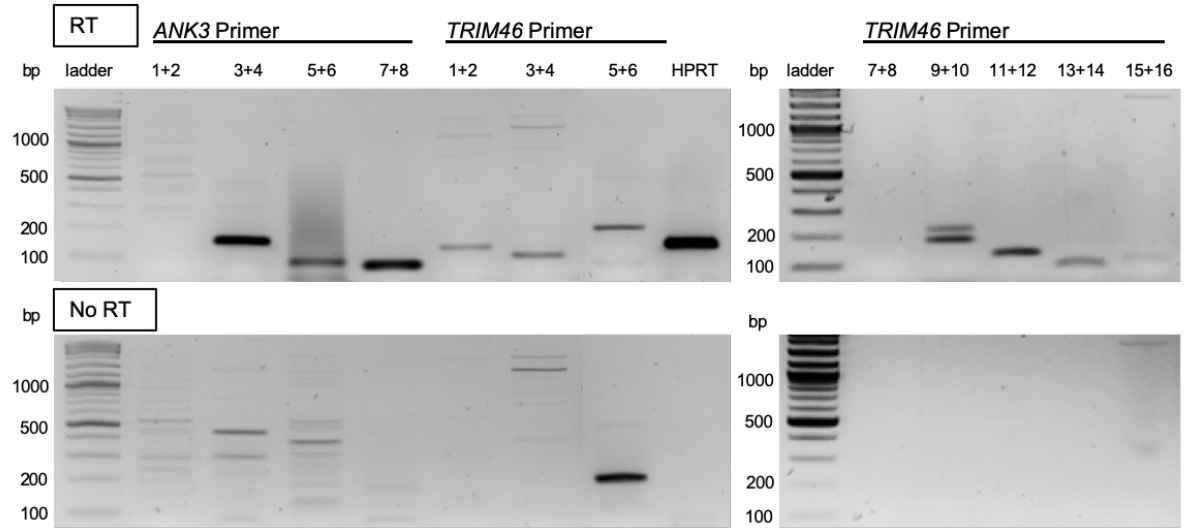


**Figure 3.4: Primer design for *ANK3* and *TRIM46* qPCR.**
Gel electrophoresis of different primer sets for *ANK3* and *TRIM46* qPCR. Upper panels: samples derived from cDNA synthesis with reverse transcriptase (RT). Lower panels: samples from cDNA synthesis without reverse transcriptase (No RT) to exclude genomic DNA contamination (see 3.2.4.3.4). Primer set 7+8 was chosen for *ANK3* qPCR. Primer set 9+10 was chosen for *TRIM46* qPCR.

### 3.2.4.3.5 **RT-qPCR**

Transcribed cDNA and previously tested gene-matching primer sets were used to assess gene expression of *TRIM46* and *ANK3* in qPCR with nucleic acid stain SYBR green (TFS). For each sample, 3 technical replicates were used. A “No RT” and a water control (no cDNA) were used

as negative controls. Furthermore, the expression of *HPRT* as a reference gene was included for relative quantification.

The following reaction mix was set up for qPCR:

| **Component** | **Amount** |
|---|---|
| 2x SYBR green Mix | 6.25 µl |
| Forward Primer | 0.5 µl |
| Reverse Primer | 0.5 µl |
| dd$H_2O$ | 1.25 µl |
| cDNA | 3.0 µl |
| **Total Volume** | **11.5 µl** |

Each reaction mix was pipetted into a well of a 96x0.1 mm well plate (Bio-Rad), which was then sealed with foil and shortly centrifuged. The plate was inserted into StepOnePlus Real Time PCR System (Applied Biosystems) which recorded fluorescence intensity during PCR with StepOne Software.

#### 3.2.4.3.6 Quantification

The Cycle threshold (Ct) values from qPCR were analyzed using the ΔΔCt formula method to assess *TRIM46* and *ANK3* expression. For relative quantification the reference gene *HPRT* was used.

1. An average Ct of the 3 technical replicates was calculated.
2. The Ct value of the target gene (*ANK3* or *TRIM46*) was normalized to the Ct value of the reference gene (*HPRT*):
   - $\Delta Ct = Ct(gene\ of\ interest) - Ct\ (HPRT)$
3. The Ct value of each sample was normalized to the Ct value of the reference sample (WT iPSC-derived neurons):
   - $\Delta\Delta Ct = Ct(sample) - Ct\ (WT\ iPSC)$
4. The fold gene expression was calculated as:
   - $fold\ gene\ expression = 2^{-\Delta\Delta Ct}$

# 4. Results

## 4.1. AIS development in iPSC-derived neurons

Human iPSC-derived neurons are essential to study human TAU and the involvement of the AIS in TAU (mis)sorting. However, the temporal course of initial polarization and AIS assembly, especially of TRIM46, in iPSC-derived neurons are understudied. Here, we provide a basic characterization of AIS development during neuronal differentiation in *NGN2*-induced iPSC-derived neurons, enabling comparisons to corresponding developmental stages in conventional animal models.

We differentiated human iPSCs into neurons using a doxycycline-inducible *NGN2* protocol with sequential subplating and media changes (see 3.2.1.2). To track AIS development over three weeks, neurons were fixed at days 3, 5, 7, 10, 14, 17, and 21, and stained for somatodendritic marker MAP2, as well as AIS markers TRIM46 and ANKG. The fluorescence intensity (F.I.) was measured along the first 80 µm of the axon and averaged per time point. An AIS enrichment factor (AIS EF) was calculated to quantify local TRIM46/ANKG accumulation relative to baseline (see 3.2.3.3.). In addition, MAP2 intensity 60-80 µm distal to the soma was averaged to assess its axonal presence.

On day 3 and 5, TRIM46 and ANKG signals were similarly low. While an overall average faint staining (maximum of 0.21 for TRIM46 and 0.27 relative F.I. for ANKG on day 5) among the neurons was visible in the immunostaining (Fig. 4.1.A, B), the AIS proteins did not show a marked enrichment (AIS $EF_{TRIM46}$ of 1.26 on day 3; 1.27 on day 5, AIS $EF_{ANKG}$ of 1.76 on day 3; 1.88 on day 5) at the outgrowing neurite at these time points (Fig. 4.1.C, D). Moreover, MAP2 was present in these neurites with the highest baseline intensity (0.14 ± 0.05 norm. F.I.) relative to later developmental stages (Fig. 4.1.E). After one week (d7), neurites grew progressively and MAP2 immunoreactivity decreased along the neurite (baseline intensity: 0.10 ± 0.01 norm. F.I.), while AIS protein levels remained low and showed no proximal enrichment (AIS $EF_{TRIM46}$ of 2.93, AIS $EF_{ANKG}$ of 4.11).

From day 10 on, TRIM46 and ANKG showed progressive enrichment at the proximal axon (Fig. 4.1.A-D), while MAP2 was gradually excluded from the axon (Fig. 4.1.E).

The TRIM46 fluorescence intensity increased steadily from 0.51 relative F.I. on day 10 to the maximum of 1.1 on day 21 (Fig. 4.1.B), with a maximum enrichment factor of 7.8 on day 17 (Fig. 4.1.C). The ANKG fluorescence intensity augmented equally from 0.72 relative F.I. on day 10 to a maximum (1.0) on day 17, with a moderate decrease to 0.79 on day 21 (Fig. 4.1.B). Local enrichment of ANKG at the AIS was also strongest on day 17, with levels being 7.3 times higher in the proximal axon than in the distal part (Fig. 4.1.D).

Importantly, the axonal presence of MAP2 decreased with increasing maturation: The baseline MAP2 intensity was decreased more than 3-fold from d5 to d17 (0.04 ± 0.03 norm. F.I.) (Fig.

4.1.E). The separation of the axonal and somatodendritic compartment in the differentiated and polarized iPSCs is represented by a marked green/red border of the TRIM46 and MAP2 immunostainings (Fig. 4.1.A, right panels).

Morphologically, the AIS in iPSC-derived neurons resembled those known from primary rat hippocampal neurons [49,58,75] or primary mouse neurons (see Fig. 4.2) in terms of length and localization: It typically began approximately 5-10 µm from the soma and extended 30-40 µm along the proximal axon, with peak TRIM46 and ANKG signal intensity occurring about 10-15 µm distal to the soma. Furthermore, the TRIM46 peak was located slightly more proximal at the AIS than the ANKG maximum. Among the differentiated iPSC-derived neurons of day 17 the TRIM46 peak localized at 10.25 µm, 1.2 µm more proximal than the ANKG peak at 11.46 µm distal from the soma. A similar distance between the TRIM46 and ANKG maximum of 1.8 µm was observed at neurons on day 14 and day 10. IPSC-derived neurons frequently developed more than one axon featuring a classic AIS, observed in 25% of neurons at day 21, as exemplified in Fig. 4.1.A, d17 (for quantification see Fig. 4.3.C).

Taken together, human *NGN2*-induced iPSC-derived neurons establish an AIS within the first +/- 40 µm of the proximal axon, shown by the local abundance of AIS markers TRIM46 and ANKG. Both AIS proteins show a coordinated increase in abundance starting between day 7 and 10, with a continuous rise until day 17.

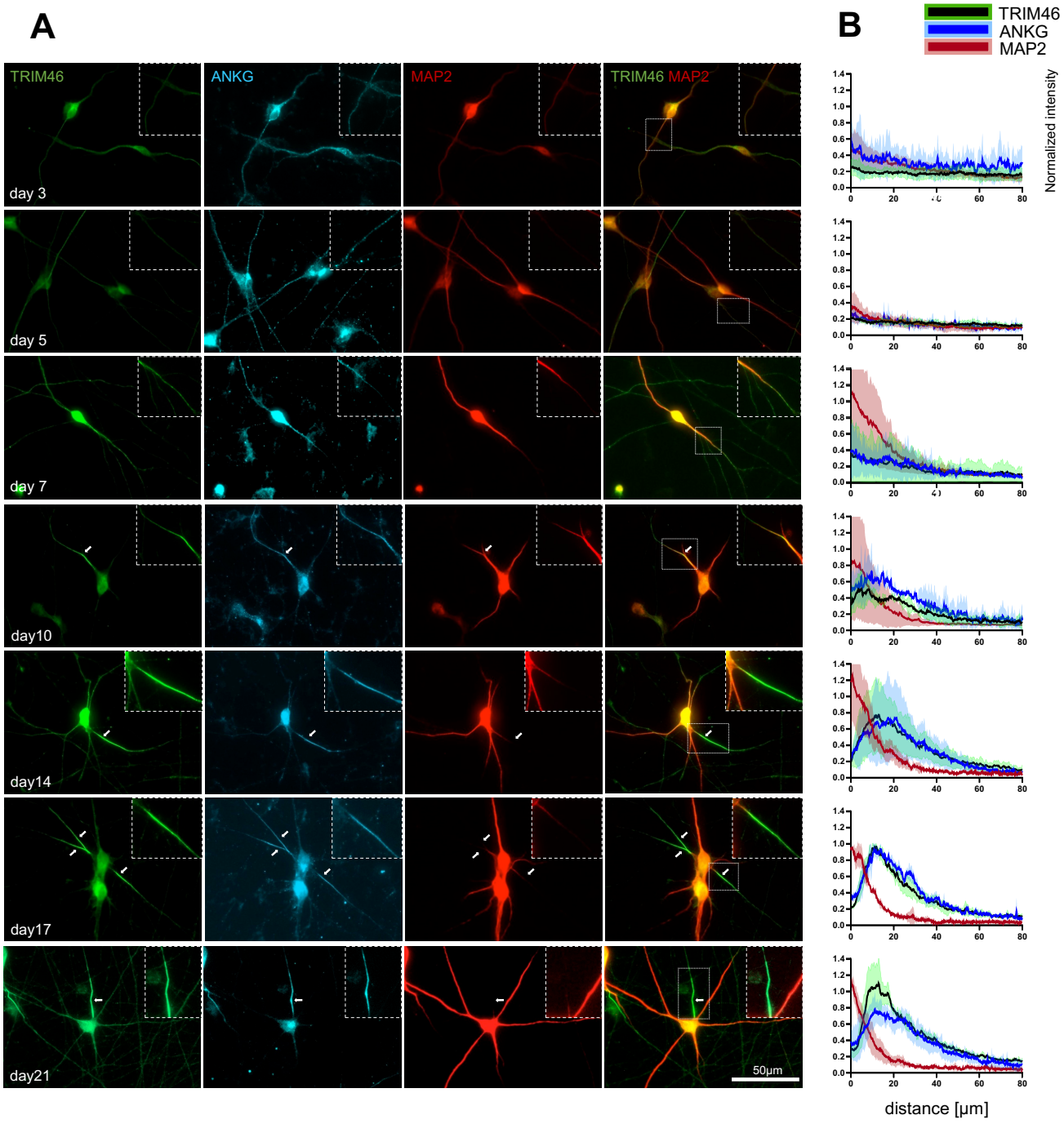
A
TRIM46
ANKG
MAP2
TRIM46 MAP2
day 3
day 5
day 7
day10
day14
day17
day21
50µm
B
TRIM46
ANKG
MAP2
Normalized intensity
distance [µm]
C
TRIM46 enrichment
AIS enrichment factor
****
d3
d5
d7
d10
d14
d17
d21
D
ANKG enrichment
AIS enrichment factor
*
E
MAP2 axonal baseline intensity
normalized intensity
*

**Figure 4.1: TRIM46 and ANKG abundance indicate AIS formation in iPSC-derived neurons within 1.5-2 weeks of differentiation.**

IPSC-derived neurons were differentiated over a time period of 3 weeks and immunostained for TRIM46, ANKG, and MAP2. **(A)** Representative images of neurons of age d3 to d21 labeled with TRIM46, ANKG, and MAP2 antibody. Arrowhead points towards AIS. Note clear boundary between MAP2 and TRIM46 staining after two weeks, but faint and overlapping staining at earlier time points. **(B)** Normalized fluorescence profiles over the first 80 µm of the proximal axon, for TRIM46 (black/green), ANKG (blue) and MAP2 (red). Absolute values of each time point were normalized to the maximum of d17 (=1.0). **(C)** AIS Enrichment Factor for TRIM46. **(D)** AIS Enrichment Factor for ANKG. **(E)** Mean fluorescence intensity of MAP2 60-80 µm distal to the axon hillock. Values were normalized to the maximum of d17 at the proximal axon (=1.0).

**(A-H)** Note increasing abundance and local enrichment of TRIM46 and ANKG at the proximal axon. Progressive neurite outgrowth and branching. Axonal MAP2 abundance declines gradually.

Analysis was performed on 3 experimental replicates with 15-20 neurons each per timepoint. Standard deviation indicated by area fill around line **(B)** or error bars **(C-E).** Statistics: One-way ANOVA with Tukey's multiple comparisons test. Significance levels: *p<0.05, **p<0.01, ***p<0.001, ****p<0.0001.

## 4.2. iPSC-derived neurons and primary mouse neurons express *ANK3* in contrast to SH-SY5Y-derived neurons

Next, we compared the AIS development in three neuronal cell systems: human iPSC-derived neurons, human SH-SY5Y-derived neurons and primary mouse neurons [3]. We used E13.5 primary mouse forebrain neurons at DIV9 as a control model as they showed clear AIS formation in former studies at this time in culture [10,92,209]. We investigated TRIM46 and ANKG abundance using immunocytochemistry (ICC), quantifying fluorescence intensity, localization and local enrichment (AIS EF), as well as mRNA levels via qPCR [3].

Both iPSC-derived neurons and primary mouse neurons displayed a clear TRIM46 and ANKG enrichment along the proximal axon, forming an AIS-like morphology in ICC (Fig. 4.2.$A_{1,3}$). The AIS in both models appeared at a similar position, roughly 5-40 µm from the soma. In both d17 iPSC-derived neurons and DIV9 primary mouse neurons, the proximal enrichment of TRIM46 (iPSC-derived neurons: 7.8-fold, primary mouse neurons: 9.1-fold) and ANKG (iPSC-derived neurons: 7.3-fold, primary mouse neurons: 9.7-fold) was strong (Fig. 4.2.C). Moreover, the maxima of TRIM46 and ANKG signal intensities were located about +/- 10 µm distal to the soma and were separated by the same ~2 µm distance in both models (Fig. 4.2.B: TRIM46 max. at 11.8 µm, ANKG max. at 13.8 µm in iPSC-derived neurons, TRIM46 max. at 10.4 µm, ANKG max. at 12.4 µm in primary mouse neurons) [3].

In contrast, SH-SY5Y-derived neurons showed no detectable ANKG staining (Fig. 4.2.$A_2$, $B_2$). However, TRIM46 was present but at noticeably lower levels compared to iPSC-derived neurons (Fig. 4.2.$A_2$, $B_2$), and its axonal enrichment was modest (AEF = 1.6) relative to the other two neuronal models (Fig. 4.2.C) [3].

To verify the reduced abundance of the AIS proteins in SH-SY5Y derived neurons, we performed qPCR to measure *TRIM46* and *ANK3* mRNA levels in iPSC-derived neurons (d12), differentiated SH-SY5Y-derived neurons (d16), undifferentiated SH-SY5Y cells and HEK-293T cells. The expression was displayed as fold change of the expression in differentiated iPSC-derived neurons, serving as reference. HEK-293T were used as a negative control for qPCR as we did not expect expression of *TRIM46* or *ANK3* in this cell model. *TRIM46* mRNA was detected in SH-SY5Y-derived neurons and rose from 10.7% to 39.9% during differentiation, which was in line with the modest TRIM46 signal seen in ICC. However, consistent with the immunostaining results, *ANK3* expression was absent in both undifferentiated and differentiated SH-SY5Y cells (<1%). HEK-293T cells did not express *TRIM46* or *ANK3*, as expected (Fig. 4.2.D) [3].

Overall, these results show that iPSC-derived neurons have an AIS resembling that of primary mouse forebrain neurons, with expression of both *TRIM46* and *ANK3*. In contrast, SH-SY5Y-derived cells only express *TRIM46* after neuronal differentiation, but lack an ANKG-organized structural component at the proximal axon [3].

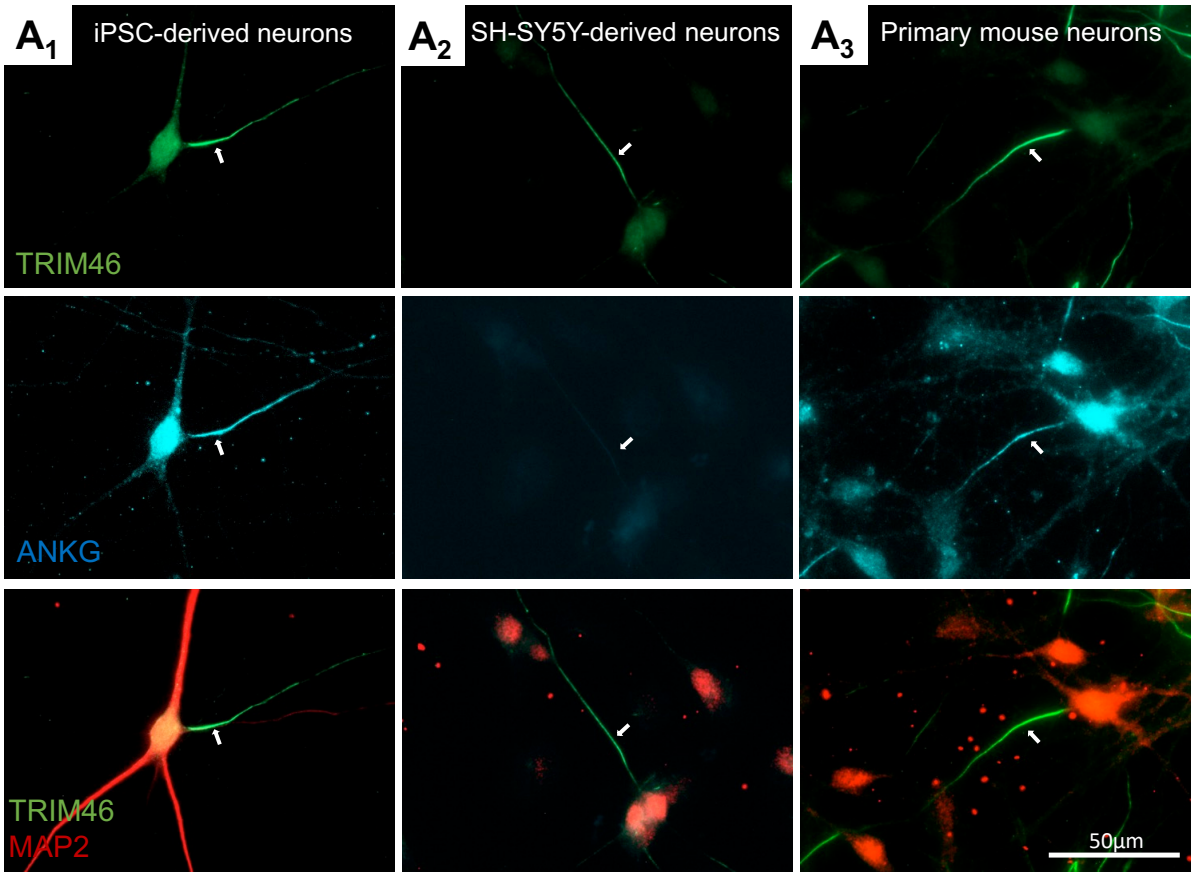
A1
iPSC-derived neurons
A2
SH-SY5Y-derived neurons
A3
Primary mouse neurons
TRIM46
ANKG
TRIM46
MAP2
50µm

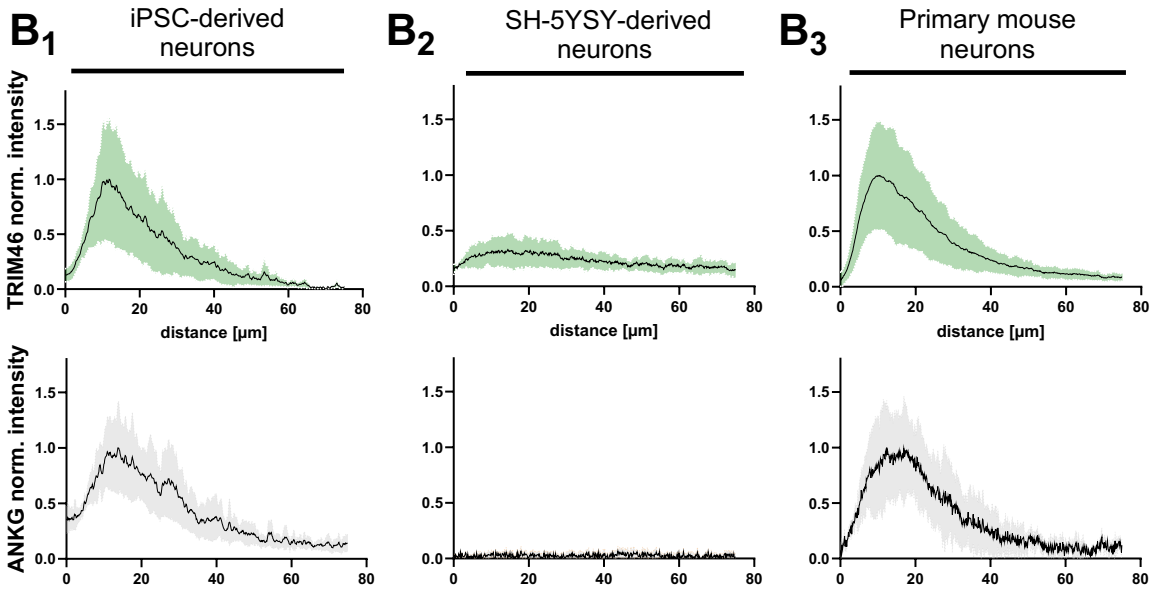
B1
iPSC-derived neurons
B2
SH-5YSY-derived neurons
B3
Primary mouse neurons
TRIM46 norm. intensity
ANKG norm. intensity
distance [µm]

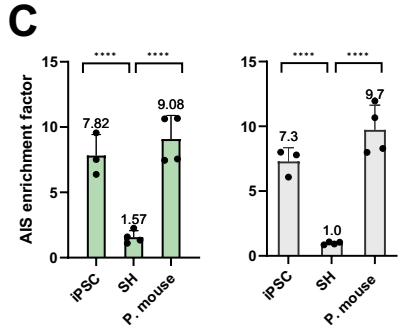
C
AIS enrichment factor
7.82
1.57
9.08
7.3
1.0
9.7
iPSC
SH
P. mouse

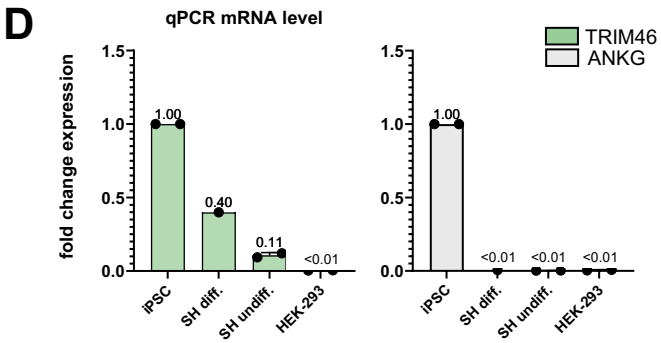
D
qPCR mRNA level
fold change expression
TRIM46
ANKG
1.00
0.40
0.11
<0.01
iPSC
SH diff.
SH undiff.
HEK-293

**Figure 4.2: AIS Development in different neuronal cell systems shows TRIM46+/ANKG+ AIS in iPSC-derived neurons and primary mouse neurons, but absence of ANKG and reduced abundance of TRIM46 in SH-SY5Y-derived neurons.**

**($A_{1-3}$)** Representative images of iPSC-derived neurons at day 17 **($A_1$)**, differentiated SH-SY5Y neurons **($A_2$)**, and primary mouse forebrain neurons at DIV9 **($A_3$)**, stained for TRIM46 (green) and ANKG (blue). iPSC-derived and primary mouse neurons show clear AIS labeling, whereas SH-SY5Y-derived neurons display only moderate TRIM46 and no detectable ANKG signal. (**$B_{1-3}$**) Fluorescence intensity profiles of TRIM46 and ANKG along the proximal axon. Values were normalized to the maximum signal of the iPSC-derived **($B_1$, $B_2$)** or primary mouse neuron **($B_3$)** plots. iPSC-derived and primary neurons exhibit typical AIS enrichment of both proteins, while SH-SY5Y-derived neurons show low TRIM46 levels and almost no ANKG labeling. **(C)** AIS enrichment factors for TRIM46 (green) and ANKG (grey) across the three models. SH-SY5Y-derived neurons show only weak TRIM46 enrichment (~1.6-fold). **(D)** qPCR analysis of *TRIM46* and *ANK3* in iPSC-derived neurons (d12), SH-SY5Y-derived neurons (d16), undifferentiated SH-SY5Y cells and HEK-293T cells. *TRIM46* increases during SH-SY5Y differentiation, whereas *ANK3* remains undetectable [3].

**(B,C)** Analysis was performed on 3-5 experimental replicates with 15-20 neurons each per cell type. Statistics: **(C)** 2-way ANOVA with post-hoc Šídák's multiple comparisons. **(D)** One-way ANOVA with post-hoc Tukey's multiple comparisons. All pairwise comparisons were highly significant (****). Significance levels: *p<0.05, **p<0.01, ***p<0.001, ****p<0.0001. Standard deviation indicated by area fill around line **(B)** or error bars **(C)**. **(D)** Analysis was performed on 1-2 experimental replicates per cell type with 3 technical replicates each.

Data and images for A2, A3, B2, B3, partly C, were obtained from Michael Bell-Simons ([92]), adapted with the author's permission. Preliminary publication of this data in [3].

## 4.3. Neuronal polarity and axonal TAU enrichment

Neuronal polarity is impaired in Alzheimer's disease (AD) and related neurodegenerative tauopathies, as indicated by the aberrant redistribution of TAU from the axons to the somatodendritic region. After we observed differences in the AIS composition between iPSC-derived neurons, SH-SY5Y-derived neurons, and primary mouse neurons, we examined whether this affected their ability to undergo neuronal polarization. We used primary mouse forebrain neurons isolated at E13.5 and cultured to DIV9 as a control model as they show successful TAU sorting at this age [8,92] and have been widely used as an appropriate model in previous TAU studies [8,10,92,115,126,210]. To assess the extent of polarity, we investigated the axodendritic segregation of TAU and MAP2 by immunocytochemistry (ICC) and calculated their compartmental enrichment in the axon as the axonal enrichment factor (AEF) (see 3.2.3.4). Moreover, we evaluated morphological changes such as axonal and dendritic outgrowth, which accompany neuronal polarization and maturation [3].

We observed that all investigated neuronal cell types developed distinct axons and dendrites, forming a dense meshwork of neurites after sufficient maturation, that is >1 week for murine neurons and >2 weeks for human neurons (Fig. 4.3.A, C). Immunolabeling with TAU and MAP2 demonstrated that TAU was distributed throughout the entire neuron but showed strong axonal enrichment, whereas MAP2 was exclusively found in the somatodendritic compartment (Fig. 4.3.A, B) [3].

However, we observed differences between the neuronal models: In iPSC-derived neurons, TAU was already moderately enriched in neurites by day 7 (5.0 ± 3.4), which increased markedly to ~13-fold enrichment by day 21 (13.2 ± 11.5), comparable to levels in primary mouse neurons (14.5 ± 0.7) (Fig. 4.3.B). In SH-SY5Y-derived neurons, TAU was also distinctly enriched in axons (7.9 ± 1.1), although to a lesser extent than in iPSC-derived neurons and primary mouse neurons (Fig. 4.3.B). Notably, SH-SY5Y-derived neurons were the only neurons among the investigated cell types in which axonal MAP2 levels were lower than somatic MAP2 levels (0.6 ± 0.1). However, axonal MAP2 enrichment was also low in iPSC-derived neurons (day 7: 2.1 ± 1.4; day 14: 1.3 ± 0.8; day 21: 3.5 ± 3.0) and primary mouse neurons (1.6 ± 0.3) (Fig. 4.3.B) [3].

We also observed distinct differences in neurite formation across the neuronal models: Early-stage iPSC-derived neurons (day 3) exhibited only 1.2 minor neurites on average. By day 21, they had developed on average 4.7 dendrites and 1.3 axons per cell (Fig. 4.3.C), comparable to neurite formation in primary mouse neurons (5.5 dendrites, 1.2 axons). IPSC-derived neurons frequently developed more than one axon featuring a classic AIS (25% of all neurons), whereas this observation was less common in primary mouse neurons (16%) and very rare in SH-SY5Y-derived neurons (2%) (Fig. 4.3.C, quantification not shown) [3].

We further assessed axon and dendrite diameters at a fixed distance from the soma: while axons of day 21 iPSC-derived neurons showed gradual thinning (average diameter of 0.62 µm) compared to minor neurites on day 3 (0.82 µm), dendrites became thicker (1.17 µm) (Fig. 4.3.C) [3].

In contrast to iPSC-derived neurons and primary mouse neurons, SH-SY5Y-derived neurons developed significantly fewer dendrites (1.8 dendrites), with a smaller diameter (1.05 µm) and reduced branching compared to the other models (Fig. 4.3.C) [3].

In summary, both human neuronal cell types, (AIS-positive) iPSC-derived neurons and (AIS-negative) SH-SY5Y-derived neurons show axodendritic development and marked polarized protein sorting with axonal enrichment of TAU, but not of MAP2, comparable to primary mouse forebrain neurons [3]. Mature iPSC-derived neurons and primary mouse neurons show a higher degree of neuronal polarization, characterized by AIS formation, more extensive dendritic arborization, and enhanced axonal TAU sorting in comparison to SH-SY5Y-derived neurons [3].

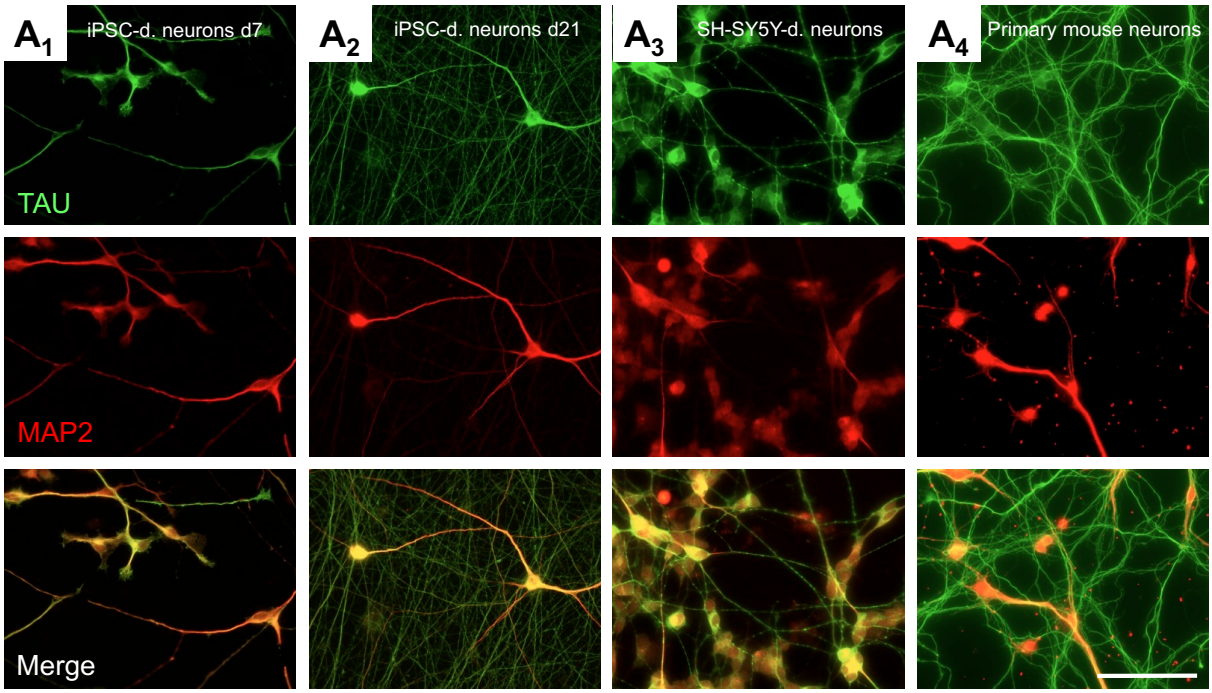

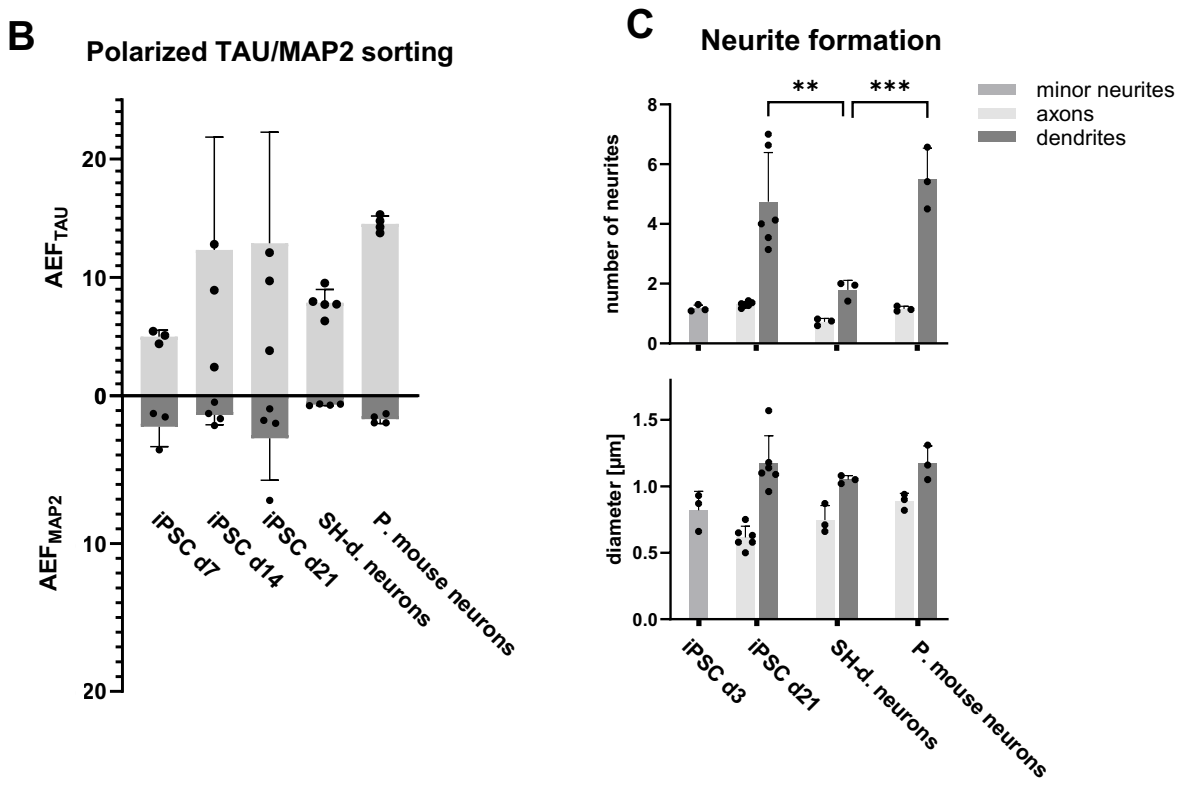


**Figure 4.3: Neuronal polarization occurs in three different neuronal models, with stronger axonal TAU sorting and dendritic development in iPSC-derived neurons and primary mouse neurons compared to SH-SY5Y-derived neurons.**

TAU accumulates in axons, whereas MAP2 is largely excluded from the axonal compartment of iPSC-derived neurons, SH-SY5Y-derived neurons and primary mouse neurons. **($A_{1-4}$)** Representative images of iPSC-derived neurons at 7 days (d7) **($A_1$)** and at 21 days (d21) **($A_2$)** post-differentiation, SH-SY5Y-derived neurons (d14) **($A_3$)** and primary mouse neurons 9 days-in-vitro (DIV9) **($A_4$)**, immunolabeled with TAU (green) and MAP2 (red) antibody. **(B)** Quantification of the axonal enrichment factor (AEF) of TAU and MAP2 in the investigated neuronal cell types. While the MAP2 levels in axon and soma are almost the same, TAU is enriched in the axon in all cell types. Axonal TAU enrichment increases with maturation in iPSC-derived neurons and is also high in primary mouse neurons. In SH-SY5Y derived neurons, TAU is moderately enriched in the axon, whereas axonal MAP2 levels are the lowest. **(C)** Neurite formation in the investigated neuronal cell types. IPSC-derived neurons mostly develop one axon and multiple dendrites, comparable to primary mouse neurons in size and diameter, whereas dendritic formation is reduced in SH-SY5Y cell-derived [3]. Analysis was performed from 3-7 experimental replicates with 12-20 neurons each per cell type and age. Standard deviation indicated by error bars upward for TAU ($AEF_{TAU}$) and downward for MAP2 ($AEF_{MAP2}$). Statistics: **(B)** 2-way ANOVA with post-hoc Šídák's multiple comparisons was not significant ($p>0.01$). **(C)** One-way ANOVA with post-hoc Tukey's multiple comparisons. Significance level: **$p<0.01$, ***$p<0.001$. See methods for detailed calculation of AEF. Scale bar: 50 µm.

Data and images for A3, A4 and B were obtained from Michael Bell-Simons ([92],[211]), adapted with the author's permission. Preliminary publication of this data in [3].

## 4.4. Microtubule organization in iPSC- and SH-SY5Y-derived neurons

MT dysfunction plays a substantial role in numerous neurodegenerative diseases, including tauopathies, but MT organization has rarely been studied in human neuronal models. After observing the absence of an ANKG-organized AIS in SH-SY5Y-derived neurons in contrast to iPSC-derived neurons, we wanted to investigate if this influenced the structure of their MT network. Moreover, we tested if the compartmental enrichment of MAP2 and TAU correlated with differential orientation of MTs in axons and dendrites [3].

To analyze microtubule dynamics and polarity across neuronal compartments and cell models, we transfected iPSC- and SH-SY5Y-derived neurons with a tdTomato-EB3 plasmid (Fig. 4.4.A). EB3 binds to the plus ends of elongating microtubules, and when fused to fluorescent markers such as tdTomato, allows live visualization of MT growth (Fig. 4.4.C) [187]. In time-lapse recordings, EB3 appears as moving comet-like signals of which we generated kymographs displaying the direction, speed, and quantity of MT growth events. EB3 movements were recorded in the proximal and distal axon and in dendrites between days 14 and 18 of differentiation (Fig. 4.4.D).

In both cell types and across all compartments, most MTs were oriented anterogradely, as indicated by EB3 comets traveling from the soma to the periphery. However, subtle differences were observed (Fig. 4.4.E). In iPSC-derived neurons, 89.0% ± 4.1 of comets in the proximal axon and 94.3% ± 1.3 in the distal axon were anterograde, whereas the dendrites displayed a significantly lower proportion of anterograde comets (72.4% ± 3.4), resulting in a high percentage of retrograde comets (27.6% ± 4.7). SH-SY5Y-derived neurons showed a similar pattern: anterograde comets made up 94.9% ± 2.0 in the proximal and 95.8% ± 0.8 in the distal axon, but only 79.8% ± 3.6 in the dendrites. Thus, retrograde comets occured four to five times more often in dendrites (20.2% ± 3.6) compared to axons (proximal: 5.1% ± 2.0, distal: 4.2% ± 0.8) [3].

Next, we determined comet frequency (comets per 30 µm/min) as an indicator of dynamic MTs and general growth activity (Fig. 4.4.F). In iPSC-derived neurons, the highest comet density was observed in dendrites (12.2 ± 5.2), followed by the proximal axon (8.7 ± 2.9), and was lowest in the distal axon (3.7 ± 1.2). SH-SY5Y-derived neurons exhibited a similar distribution (dendrites: 12.0 ± 0.9, proximal axon: 9.6 ± 2.1, distal axon: 6.2 ± 1.5), with comet numbers slightly exceeding those in iPSC-derived neurons in all compartments, although differences were not statistically significant [3].

The average speed of MT polymerization was comparable between the two cell types and compartments, ranging from ~10-14 µm/min (Fig. 4.4.G). Comets moved fastest in dendrites of iPSC-derived neurons (13.9 ± 1.1 µm/min) and in the distal axon of SH-SY5Y-derived neurons (14.1 ± 2.1 µm/min).

Across both cell types, anterograde comets typically showed higher velocities than retrograde comets, with the dendritic compartment of iPSC-derived neurons being the only exception. However, the differences were modest and statistically nonsignificant [3].

In summary, MT organization in SH-SY5Y-derived neurons and iPSC-derived neurons was strikingly alike regarding distribution, dynamics and growth rates. Essentially, MTs were almost uniformly oriented outwards in the axon but showed mixed directionality in dendrites, a phenomenon that reflects MT polarity and was more pronounced in the iPSC-derived neurons than in the SH-SY5Y-derived neurons [3].

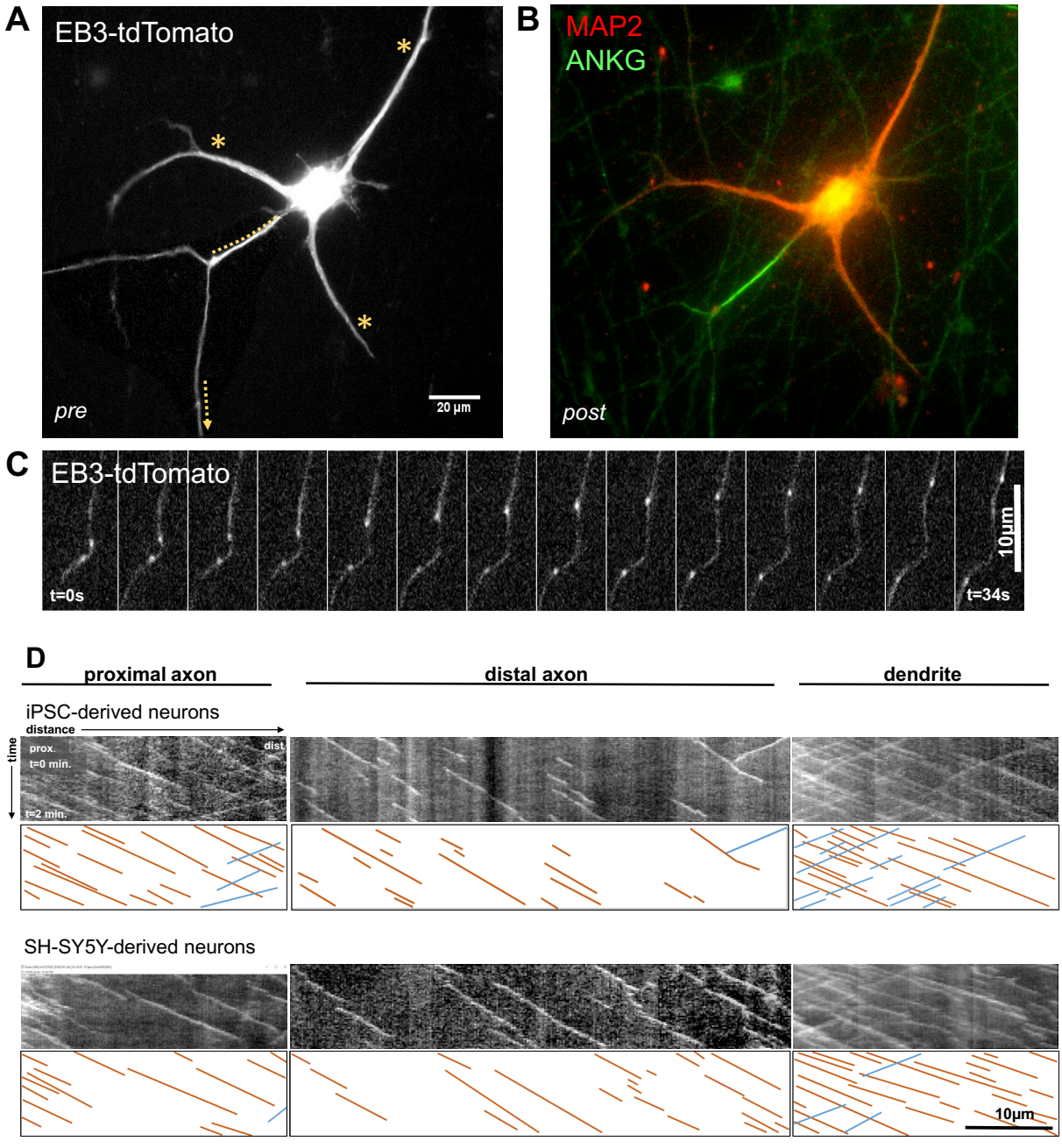

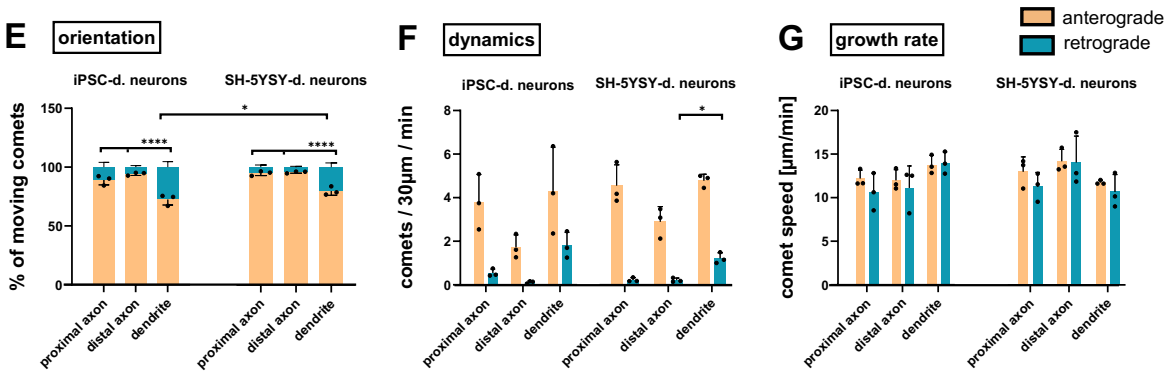


**Figure 4.4: Comparison of MT organization between proximal axon, distal axon and dendrites in iPSC-derived neurons and SH-SY5Y-derived neurons**

**(A)** Exemplary image of an iPSC-derived neuron expressing pEB3-tdTomato. EB3 comet movement was recorded in the proximal axon (dashed line), a dendrite (asterisk) and in the distal axon (not shown; ≥400 µm from the soma). **(B)** After imaging, recorded neurons were fixed and stained for ANKG and MAP2. **(C)** Close-up time-lapse sequence showing two EB3 comets moving in opposite directions within the distal axon of an iPSC-derived neuron (1 frame/2 s). **(D)** Example kymographs from proximal axon, distal axon and dendrite in iPSC-derived and SH-SY5Y-derived neurons. Y-axis indicates time; X-axis indicates traveled distance. Top: raw grayscale kymographs; bottom: illustrative versions with comet trajectories highlighted. **(E)** Quantification of comet direction representing MT orientation. **(F)** Quantification of comet number representing dynamic MTs. **(G)** Quantification of comet velocity representing MT growth rate.

Analysis was performed on 3 experimental replicates per cell type with 18-75 neurons per replicate. Statistics: Two-way ANOVA with Tukey's post hoc correction for multiple comparisons was used to assess significance in **(E-G).** A significant main effect of cell type was detected in **(F).** Significance levels: *$p < 0.05$, **$p < 0.01$, ***$p < 0.001$. In **(E),** error bars for anterograde portions point downward; error bars for retrograde portions point upward. Preliminary publication of this data in [3].

## 4.5. shRNA-based knockdown of *ANK3 and TRIM46*

To study the individual tasks of the AIS proteins ANKG and TRIM46 in initial polarization, axonal MT organization, and TAU sorting, we aimed to perform shRNA-mediated knockdown of *ANK3* and *TRIM46* in iPSC-derived neurons. To achieve this, we pursued two methodological approaches: transient transfection with shRNA-containing pRNAT vector (3.2.1.5) and lentiviral transduction with shRNA-containing pLKO.3G vector (3.2.1.7). Several shRNAs were designed and cloned into the respective plasmid (see 3.2.4.1).

Transfection with shRNA-containing pRNAT resulted in very low transfection efficiency and thus hindered reliable quantification. Therefore, we performed knockdown via lentiviral transduction of pLKO.3G vectors instead, which allowed transduction rates of over 90% (3.2.1.7). Neurons were transduced on day 5 to 7 and fixed on day 17 to 21, bearing in mind the long half-life of AIS proteins, i.e., >1 week for ANKG or >2 weeks for ANKG's primary binding partners NF-186, $Na_v$ channels and βIV-spectrin [59].

We fixed untreated iPSC-derived neurons and those transduced with *ANK3 shRNA*, *TRIM46* shRNA, or non-targeting scrambled shRNA and immunostained for ANKG and/or TRIM46 and MAP2 (Fig. 4.5.1.A, Fig. 4.5.2.A). The fluorescence intensity of the AIS proteins along the first 80 µm of the proximal axon was measured (Fig. 4.5.1.B, Fig. 4.5.2.B) and we analyzed the mean and maximum intensities (Fig. 4.5.1.C-D, Fig. 4.5.2.C-D). Finally, we performed qPCR to assess mRNA levels of *ANK3* and *TRIM46* (Fig. 4.5.1.E, Fig. 4.5.2.E).

### 4.5.1. *ANK3* knockdown

In ICC, the fluorescent profile of the untransduced control neurons reached a higher peak of 221 ± 66 F.I., compared to a maximum of 163 ± 64 F.I. in the neurons transduced with scrambled shRNA and of 119 ± 46 F.I. in those transduced with *ANK3 shRNA*, representing a 1.86-fold difference between control and knockdown cells (Fig. 4.5.1.B, C). The same difference was observed in the mean fluorescence intensity averaged over the total distance of 80 µm, which was 91 ± 18 in control, 71 ± 27 in scrambled shRNA and 40 ± 7 F.I. in *ANK3 shRNA*-treated iPSC-derived neurons (Fig. 4.5.1.D).

To verify the results from ICC, we quantified *ANK3* by qPCR in knockdown iPSC-derived neurons on day 12 of differentiation, transduced with *ANK3* shRNA or scrambled shRNA at day 4. The untransduced neurons served as a reference sample with an expression assigned a value of 1. *ANK3* mRNA levels were reduced in the knockdown sample to 0.51 ± 0.06 relative to the untransduced control. However, the scrambled shRNA had a similar effect on the *ANK3* expression, resulting in mRNA levels of 0.45 ± 0.12 relative to untransduced neurons (Fig. 4.5.1.E).

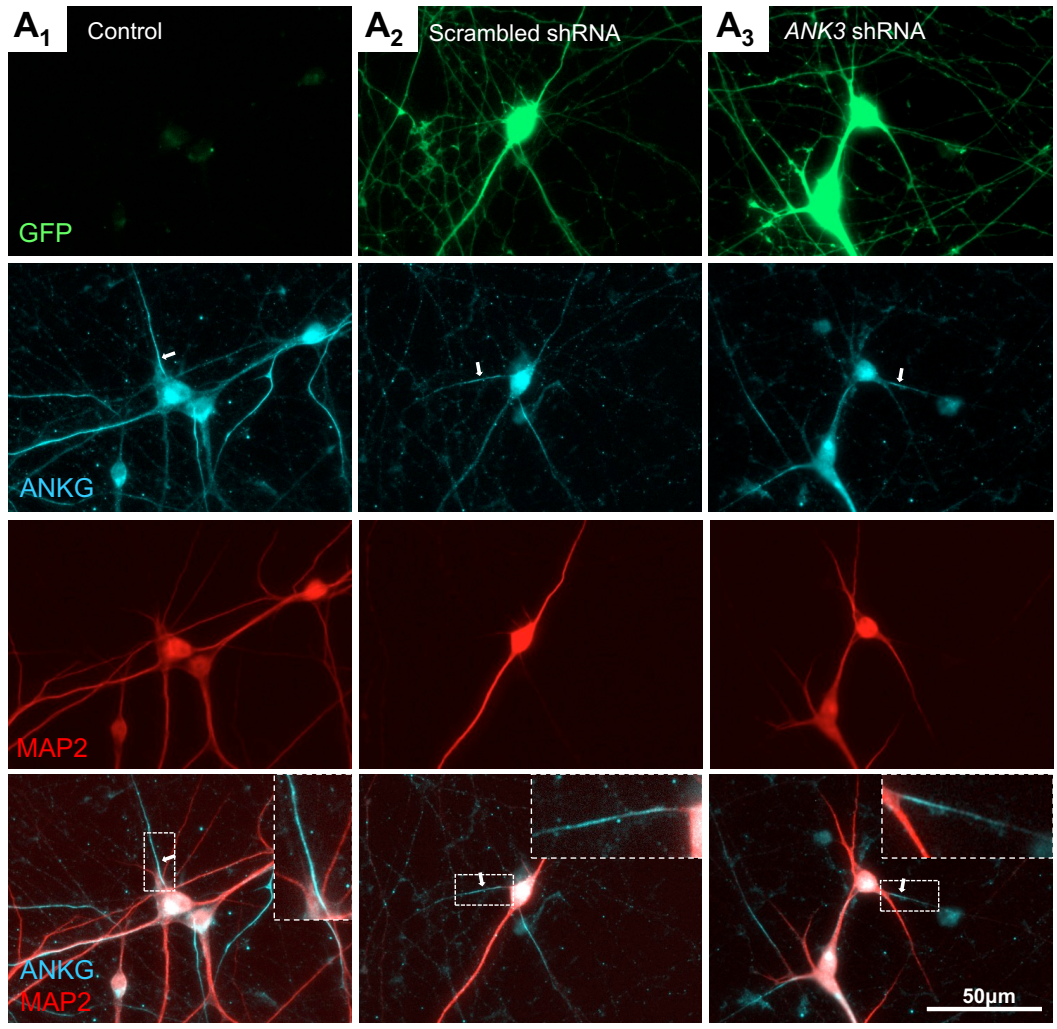
A1
Control
A2
Scrambled shRNA
A3
ANK3 shRNA
GFP
ANKG
MAP2
ANKG
MAP2
50µm

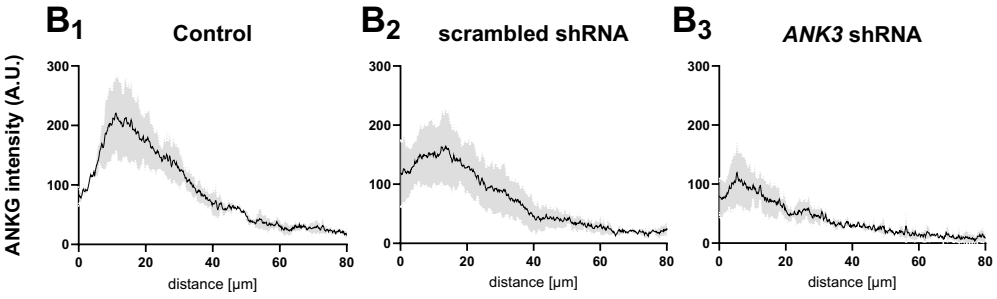
B1
Control
B2
scrambled shRNA
B3
ANK3 shRNA
ANKG intensity (A.U.)
distance [µm]
distance [µm]
distance [µm]

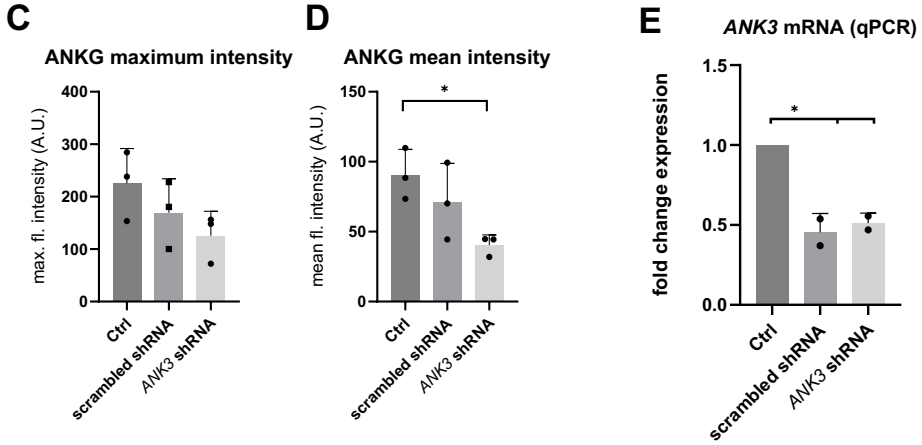
C
ANKG maximum intensity
max. fl. intensity (A.U.)
D
ANKG mean intensity
mean fl. intensity (A.U.)
E
ANK3 mRNA (qPCR)
fold change expression
Ctrl
scrambled shRNA
ANK3 shRNA

**Figure 4.5.1: shRNA-based knockdown via lentiviral transduction of *ANK3* in IPSC-derived neurons**
**(A)** Representative images of iPSC-derived neurons at d21: **($A_1$)** untreated (Control/WT), **($A_2$)** transduced with scrambled shRNA, and **($A_3$)** transduced with *ANK3* shRNA, immunostained for MAP2 and ANKG. **(B)** Fluorescence intensity profile of ANKG at the proximal axon. **(C+D)** Quantification of knockdown results in ICC: **(C)** maximum fluorescent ANKG intensity and **(D)** mean fluorescent ANKG intensity over the first 80 µm of the proximal axon. **(E)** *ANK3* mRNA level in qPCR in WT iPSC-derived neurons, iPSC-derived neurons transduced with scrambled shRNA and *ANK3 shRNA*.
Statistics: A two-way ANOVA and Tukey's correction for multiple comparisons were performed to determine significance in **(C-E)** There was no significant difference in qPCR and ICC between scrambled and targeting shRNA for both proteins. Significance levels: *p<0.05. Standard deviation indicated by area fill around line **(B)** or error bars **(C, D, E). (B)** Analysis was performed on 2-3 biological replicates per condition with 9-15 neurons each. **(E)** Analysis was performed on 2 biological replicates per condition with 3 technical replicates each.

### 4.5.2. *TRIM46* knockdown

Analogous to the ANKG experiments, we assessed TRIM46 abundance in knockdown and control samples by ICC. The peak intensity of the control neurons (640 ± 86 F.I.) exceeded those of the neurons transduced with scrambled shRNA (547 ± 237 F.I.) as well as those transduced with *TRIM46* shRNA 1 *(*476 ± 333 F.I.) (Fig. 4.5.2.B, C*).* Similar to *ANK3 knock*down, the mean fluorescence intensity was highest in the control neurons (221 ± 35 F.I.), followed by the scrambled shRNA samples (207 ± 50 F.I.), and lowest in those transduced with *TRIM46* shRNA 1 (195 ± 118 F.I.), but differences were less pronounced (Fig. 4.5.2.D). However, variability was high and the effects were not statistically significant.
To verify the results, we quantified *TRIM46* mRNA levels by qPCR in knockdown iPSC-derived neurons on day 12 of differentiation, transduced with *TRIM46* shRNA (1/2) or scrambled control at day 4. The untransduced neurons served as a reference sample with an expression assigned a value of 1. We used two different *TRIM46* shRNAs, which reduced *TRIM46* mRNA levels to 0.48 ± 0.14 (shRNA 1), respectively 0.46 ± 0.03 (shRNA 2). Yet again, the mRNA amount in the scrambled control was even lower at 0.42 ± 0.1 relative to untransduced neurons (Fig. 4.5.2.E).

In conclusion, both *ANK3* and *TRIM46* expression was reduced by lentiviral transduction, however equally by scrambled and gene-specific shRNA and therefore no selective knockdown occurred. Notably, the untransduced neurons were harvested from a different biological replicate, therefore the large differences of these mRNA levels might be due to variable state of maturation and cell health in different batches of iPSC-derived neurons.
For alternative explanations (shRNA off-target effects and sequences, lentiviral toxicity, protein turnover) we refer to the discussion (5.2.1).

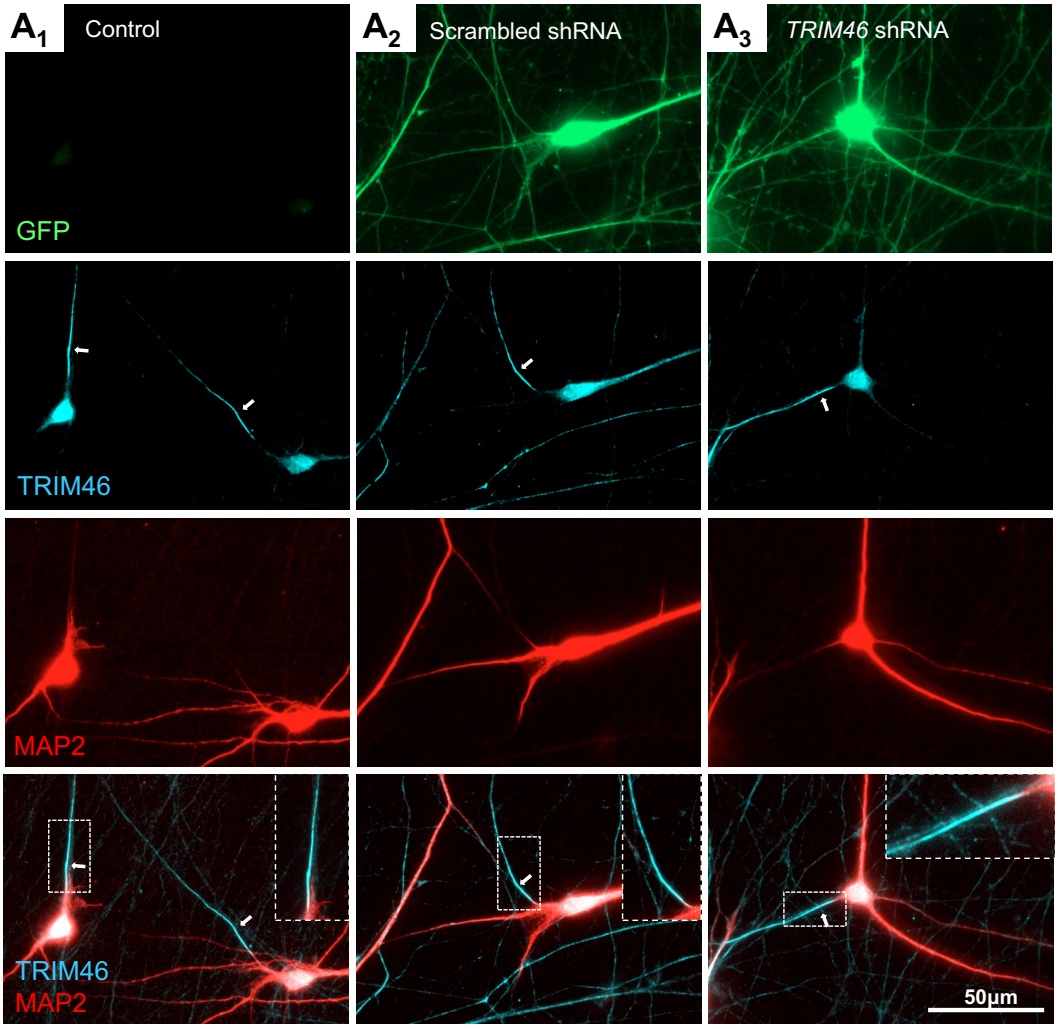
A1
Control
A2
Scrambled shRNA
A3
TRIM46 shRNA
GFP
TRIM46
MAP2
TRIM46
MAP2
50µm

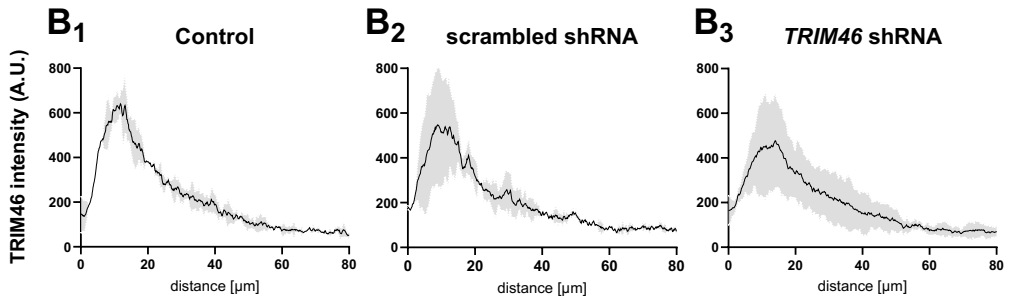
B1
Control
B2
scrambled shRNA
B3
TRIM46 shRNA
TRIM46 intensity (A.U.)
distance [µm]
distance [µm]
distance [µm]

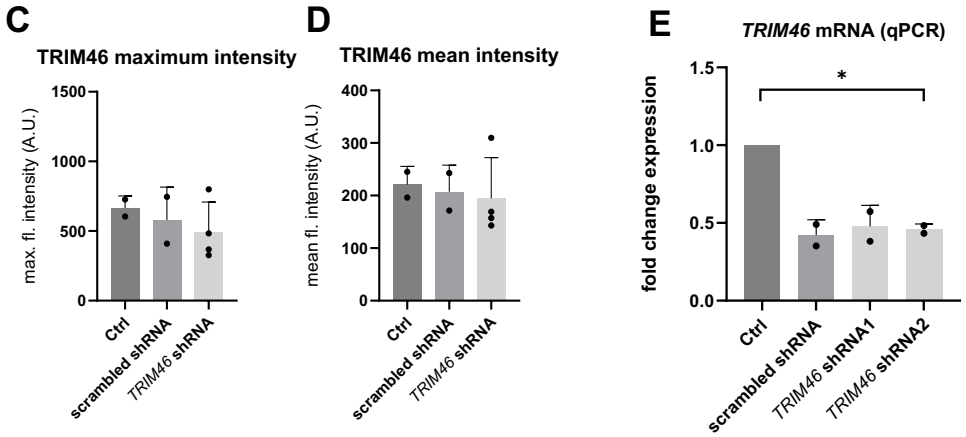
C
TRIM46 maximum intensity
max. fl. intensity (A.U.)
Ctrl
scrambled shRNA
TRIM46 shRNA
D
TRIM46 mean intensity
mean fl. intensity (A.U.)
Ctrl
scrambled shRNA
TRIM46 shRNA
E
TRIM46 mRNA (qPCR)
fold change expression
*
Ctrl
scrambled shRNA
TRIM46 shRNA1
TRIM46 shRNA2

**Figure 4.5.2: shRNA-based knockdown via lentiviral transduction of *TRIM46* in IPSC-derived neurons**

**(A)** Representative images of iPSC-derived neurons at d21 **($A_1$)** untreated (Control/WT), **($A_2$)** transduced with scrambled shRNA and **($A_3$)** *TRIM46* shRNA 1, immunostained for MAP2 and TRIM46. **(B)** Fluorescence intensity profile of TRIM46 at the proximal axon. **(C+D)** Quantification of knockdown results in ICC: **(C)** maximum fluorescent TRIM46 intensity and **(D)** mean fluorescent TRIM46 intensity over the first 80 µm of the proximal axon. **(E)** *TRIM46* mRNA level in qPCR in WT iPSC-derived neurons (d12), iPSC-derived neurons transduced with scrambled shRNA and *TRIM46* shRNA 1 and 2 (d4-d12).

Statistics: A two-way ANOVA and Tukey's correction for multiple comparisons were performed to determine significance in **(C-E)** There was no significant difference in qPCR and ICC between scrambled and targeting shRNA for both proteins. Significance levels: *$p<0.05$. Standard deviation indicated by area fill around line **(B)** or error bars **(C, D, E). (B)** Analysis was performed on 2-3 biological replicates per condition with 9-15 neurons each. **(E)** Analysis was performed on 2 biological replicates per condition with 3 technical replicates each.

# 5. Discussion

TAU pathology plays a pivotal role in the pathogenesis of Alzheimer's Disease (AD) and related tauopathies. To date, no treatments targeting TAU pathology have been approved [212], even though TAU is considered the main driver of disease progression in AD. The somatodendritic missorting of TAU represents an early step in the pathological cascade of these diseases, leading to MT destabilization, transport deficits and synaptic toxicity [2,17,107,110,111]. In order to target TAU missorting, physiological sorting mechanisms that enable axonal TAU enrichment need to be understood. The axon initial segment (AIS) acts as a boundary between the axonal and somatodendritic compartment and was therefore proposed to be involved in axonal TAU sorting [49,59,60]. On the other side, perturbations in the AIS structure are observed in AD animal models and *MAPT*-knockout (KO) *in vitro* models, hinting at a reciprocal relationship between the AIS and TAU [82,83,147]. Furthermore, the study of the neuronal MT network is essential in TAU studies, as it (a) is directly affected by TAU missorting and (b) involved in TAU sorting mechanisms itself [1,55,110,111,213,214]. Current research has addressed both basic neurodevelopment (polarization, AIS development, MAP sorting) as well as TAU pathology mainly in primary rodent cultures or tauopathy mouse models. Due to various limitations in these models, many described mechanisms might differ from those in the human CNS, which is reflected in poor therapeutic success in the field of tauopathies as well as neurological diseases related to MT- and polarity defects [167,168]. Therefore, we here aim to provide a basic characterization of neuronal polarization, AIS development and MT organization in human neuronal models. Specifically, we characterized the temporal AIS development in iPSC-derived neurons and compared AIS composition of human neuronal models (iPSC- and SH-SY5Y-derived neurons) to conventional primary rodent neurons (AIM 1). We investigated whether these differences in the AIS composition influenced neuronal polarization and MAP2/TAU sorting behavior, by implementing a quantitative measure for axonal MAP enrichment (AIM 2). By using +TIP live-cell imaging, we investigated compartmental MT organization in iPSC- and SH-SY5Y-derived neurons (AIM 3). Finally, we discuss if the two established human neuronal models hold promise for extended TAU research (AIM 4).

## 5.1. AIM 1) Investigation of neuronal polarization and AIS development in human neuronal models

To study the interaction between the AIS and TAU in humans, we investigated early polarization in iPSC-derived neurons. To date, most of our knowledge about the structure and assembly of the AIS is based on findings from rats [49,62-64,145], mice [58,59,63,65,66,215,216], or *C.*

*elegans* [84,217] but whether this can be recapitulated in human neurons has only rarely been studied [38]. Importantly, the differentiation of iPSC-derived neurons already provided novel insights into other fundamental processes of neurogenesis in humans among them neurite formation, synapse development or gene expression shifts during development [38,175], demonstrating limited comparability to animal neurons.

Here, we monitored the step-by-step development of the AIS in the early stages of neurodevelopment from induced pluripotent stem cells to (pre)mature human neurons over a timespan of three weeks.

### 5.1.1. **Comparative analysis of neurodevelopmental stages in iPSC-derived neurons and conventional rodent neurons**

The temporal course of AIS development and the establishment of neuronal polarity is well-studied in animal models. Most commonly, dissociated cultures of embryonic (E18) pyramidal rat neurons (hippocampal or cortical) [93] or postnatal cerebellar granule neurons [94,218] are used as model systems in polarity research. Rat hippocampal neurons undergo a well-defined sequence of five developmental stages, initially defined by Banker et al [93] and later expanded to include the formation and maturation of AIS [38,49,61] (Fig. 5.1).

Importantly, alterations in AIS structure (e.g., changes in length and position) as well as cellular TAU polarity are observed both during normal neuronal maturation (4.1, 4.3, [38,67,211]) as well as in response to pathological conditions [10,67,78,79,118,219]. Therefore, when investigating AIS architecture and TAU sorting, it is essential to ensure the comparability of neuronal models, particularly by matching their developmental stages. This includes accounting for differences between *in vivo* and *in vitro* systems, embryonic versus postnatal origin, neuronal types (e.g., cortical pyramidal neurons, hippocampal pyramidal neurons, cerebellar granule neurons), and species (rodent vs. human).

In the following, we illustrate how the developmental trajectory of iPSC-derived neurons aligns with or deviates from these defined maturation stages in rat hippocampal neurons, which represent the standard model for studying neuronal polarity.

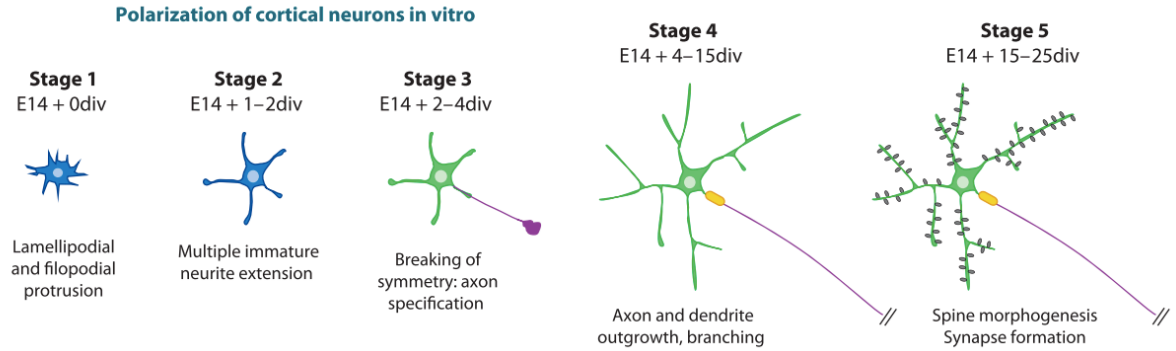


**Figure 5.1: Stages of neuronal development in dissociated cortical rodent neurons.** [91]

Dissociated cortical or hippocampal rat neurons firstly appear as symmetric cells that form small lamellipodia-like processes (stage 1) during the first day in culture (DIV0). These processes grow out to multiple minor neurites (stage 2) of about the same length after one to two days in vitro, of which one neurite experiences extensive outgrowth as the axon while the others elongate only moderately as the dendrites (stage 3), only after 2 to 4 days in vitro [91]. When neurons transition from stage 2 to 3 polarity is established: MTs in the axon become uniformly orientated and TRIM46 localizes to the proximal part of the outgrowing neurite which is about to become the future axon of stage 3 neurons [49]. Between DIV4-7, ANKG becomes detectable, which assembles the remaining AIS components [59,66,69,70], marking the transition to stage 4 neurons. Axo-dendritic compartmentalization is further enhanced in stage 4 neurons (>4 DIV): TAU is enriched in the axon and MAP2 is confined to the dendrites. The following development is defined by further outgrowth of the neurites, dendritic arborization (stage 4, 4-15DIV), and finally synaptogenesis and spine formation (stage 5, >15DIV) [91]. In cortical rodent neurons cultured *in vitro*, axonal TAU enrichment increases during the first two weeks, progressing from accumulation at the distal axon at DIV3 to a clearly polarized distribution by DIV12-16, with slight variations between studies [8,92,126].

Human iPSC-derived neurons broadly followed this developmental course: When plated for differentiation iPSCs appeared as fibroblast-like cells with only small lamellipodia-like protrusions, which corresponds to stage 1 neurons. Already at d3 they grew out one or sometimes multiple short neurites, as representative of stage 2 neurons. Interestingly, stage 2 iPSCs-derived neurons often had only 2 minor neurites of bipolar direction (4.1.,[203]), resembling developing cerebellar granule neurons, whereas rodent neurons at this stage exhibit about 4 to 5 neurites, outgrowing radially from the soma [220].

The abundance of TRIM46 and ANKG in the proximal axon augmented from day 3 to day 10 (stage 2-3), while MAP2 was gradually excluded from the axon. From day 14 on, the AIS proteins had a pronounced proximal enrichment and marked a brisk boundary to the MAP2-defined somatodendritic domain, indicating the transition to stage 4 neurons. At this stage, multiple dendrites grew out, which were of bigger diameter than their counterpart axon that

thinned progressively. In sum, the developmental rate of the human iPSC-derived neurons was much slower: Only after about 1.5 to 2 weeks in culture, they reached stage 4, marked by AIS presence, whereas this occurs in rodent cortical neurons after only 4 to 7 days in culture. Neurogenesis and cortical development is generally faster and less complex in non-human mammals, which may explain the slow differentiation of human iPSC cultures [38].

Finally, we did not investigate whether iPSC-derived neurons acquired properties of stage 5 neurons in this work, as it focused on the AIS and polarized protein sorting.
Former studies working with rapid *NGN2*-differentiation via lentiviral transduction reported abundance of synaptic markers (PSD-95, SNAP25, Synaptobrevin-2, Syntaxin, Synaptotagmin-1) after 3 weeks of differentiation [202]. A recent study from our laboratory showed colocalization of postsynaptic marker PSD-95 and presynaptic marker VGLUT1 in the iPSC-derived neurons used in this study already after two weeks of differentiation [221]. Both Zhang et al. and Wang et al., who work with *NGN2*-differentiation, showed AP firing, spontaneous and evoked postsynaptic currents and thereby the formation of functional synapses after 3, respectively 8 weeks of differentiation. However, they only proved synaptic connectivity in iPSC-derived neurons when co-cultured with mouse glia [186,202]. Still, already 40%, respectively 62% of 2-week-old WTC11 iPSC-derived neurons from our laboratory show spontaneous network activity in calcium signaling experiments when in mono- or co-culture with mouse glia [147]. Thus, iPSC-neurons used in this study presumably need >3 weeks to reach neurodevelopmental stage 5. To verify this, one could combine immunocytochemical detection of synaptic markers (as mentioned above) with high-resolution microscopy using phalloidin, a fungal toxin that binds to F-actin, allowing for more precise structural analysis of dendritic spines and quantification of spine denseness [210]. Moreover, patch-clamp recordings may complement $Ca^{2+}$-imaging to assess synaptic activity on the single-cell level. Finally, RNA sequencing could assess maturity of neuronal populations at the transcriptional level.

### 5.1.2. **AIS development in iPSC-derived neurons: TRIM46 and ANKG abundance and interplay**

In order to use iPSC-derived neurons as a model system to investigate the role of the AIS and polarization defects in neurodegenerative diseases, this study aimed to characterize the basic development of the AIS in iPSC-derived neurons. We monitored the abundance of ANKG and TRIM46 over three weeks in developing iPSC-derived neurons.

Already at day 3-5 of differentiation, immunolabeling for TRIM46 and ANKG was detectable at low intensity, not restricted to the axon but distributed throughout soma and neurites, where it overlapped with MAP2, indicating that axonal specification had not yet occurred. In fact,

transcriptomic profiles of iPSC-derived neurons used in another study showed that *ANK3* and *TRIM46* RNA levels were upregulated only after one week of differentiation (from day 3 to day 7) [38] suggesting early detection could result from nonspecific antibody binding. Future studies using qPCR or Western blot could clarify the actual abundance at these early stages.
The abundance of TRIM46 and ANKG in the proximal axon augmented progressively, and from d10 on, the AIS proteins had a pronounced proximal enrichment and marked a brisk boundary to the MAP2-defined somatodendritic domain. From day 14 onward, the intensity profiles of TRIM46 and ANKG overlapped closely, resembling the AIS composition in primary mouse neurons (4.2.), suggesting a conserved structure across species.
The temporally and spatially overlapping abundance of TRIM46 and ANKG could indicate a direct protein-protein interaction, as ANKG is known to interact with other AIS binding partners [73]. However, the maximum of TRIM46 localized slightly more proximal (~1.8 µm) in the AIS than the one of ANKG, a characteristic that is consistent from day 10 on (4.1.) and also observable in mouse (4.2.) and rat hippocampal neurons [49,74]. Indeed, the super-resolution microscopy technique STORM revealed that TRIM46 decorated a more proximal and central part of the AIS, distinct from the membrane domain marked by ANKG and associated binding partners like βIV-spectrin, NF-186 and $Na_v$ channels [49]. Additionally, biotinylation assays revealed no direct interaction of TRIM46 and known AIS components, except for α2-spectrin (*Sptan1*) and β2-spectrin (*Sptbn1*). Thus, there might be a functional interplay (further discussed in 5.2), reflected by the simultaneous accumulation of ANKG and TRIM46, but no direct protein-to-protein interaction of the two proteins.

Whereas TRIM46 locates only to a single precursor neurite that gives rise to the future axon in hippocampal rat neurons [49], TRIM46 and ANKG were initially present – however, not proximally enriched – in multiple developing neurites in human iPSC derived neurons (4.1, [38]), which may represent a species-dependent difference. Also, we did not find that TRIM46 was present at the AIS earlier than ANKG but that both proteins accumulated simultaneously in iPSC-derived neurons, in contrast to prior studies [38,49]
Moreover, iPSC-derived neurons sometimes developed more than one AIS, a phenomenon observed more frequently than in murine forebrain neurons (4.2). In addition, the AIS occasionally emerged from a basal dendrite, which has also been reported in non-human mammals as well as in human neurons [222,223].

A study characterizing differentiation of human iPSC-derived neurons reported that both AIS proteins were initially present over a longer distance in the developing axon, and only later localized to the proximal part [38], which goes in line with the increase of the axonal enrichment factor and the proximal displacement of the fluorescent peaks from stage 2 to 4 in our

experiments (4.1.). This distal-to-proximal relocation was also found in cultured rat hippocampal neurons [75] or during *in vivo* AIS assembly in mouse motor neurons [216]. Possibly this relocation is involved in axonal MT reorientation [38] or the formation of early spontaneous electrical activity [79].

Strikingly, both the absolute fluorescent values, as well as the axonal enrichment factor decreased for both AIS proteins from day 17 to day 21. It should be noted though that 2 of the 3 replicates investigated at d21 did not originate from the same biological replicate as the replicates from the other time points and therefore differences could be due to the commonly high variability of iPSC batches and thus be a methodological artifact.
If not methodologically explained, AIS protein abundance might indeed reach a peak after 2.5 weeks and then decrease when neuronal polarization is obtained. *NGN2*-induced iPSC-derived neurons showed no expression increase of other neuronal markers, e.g., NeuN and MAP2, from two- to three-week-old neurons [202], so this might equally be the case for the AIS markers. Nevertheless, TRIM46 expression levels augmented progressively even beyond stage 3 in hippocampal rat neurons [48]. Further observation beyond three weeks of differentiation would help to validate this trend.

Summarizing, polarization of iPSC-derived neurons follows broadly the same chronology as primary rodent neurons and their AIS composition seems much alike.
The enrichment of TRIM46 and ANKG in the proximal axon overlaps temporally and spatially and coincides with the axodendritic separation of MAP2 and TAU. However, in contrast to rodent neurons, where TRIM46 precedes ANKG at the AIS and localizes to a single future axon, iPSC-derived neurons show a simultaneous accumulation of both proteins and occasionally form more than one AIS. Moreover, development in iPSC-derived neurons is much slower: polarized stage 4 neurons with ANKG and TRIM46 enrichment at the AIS are obtained after 10-17 days of differentiation. These findings emphasize the necessity of extended differentiation periods for experiments requiring fully polarized neurons. In particular, studies on TAU missorting should be conducted after at least 1.5 to 2.5 weeks of differentiation to ensure the establishment of axodendritic polarity. Furthermore, these results provide a valuable foundation for exploring early neurodevelopment in human neurons and demonstrate their comparability to rodent models in polarity research.

### 5.1.3. **Functional crosstalk between ANKG and TRIM46**

As the master organizer of the AIS, ANKG assembles and maintains the AIS components [59,66,69,70], leading to the speculation that the same might apply to TRIM46. The fact that ANKG and TRIM46 are detectable almost simultaneously in close neighborhood in iPSC-derived

neurons (4.1) and rodent neurons (4.3, [48,49,62,75,92]) suggests a direct interaction between the two partners. Also, we found that in SH-SY5Y-derived neurons, TRIM46 was present but much less confined to the proximal axon in the absence of ANKG. While indeed Freal et al. reported that TRIM46-decorated MT bundles are recruited by ANKG and EB3 to the axonal plasma membrane [74], others showed that TRIM46 localized independently from ANKG to the proximal axon [49,144]. This was demonstrated in former studies where TRIM46 accumulates at the nascent axon to the developing axon before ANKG, with 70% of the neurites in stage 2 neurons being TRIM46+/ANKG- but 0% ANKG+/TRIM46- [3,49]. Moreover, TRIM46 is restricted to the proximal axon of dorsal root ganglion (DRG) neurons, which lack ANKG and other AIS components [224]. The treatment of polarized hippocampal rat neurons (DIV7) with *Ank3 shRNA* over more than a week reduced TRIM46 levels only moderately by 30% [225]. Early *Ank3 knock*down (at DIV1) in hippocampal rat neurons (DIV5) caused moderate mislocalization of TRIM46 distal from its typical localization at the very proximal axon [49]. Similarly, in *Ank3*-knockout mice, TRIM46 decorated a longer segment at the proximal axon than in control neurons [226]. In conclusion, TRIM46 localizes independently from ANKG to the proximal axon, although its precise position at the AIS may be regulated by ANKG.

Nevertheless, alternative mechanisms may contribute to TRIM46's localization at the proximal axon. Probably this role is not assumed by prominent AIS components like βIV-spectrin, NF-186, $Na_v$ as they are also absent in DRG neurons [224] and their knockdown did not result in marked TRIM46 redistribution [49]. Hamdan et al. recently identified additional binding partners of TRIM46 in biotinylation assays, of which the greatest part were no known AIS proteins but AIS tubulins [225]. This study reported interaction of TRIM46 with α2-spectrin and β2-spectrin, which were both recently identified as part of a periodic cytoskeletal scaffold at the AIS [227,228], thereby possibly enriching TRIM46 at the AIS. Alternatively, TRIM46 might be localized to the AIS via anchoring of its associated MT bundles by the -TIP CAMSAP2, which anchors the minus ends of anterograde MTs in the very proximal axon [32]. Additionally, its position could be mediated by MAP2, whose silencing leads to shift of TRIM46 towards the soma [224]. A recent study showed that TRIM46 is transported to the proximal nascent axon by the MT-based kinesin motor complex KIF3A/KAP3, influenced by selective MARK2 phosphorylation [229]. Of note, all experiments mentioned above were conducted in rodent neurons or non-neuronal *in vitro* assays, emphasizing the need to study AIS protein interaction in human neurons.

By which mechanism TRIM46 is clustered at the AIS is crucial question yet to be resolved, as it may define the MT-based boundary for TAU distribution (see 5.2.5, 5.3.4.) and thus be involved in TAU missorting.

### 5.1.4. **Absence of the AIS in SH-SY5Y-derived neurons?**

We found that in SH-SY5Y-derived neurons, *ANK3* was not expressed while *TRIM46* was expressed upon neuronal differentiation but TRIM46 was not precisely restricted to the very proximal axon, as it is the case for ANKG, TRIM46 and other AIS proteins in other cell models. This raises the question whether SH-SY5Y-derived neurons even have an AIS as a structurally defined region. No other study has investigated the presence of known AIS proteins (e.g., βIV-spectrin, NF-186, Ndel1) in SH-SY5Y-derived neurons. Several studies reported AP firing [230,231], but Lazarov et al. demonstrated that APs can arise from other excitable regions of the neuron, even in the absence of a structurally defined AIS, whereas the AIS is required for time precision and wider bandwidth of APs [228]. One study reported genes related to the AIS as significantly enriched among the differentially expressed genes upon differentiation of SH-SY5Y cells, but did not demonstrate localized presence of specific AIS proteins [230]. Finally, it is questionable whether SH-SY5Y-derived neurons show local enrichment of typical AIS proteins, like βIV-spectrin, NF-186 or ion channels, because their anchoring is known to depend on ANKG [59,69,70]. Therefore, SH-SY5Y-derived neurons most likely lack a structurally organized AIS by ANKG, but further studies exploring abundance of other AIS-defining proteins are needed to investigate this matter.

### 5.1.5. **Conclusion: AIM 1**

We monitored ANKG and TRIM46 levels in iPSC-derived neurons and SH-SY5Y-derived neurons in comparison to primary mouse neurons, using ICC, quantitative measures of AIS protein enrichment (AIS EF) and qPCR. The following conclusions can be drawn from these findings: Human iPSC-derived neurons undergo a stepwise process of polarization and AIS development that largely parallels that of primary rodent neurons, however at a slower pace. The abundance of AIS markers, TRIM46 and ANKG was temporally and spatially aligned, resulting in the formation of a structurally distinct AIS from day 10 to 14. These findings confirm the suitability of iPSC-derived neurons for modeling AIS-associated processes, while emphasizing the need for extended differentiation periods, i.e., >14 days, to achieve robust axodendritic polarity (stage 4).

SH-SY5Y-derived neurons, by contrast, lacked ANKG and showed diminished TRIM46 enrichment, limiting their applicability for AIS-focused studies. Overall, these results provide the groundwork for future research on AIS-related TAU (mis)sorting and polarity defects in human neurons, while offering a reference for the timing of such investigations as well as comparability to rodent models.

## 5.2. AIM 2) The role of AIS proteins ANKG and TRIM46 in neuronal polarization and TAU sorting

### 5.2.1. Limitations in shRNA-mediated knockdown of *ANK3* and *TRIM46*

To better understand the functional interplay of ANKG and TRIM46 and their responsibilities in TAU sorting and polarity, we wanted to silence their expression via shRNA-mediated knockdown. Liposomal transfection with all pRNAT plasmids containing different shRNAs resulted in very low transfection efficiency (3.2.1.7) in contrast to empty pRNAT, and thus hindered reliable quantification. One possible reason, could be that shRNA-containing plasmids exceeded a critical size where lipid-based reagents lose efficiency [232]. Moreover, stem cell-derived cells were described as a hard-to-transfect cell type [232], so we pursued shRNA-mediated knockdown via lentiviral transduction. Transduction of iPSC-derived neurons introducing *TRIM46* and *ANK3 shRNA* with different experimental setups yielded high transduction efficiency but did not result in in target-specific knockdown. In qPCR and immunofluorescence experiments, their mRNA and protein amount, respectively, was reduced compared to untreated neurons but similar to those infected with scrambled shRNA.

This could be due to the overwhelming stability and longevity of AIS proteins. In primary neurons, ANKG was depleted only after 2 weeks of shRNA-treatment [59] and the number of neurons with an ANKG-positive AIS was reduced only by 37% after 3 days of transfection. Other AIS proteins have a similarly long half-life, like NF-186, $Na_v$ channels and β-spectrin [59], hence this might be also the case for TRIM46. However, we tried to overcome longevity of AIS proteins by early (starting before AIS implementation at d3-5 of differentiation) and long transduction. Thus, the ineffective knockdown is mostly due to methodological reasons:

Possibly all shRNA constructs had non-specific off-target effects leading to overall mRNA degradation or the mode of delivery – the lentiviral infection using high viral titers and prolonged transduction periods (with viral exposure up to d21) – had a toxic effect on the treated neurons. Notably the untransduced neurons were harvested from a different biological replicate, therefore the substantial differences of these mRNA levels might be due to variable state of maturation and cell health in different batches of iPSC-derived neurons.

Furthermore, it is probable that the designed shRNA sequences were simply not effective or that there was a structural error composing the shRNAs, as none of the three sequences resulted in target silencing. Indeed, we found that the design is possibly flawed as the sequence of insertion included a 2 bp-overhang (TT), that may have disabled shRNA loop formation. However, this would not explain mRNA reduction in the crontol sample (scrambled shRNA).

Thus, to investigate the distinct effects of an *ANK3* or *TRIM46* knockdown, further experiments are needed with adapted shRNA sequences, optimized lentiviral titers, the evaluation of cell viability and assessment of off-target effects in transcriptome analysis.

### 5.2.2. **SH-SY5Y-derived neurons acquire axon formation and polarized TAU sorting without ANKG-organized AIS**

We compared AIS development and polarization in iPSC-derived neurons, primary mouse neurons and SH-SY5Y-derived neurons. While iPSC-derived neurons and primary mouse neurons showed a similar AIS composition, SH-SY5Y-derived neurons lacked *ANK3* expression and showed only moderate levels of TRIM46 (4.2). Importantly, TRIM46 abundance increased during neuronal differentiation (4.1, 4.2), consistent with its described function in early neuronal polarization [49,74]. As discussed (5.1.4.), SH-SY5Y-derived neurons most likely lack a structurally organized AIS by ANKG. All three cell models nevertheless established neuronal polarity, represented by the establishment of separate axonal and dendritic domains with compartment-specific localization of TAU and MAP2 (4.3).

This was unexpected, as earlier studies reported that ANKG was essential for maintenance of neuronal polarity and axonal identity [59-61]. Yet, SH-SY5Y-derived neurons generated axons and displayed polarized protein sorting without ANKG.

However, several studies have questioned whether ANKG alone controls axonal identity [49,63,75,92,214,233,234], which is supported by our findings.

Instead we propose to differentiate between distinct tasks of ANKG and TRIM46 in (1) initiation of neuronal polarity (Chapter 5.2.3.), (2) axon formation (Chapter 5.2.3.), (3) TAU sorting (Chapter 5.2.4, 5.2.5.) and (4) maintenance of neural polarity (5.2.6).

### 5.2.3. **TRIM46 mediates initial polarization and axon formation**

In both iPSC- and SH-SY5Y-derived neurons, TRIM46 levels increase progressively during early development (4.1, 4.2, [38]). In iPSC-derived neurons, TRIM46 levels reach a high plateau after 1.5 weeks of differentiation, which corresponds to stage 3-4 of neuronal development. (4.1) Simultaneously, extensive axonal outgrowth occurs in both cell models. (4.3) Former research findings explain the causal link between TRIM46 abundance and structural polarization:

Cytoskeletal rearrangements in the neurite destined to the axon are needed for axonal outgrowth: Numerous MTs must grow extensively towards the periphery and they must be of particular stability. Witte et al. demonstrated this by applying the MT-stabilizing drug taxol to unpolarized neurons which led to the development of multiple minor neurites into axons. When exposing a photo-activatable form of taxol to a single neurite, axonal outgrowth was only

observed in this specific neurite [43]. Indeed, previous studies have shown that this stabilization can be achieved by TRIM46. TRIM46 localizes to the future axon [49] and cross-links parallel MTs in bundles [48] which experience – when bundled – a higher rescue frequency [74]. This means that they are less susceptible to depolymerization, which in turn promotes their growth. Moreover, MTs bundled by TRIM46 are uniformly oriented into the same direction (See 2.3.2, [48]) a phenomenon that is also observable in non-neuronal cell types when TRIM46 is introduced [49,74].

Finally, the joint growth of the parallel TRIM46-stabilized MTs towards the growth cone drives the elongation of the nascent axon into the periphery. TRIM46's role in MT fasciculation and stabilization is supported by results from knockdown experiments: uniform MT orientation is lost in the axon and a dendrite-like bidirectional orientation emerges (30% of MTs with minus-end out). Axonal outgrowth is reduced and even taxol-induced axon formation is blocked in TRIM46-deficient neurites [49].

Conclusively, TRIM46 could mediate initial axon formation via its MT-associated function.

Of note, a recent study contradicted former findings about TRIM46's function: While Van Beuningen et al. found that TRIM46 is crucial for axon specification by shRNA-mediated knockdown of *TRIM46* in cultured neurons and in neonatal mice after in utero shRNA electroporation, Melton et al. showed normal axon formation and brain structure in *TRIM46*-knockout mice [226]. To explain these discrepant findings, the authors suggest that sudden TRIM46 depletion by shRNA during axon specification may cause more severe effects, while a permanent absence of TRIM46 in knockout mice may allow compensation by yet unidentified proteins in axon formation. Future studies should identify those regulators of axon formation that compensate for loss of TRIM46.

Importantly, the extensive elongation of the axon could be a key factor driving polarization itself. Lamoureux et al. showed that forced extension of a minor neurite via mechanical stretching caused this neurite to acquire additional axonal properties [235]. The mechanistic explanation of this could be that the axonal outgrowth per se modulates molecular feedback loops of polarity factors, that in turn drive downstream signaling establishing the axonal fate and further polarization [236]. These may be the mechanisms by which TRIM46 initiates neuronal polarity.

### 5.2.4. **Differential tasks of ANKG and TRIM46 in TAU sorting and neuronal polarity**

We investigated compartmental TAU and MAP2 sorting in iPSC-derived neurons, SH-SY5Y-derived neurons and primary mouse neurons. Primary mouse neurons isolated at E13.5 and cultured to DIV9 served as a control model for successful TAU sorting, as they are known to be polarized by DIV2-4 and to accumulate axonal TAU beginning at DIV3, with increasing

enrichment up to approximately DIV12-16. [8,92,126]. These neurons have been widely used as a reliable model in previous TAU studies [8,10,92,115,126,210]. We chose not to work with more mature primary neurons (>DIV10), which already undergo spine formation and synaptogenesis, to match the approximate developmental stage of iPSC- and SH-SY5Y-derived neurons at 14 days of differentiation.

After characterizing the time course of AIS development in iPSC-derived neurons, we aimed to determine whether it correlated with MAP2 and TAU sorting. Therefore, we examined iPSC-derived neurons at different developmental stages: after one week (stage 2-3), two weeks (stage 3-4), and three weeks (stage 4).

Parallel to the AIS assembly, the iPSC-derived neurons of two and three weeks of age showed axodendritic segregation of MAP2 and TAU. Strikingly, TAU was enriched, in contrast to MAP2, already in the emerging neurites of stage 2-3 iPSC-derived neurons (d3-d10) before the AIS was fully implemented, suggesting that its polarized sorting might be independent of the AIS. Instead, it could be mediated by polarized transport, that is established before the assembly of the AIS [63]. In addition, ANKG-deficient SH-SY5Y-derived neurons also showed a high extent of axonal TAU enrichment. This was in contradiction with former studies that reported the redistribution of TAU and MAP2 in *Ank3*-KD neurons [59-61].

So how can we explain the polarized protein sorting, of predominantly TAU, despite ANKG deficiency? Should ANKG's role be reconsidered? Strikingly, the knockdown of *Trim46* also led to redistribution of MAP2 and TAU [49,75].

Regarding the involvement of both AIS proteins in polarized protein sorting we have to differentiate between cytosolic proteins, segregation of membrane-bound proteins and polarized active transport. Below, we will discuss the AIS's role in these modalities of TAU movement.

### 5.2.5. **Microtubule-dependent distribution of TAU**

As a cytosolic protein, TAU can be sorted into the axon through three primary mechanisms: (a) diffusion of soluble TAU in the cytosol, (b) MT-bound movement along the microtubule lattice, and (c) active motor-driven transport. TRIM46 promotes axon-specific bundling and anterograde orientation of MTs, which could serve as a structural platform for both passive diffusion and active transport of TAU into the axon.

#### Passive TAU distribution by diffusion

Earlier models proposed that ANKG and its associated actin filaments at the AIS function as a size-dependent diffusion barrier, preventing axosomatic diffusion of proteins like TAU and MAP2 [82,145]. However, super-resolution microscopy has revealed no such physical filter [62]. Furthermore, Hirokawa et al. demonstrated that microinjected TAU initially distributed

throughout the soma and dendrites but ultimately persisted only in the axon [140], challenging the notion that the AIS maintains polarized distribution of soluble proteins like TAU by acting as a physical barrier.

Alternatively, diffusion-driven sorting of TAU into the axon could be mediated by a preferential affinity of TAU for axonal MTs. This interaction is in a dynamic equilibrium, where TAU periodically binds and detaches from the MTs [4]: If TAU binds too tightly to MTs (e.g., due to low phosphorylation or certain isoforms), it may become immobilized and fail to reach distal axonal regions. If TAU's MT affinity is too low (e.g., due to hyperphosphorylation), it may detach from MTs and mislocalize, including to dendrites and soma, as seen in disease states [143]. It was also proposed that the binding of free TAU to MTs in the AIS creates a negative gradient of free TAU from the soma to the AIS, which leads to diffusion-driven transport of TAU into the proximal axon [198]. In addition to diffusion of soluble TAU, MT-bound TAU can move along the MT lattice itself [196].

As the axon elongates during development, this could constantly supply free MT binding sites for TAU and thereby create a concentration gradient.

However, the fact that axonal TAU localization is mediated by diffusivity and MT affinity was challenged in recent studies: Iwata et al. showed that a TAU variant lacking the MT-binding domain still localized to the axon, while a TAU variant with reduced diffusivity and increased MT affinity (dephosphorylation-mimetic mutations in the proline-rich region) was mislocalized to the soma and dendrites [126]. Bell et al. selectively expressed various *MAPT* variants in human *MAPT*-KO iPSC-derived neurons and found that axonal sorting was independent from general MT affinity of the corresponding TAU variant [211].

**Active transport mechanisms of TAU**

Moreover, active transport mechanisms via motors on the MT track were reported to be essential for axonal TAU enrichment, especially in the long-distance range [197]. As a cytoplasmic protein, TAU is not a classic cargo of fast motor-driven transport, but moves at rates of 0.2-0.4 mm per day [200,237]. It can be transported solely via motor-driven slow transport [200], as well as co-transported in a "piggyback" mechanism along with short MT-fragments via fast-transport [197]. Directed active transport is determined by the differential interaction of the cargo with an appropriate motor, e.g., synaptic vesicles on kinesin motors or postsynaptic receptors on dynein motors [144,217,238]. Utton et al. demonstrated that TAU directly interacts with kinesin-1 via kinesin light chains 1 and 2 but not dynein, implying a preference for anterograde transport [199]. Indeed, FRAP experiments showed that anterograde movement of TAU in the axon outweighs retrograde movement [126]. Moreover, photoconvertible forms of TAU (TAU coupled to Dendra2) showed axon-biased movement of TAU after photoconversion in the soma [126]. Impaired interaction of TAU and kinesin light chains also leads to TAU

hyperphosphorylation, accumulation and neurodegeneration [239,240]. On the other hand, filamentous TAU disrupts kinesin-driven transport via activation of PP1 and GSK-3 kinases [241]. Accordingly, impaired TAU-motor interactions may trigger TAU missorting through a positive feedback mechanism.

Importantly, studies have shown that polarized cargo transport occurs in young neurons before AIS assembly [214,233] and even in *Ank3*-knockdown neurons [63,144]. These findings strongly suggest that axonal TAU enrichment is independent of ANKG, which could explain why SH-SY5Y-derived neurons can accumulate TAU in the axon.

Notably, motor-driven TAU sorting depends on the correct MT orientation, since kinesin moves exclusively towards plus-ends. This organization is controlled by TRIM46, which ensures uniform MT polarity in the axon [48,49] and was present in SH-SY5Y-, as well as iPSC-derived neurons (4.4).

Consistently, TRIM46 was shown to localize at the "pre-axonal exclusion zone", a proximal compartment where sorting decisions occur [144,224]. Moreover, Gumy et al. demonstrated TRIM46's involvement in this exclusion process in sensory DRG neurons which lack a classical AIS, like SH-SY5Y-derived neurons [224]. They propose that cargo sorting is mediated by MAP2, whose positioning depends on TRIM46. These mechanisms could explain axodendritic sorting of TAU and MAP2 by means of active transport, dependent on the TRIM46-controlled MT array but independent from ANKG.

### 5.2.6. **The AIS barrier for membrane proteins**

Neuronal polarization is not limited to the differential distribution of TAU and MAP2, but also includes the axosomatic segregation of numerous other cytosolic proteins as well as membrane-bound proteins, e.g., pre- and postsynaptic receptors or ion channels, that define the axonal or dendritic identity.

We did not investigate the distribution of these compartment-specific proteins in SH-SY5Y-derived neurons, so we can only speculate about ANKG's role in their distribution, but previous studies provide an outlook: It has been shown that the lateral diffusion of membrane proteins and the mobility of lipids at the AIS is restricted. A so-called "picket and fences" model was proposed in which ANKG organizes its associated membrane proteins (pickets) and the underlying actin skeleton (fences), so that membrane proteins would not redistribute between the somatodendritic and axonal domain [146,242]. This may explain, why the postsynaptic membrane protein PSD-95 is detectable in axons of *Ank3*-knockdown neurons after 1.5 weeks [59].

Conclusively, active cargo transport may be independent from ANKG, but ANKG prevents the retrograde diffusion and intermixing of axonal and somatodendritic membrane proteins. Finally,

this explains how polarized distribution of membrane proteins or those associated with them is maintained – not established – in the long term by ANKG.

### 5.2.7. **Conclusion: AIM 2**

We aimed to identify the role of TRIM46 and ANKG in neuronal polarization and TAU sorting. While shRNA-mediated knockdown was limited by methodological constraints, comparative analyses between iPSC-derived neurons and SH-SY5Y-derived neurons revealed that axon formation and polarized TAU distribution can occur independently of ANKG. Based on previous studies, we argue that TRIM46 provides the architectural foundation for initial polarization by enabling axonal outgrowth via its MT-organizing function. Through anterograde MT bundling, TRIM46 also provides the basis for directed active protein sorting. Axonal TAU enrichment was observed prior to full AIS assembly and even in ANKG-deficient SH-SY5Y-derived neurons. Thus, axonal TAU sorting may result from anterogradely-biased active transport, rather than a direct diffusional barrier at the AIS. This could explain how TRIM46 as a predominant organizer of axonal MTs may be sufficient to drive axonal TAU enrichment, in the absence of ANKG.

However, as neurons mature, ANKG becomes essential in maintaining polarity by preserving the axo-dendritic separation of membrane proteins and the integrity of the AIS. This might indeed be needed to acquire advanced functions of higher neuronal maturity, including e.g., AP firing, development of synaptic connections, lowering of the membrane potential or distinct neurite branching.

Summarizing the distinct roles of the two AIS proteins: the TRIM46-MT-interaction may drive initial polarization (1), enabling axon formation (2) and axonal TAU sorting (3), while an ANKG-organized AIS is needed to acquire neuronal functions associated with maturity and to maintain long-term polarity in mature neurons (4).

## 5.3. AIM 3) Characterization of compartmental MT organization in human neuronal models

Neuronal microtubules are essential for neuronal polarity, migration, and differentiation [22]. Axons and dendrites exhibit a distinct MT organization, which dictates intracellular transport, neuronal signaling, and overall cell morphology. Axonal MTs are highly polarized with uniform plus-end-out orientation, whereas dendritic MTs display mixed polarity [22,35]. Understanding the mechanisms governing this MT polarization is critical for deciphering how neurons develop and maintain their functional architecture. Furthermore, insights into MT dynamics in human neurons are essential for understanding cytoskeletal dysfunction in neurodevelopmental disorders and neurodegenerative diseases.

In this study, we investigated MT dynamics in SH-SY5Y- and iPSC-derived neurons using +TIP live imaging to address key questions related to neuronal polarity. Specifically, we examined (1) whether MT reorientation occurred in both cell models, confirming their identity as polarized neurons, (2) the role of the AIS and associated proteins (TRIM46 and ANKG) in shaping MT organization, (3) the contribution of MT polarity to axonal TAU sorting, and (4) if there are species-dependent differences in MT growth parameters. Understanding MT behavior in human neurons is particularly relevant for identifying differences in cytoskeletal regulation compared to other model organisms, as these may affect the translatability of studies on neuronal development and pathologic conditions related to cytoskeletal dysfunction.

### 5.3.1. **Microtubule polarity in iPSC- and SH-SY5Y-derived neurons**

In both iPSC- and SH-SY5Y-derived neurons, we observed highly polarized MTs in the axonal compartment with ~90-95% of their plus-ends growing towards the periphery, compared to 79%, respectively 72% in dendrites, representing a typical feature of MTs in polarized neurons [22,35].

Notably, former studies have demonstrated MT-reorganization during neuronal polarization: MTs in minor neurites of unpolarized neurons (stage 2) are of mixed polarity (80 plus-end out, 20% plus-end in), but during initial polarization (stage 3), the MTs in the neurite destined for the future axon, are reorganized to the typical uniform anterograde orientation [31,33,39]. In rodent neurons, the proportion of anterograde MTs in the nascent axon is high (>95%) and increases further during development (close to 100%). Contrarily, the number of plus-end out MTs in the minor neurites – later dendrites – decreases from approximately 80 to 60% [3,31,39]. Consistently, studies showed that the number of retrograde MTs in the dendrites increases with length of dendrite [33]. One recent study addressing MT dynamics in iPSC-derived neurons showed a similar pattern in human neurons: in unpolarized stage 2 neurons anterograde MTs made up 80%, increasing to roughly 90% in stage 3 axons, while the proportion of anterograde MTs in dendrites decreased from 80% to 60% [3,38]. Therefore, the greater proportion of retrograde MTs in dendrites of iPSC-derived neurons compared to SH-SY5Y-derived neurons could reflect a more advanced neuronal maturation, consistent with differences in structural polarization between the two neuronal models. Still, both iPSC- and SH-SY5Y-derived neurons have a polarized MT network [3].

### 5.3.2. **Role of ANKG and TRIM46 in establishment of microtubule polarity**

SH-SY5Y-derived neurons develop a polarized MT network, which demonstrates that MT polarization occurs independent of ANKG, which is absent in these neurons. A synthesis from recent studies explains, which factors may account instead for this process:

Both the reorientation and stabilization of MTs in this axonal neurite seems to be required for its extensive outgrowth – thus development into the axon (see 5.3.3). Importantly, studies showed that this is particularly achieved by TRIM46 [49,74]. As explained, TRIM46 localizes to the future axon and cross-links parallel MTs in bundles, of which the joint growth drives the elongation of the nascent axon into the periphery. *Trim46* knockdown leads to bidirectional orientation of axonal MTs (30% minus-end out) and reduction of axonal outgrowth [49]. The fact that MT reorientation during transition of stage 2 to 3 is initiated before the AIS assembles [49], underlines that ANKG is not required for this process.

Finally, we can discuss that TRIM46 is not the only factor determining uniform MT orientation. For example, the -TIP protein CAMSAP2, located at the AIS, is required to stabilize the minus ends from which axonal MTs extend. Besides this, other members of the “parallel bundler” family were proposed, such as TAU isoforms themselves or kinesin-14 [22]. Furthermore, we can speculate that the elimination of minus-end-out oriented MTs from axons, e.g., by retrograde removal of those MTs by dynein motors or through direct severing, leaves only plus-end-out MTs (mechanisms reviewed by [22]). A recent study proposed that dynein works in concert with TRIM46 to sort axonal MTs according to their polarity [243].

### 5.3.3. **Contribution of microtubule polarity to axon formation**

Furthermore, the specific mechanisms by which stable and unidirectional MTs in the AIS promote axonal outgrowth and specification remain unknown. It is thought, that besides polymerization and elongation of the axonal MT bundle, the translocation of the bundle per se might contribute to the extension of the growth cone. In line with this, *Trim46* knockdown led to antiparallel MT orientation not only in the proximal, but also in the distal axon [49]. Therefore, uniform MT bundles, generated by TRIM46, might be shifted towards the distal axon where they contribute to the growth cone extension. Furthermore, axon formation induced by taxol did not only stabilize local MTs but also induced transportation of new MTs to the distal bundle [21]. We can also hypothesize that stable MTs in the proximal axon serve as a de novo nucleation site for new MTs that elongate the axon, using the augmin mechanism described by Sanchez-Huertas et al. [34].

Moreover, the interaction of the MT network with actin filaments, in which actin arcs condense sparse MT to closer bundles at the growth cone, promotes the elongation of peripheral MTs and, consequently, axon extension [21]. Consistently, we observed even more anterograde MTs

in the distal than the proximal axon of both SH-SY5Y- and iPSC-derived neurons, which may reflect the ongoing elongation of the growth cone. Mechanisms of MT orientation could behave analogously to MT stabilization: Although MT stabilization is highest in the axonal shaft and distal axon, the proximal axon/AIS is the primary site of stabilization [47]. Alternatively, retrograde MTs in the proximal axon might be a relic from its previous state as a minor neurite, that could be in the process of retrograde removal, severing or those not yet bundled by TRIM46. Furthermore, the uniform orientation of MTs towards the periphery plus the preferential binding of motors – specifically kinesin subtypes – drives the transport of MT-fragments, tubulin heterodimers, as well as organelles, transcription factors or proteins to the distal axon which in turn enforce axon extension and specification [21]. For example, it was suggested that proteasomes are transported retrogradely along the axon which establishes an asymmetric protein composition through local proteostasis [244].

In sum anterograde orientation of axonal MTs, as we observed in iPSC- and SH-SY5Y-derived neurons, is a unique feature of polarized neurons and represents a prerequisite for axonal outgrowth and specification.

### 5.3.4. **Contribution of microtubule polarity to polarized protein sorting and TAU distribution**

We proposed that efficient TAU targeting to the axon depends on a uniform microtubule orientation. Supporting this, polarized protein distribution aligned with MT directionality in both iPSC- and SH-SY5Y-derived neurons: MAP2 was enriched where MT polarity was mixed, while TAU accumulated in regions with predominantly plus-end-out MT arrays [3]. This goes in line with previous observations that TAU remains broadly distributed in immature stage-2 iPSC-derived neurons (4.3, [211]), which still show MT networks of mixed polarity in their outgrowing neurites [3,38]. As discussed in 5.4., we propose that axonal MT orientation promotes kinesin-driven anterograde transport of TAU [199]. In addition, AIS-specific MT properties, including polarity, spacing, PTMs, local binding partners, may enhance TAU binding, which could further promote a diffusional TAU gradient from the soma to the axon, as proposed before [3,198]. Conversely, MAP2 may not associate with axonal motor proteins, as it was shown for other dendritic cargo [144]. Conclusively, we propose that axodendritic MT polarity establishes polarized protein sorting by selective engagement of motors [3,144].

### 5.3.5. **The organization of the MT network is species-dependent**

Finally, we can compare the parameters of MT dynamics in these human cell models to those from animal models. Plus-end dynamics have been studied in various species and cell types, including rat and mouse neurons, neurons from *Drosophila*, *C. elegans,* and recently also

iPSC-derived neurons [31,33,37,38,42,49,245-247]. Moreover, MT dynamics were studies in different neuronal subtypes – hippocampal neurons, Purkinje cells or glia – and by the use of different +TIP proteins – EB1, EB3, CLIP-115 and CLIP-170 [42]. Finally, Yau et al. even compared differences of MT dynamics in several experimental setups: *in vitro, in vivo* and *ex vivo* [31].
These versatile experiments showed significant differences in the parameters of MT dynamics depending on the species, neuronal subtype, developmental stage or presence of pathological influences.
The uniform orientation of anterograde in MTs, compared to bidirectional MTs in dendrites, seems to be a conserved feature of neurons in various animal models, however the degree of this polarization differs between species. In invertebrates, such as *Drosophila* [33] and *C. elegans* [246], axonal and dendritic MTs are of completely opposite polarity, hence ~100% directed away, respectively towards the soma. However, rodent neuron types – pyramidal neurons from hippocampus [31,42,49] or somatosensory cortex [31,37], dentate granule cells [31], Purkinje neurons [42], motor neurons [37] – conserve anterograde MTs in the axon (~100%), but only ~40% of MTs in the dendrites are directed retrogradely.
Here, we demonstrate that in human neurons the feature of anterograde MT orientation in the axon is conserved, but that retrograde orientation in dendrites is less pronounced (~20-30%). One could explain that this discrepancy by a lower maturity of the human neuronal cultures which were imaged at 2.5 weeks of age, in contrast to former findings from hippocampal rat neurons at the age of more than 2 months or from mature hippocampal slice cultures [31]. However, our findings are consistent with a recent study characterizing MT dynamics in iPSC-derived neurons at the age of ~2 weeks [38] and ~3 weeks [245] and, therefore these specific proportions could be unique to human neurons.

Finally, methodological differences must be considered when comparing MT orientation across different studies. Notably, +TIP imaging in non-manipulated neurons only visualizes growth events, thus orientation of dynamic MTs. To unravel orientation of stable non-polymerizing MTs, laser severing of MTs is necessary [31]. After cutting, they will polymerize following their orientation. Importantly, a considerable portion of MTs, especially in dendrites, is of dynamic nature, and thus their exact orientation is only to be obtained by laser severing.

Apart from MT orientation, we also investigated speed and dynamic properties (absolute comet number) of MT growth in both cell models. The speed of EB3 comets was fairly consistent across compartments and cell models, averaging 12.1 µm/min in SH-SY5Y- and 12.9 µm/min in iPSC-derived neurons [3]. Retrograde MT growth was generally slower than anterograde growth, with the exception of dendritic MTs in iPSC-derived neurons [3].

A former review summarized how MAPs regulate MT growth, including catastrophe and rescue frequencies as well as polymerization speed. The distinct acquisition of MAPs on MT plus and minus ends, as for example EB1 on plus ends, could be responsible for the higher polymerization rate of anterograde MTs [3,28]. Jakobs et al. further suggest that the faster growth of plus-end out MTs in axons could promote uniform MT polarity in the axon [248].

However, we did not find that axonal MTs grew substantially faster than dendritic MTs (4.4., [3,38,41,248]). Thus, axonal specification and outgrowth are probably driven by other MT regulations than growth rates, such as MT polarity, increased rescue frequency or decreased catastrophe frequency, all of which were linked to TRIM46 [74,75]. This is consistent with the observation that TRIM46 knockdown does not reduce MT growth velocity, but instead reduces the proportion of anterograde MTs and limits axonal elongation [49].

We found that MT polymerization rate in human neurons was substantially higher than in animal-based model systems [3,187]. For comparison, velocities of 0.1 µm/s (6 µm/min) have been measured in *C. elegans* [247], 0.12 µm/s (7 µm/min) in *Drosophila* dendrites [33] and 5µm/min in *Drosophila* axons [248]. In mammalian-neurons, mouse cortical neurons showed 0.1 µm/s (6 µm/min) [37], whereas rat hippocampal neurons displayed speeds of 0.08 µm/s (4.8 µm/min) [49] and 0.2-0.3 µm/s (13-19 µm/min) [41] in different studies. Importantly, the MT growth is not influenced by the type of fluorescent +TIP used for visualization [3,42]. Therefore, these discrepancies may reflect species-specific regulation of MT dynamics: human neurons might require faster polymerization because they often extend substantially longer neurites than invertebrate or rodent neurons [3]. Nevertheless, the rate of MT growth is susceptible to alterations in experimental setup that influence cell culture health, e.g., temperature, light exposure, mechanical stress, and is also strongly influenced by whether the neurons are studied *in vitro, in vivo* or *ex vivo* – with +TIP being almost twice as fast *in vivo* pyramidal mouse neurons than in dissociated cultures [31]. Hence, consistent protocols are needed for comparability.

We also quantified the frequency of MT growth events which was highest in dendrites, intermediate in the proximal axon, and least in the distal axon in both iPSC- and SH-SY5Y-derived neurons [3]. This may indicate either a relatively larger proportion of dynamic MTs or increased MT density in dendrites [3]. Indeed, several studies have reported that dendrites host more dynamic MTs than axons [31,38]. Among others [28], TRIM46 accounts for the selective stability of axonal MTs by reducing catastrophe frequency [49,74] and thereby the number of reoccurring growth cycles. Moreover, TAU likely contributes to the higher stability of MTs in axons, especially the distal part, where it is enriched the most [249].

Generally, the number of moving +TIP comets decreases (a) during neuronal maturation [31,38] and (b) with growing distance from the soma [31,38,42], expect for the very distal growth cone [42,248].

This is consistent with the task of MT reorganization during neurite formation and axonal outgrowth.

### 5.3.6. **Conclusion: AIM 3**

We investigated MT organization of iPSC-derived neurons using EB3 live-cell-imaging, focusing on MT orientation, dynamics, polymerization speed in the proximal axon, distal axon and dendrite. Both SH-SY5Y- and iPSC-derived neurons established cellular MT polarity characteristic of polarized neurons, that is, a high degree of plus-end-out MT orientation (~95% anterograde) in axons and mixed MT polarity (~75% anterograde) in dendrites. These findings highlight that MT polarization is independent from ANKG, which is absent in SH-SY5Y-derived neurons. Instead, basal levels of TRIM46 might suffice to implement MT polarity, as described in previous studies through crosslinking of parallel MTs. However, future studies should explore additional mechanisms that establish MT polarity. Unipolar MT orientation in axons presumably results from a combination of mechanisms, including TRIM46-mediated parallel MT bundling, motor-driven translocation MTs, distinct growth properties of plus- vs minus-end MTs, local MT nucleation and de novo MT generation from pre-existing MTs [3,246,248].

The observed correlation between MT directionality and axonal TAU enrichment supports a model in which MT orientation directly governs polarized protein sorting, complementing findings from AIM 2. Thus, we argue that axonal TAU sorting is achieved through directed, motor-driven transport. The specific motors, adaptors and TAU domains involved in axonal TAU (mis)sorting deserve further investigation.

Furthermore, the EB3 live-cell-imaging highlights notable differences of MT organization in human neurons and animal neurons, investigated in former studies. Human neurons had less pronounced MT polarity (~95/75% vs. ~100/60% in rodent neurons or ~100/0% in invertebrate neurons) and faster MT polymerization rates. These distinctions may reflect the maturity of the cultures as well as species-specific aspects of MT organization.

In sum, these findings show that MT polarity in human neurons is established in the absence of ANKG and suggest that TRIM46 may be sufficient to establish anterograde MT orientation in axons, although cooperating mechanisms need further investigation. SH-SY5Y-derived neurons and iPSC-derived neurons are excellent models to study human MT organization *in vitro*. This is essential to study MT-dependent TAU sorting mechanisms but also MT dysfunction downstream of TAU pathology in tauopathies. Finally, iPSC- and SH-SY5Y-derived neurons may serve as human-based *in vitro* models to study MT (dys)function in many MT-related neurological disorders – beyond tauopathies – such as synucleinopathies, ALS, HSP, CMT and Lissencephaly.

## 5.4. AIM 4) Suitability of iPSC- and SH-SY5Y-derived neurons for AD and tauopathy research

Rodent models have been the foundation of tauopathy research for many decades, but they have several downsides: In order to replicate key aspects of AD (Aβ plaques, NFTs, cognitive decline) transgenic mice are required to overexpress mutant variants of *APP*, *PSEN1/2* or *MAPT*, which do not reflect the multifactorial pathogenesis of age-related diseases, such as sporadic AD. The amino acid, interactome and isoform composition of TAU differs significantly between humans and mice, and thereby also possible interactions that influence TAU (mis)sorting. As mentioned, rodents lack all 3R TAU isoforms, but TAU isoform composition is relevant for both physiological and pathological functions of TAU: The six isoforms show distinct subcellular sorting [8-11], have different interaction partners [12], have different phosphorylation sites and aggregation propensity [13-15] and are implemented differentially in several tauopathies or result in tauopathies when in imbalance [2,9].
Lastly, rodent models suffer from poor sorting efficiency of overexpressed or transfected TAU (e.g., fluorescently tagged TAU, TAU mutants, human TAU), hindering the investigation of TAU (mis)sorting mechanisms in murine neurons [126,250]. Nevertheless, rodents have the obvious advantage of allowing the study of disease progression and therapy testing *in vivo*, but due to the aforementioned limitations, they often fail when translating pathomechanisms into therapeutic drugs. Therefore, an *in vitro* human model in which all TAU isoforms are present is needed. We investigated whether human iPSC-derived neurons or neurons derived from the human SH-SY5Y neuroblastoma cell line serve as suitable alternatives to the animal model.

IPSC-derived neurons have some exclusive advantages: They retain the genetic background of healthy donors or those affected by sAD, fAD, FTD and other tauopathies. We differentiated the WTC11 iPSC line into glutamatergic cortical neurons using doxycycline-induced expression of a Neurogenin 2 transgene. Neuronal differentiation is highly efficient (~90%) and reproducible [186]. These iPSC-derived neurons develop into polarized neurons with extensive neurite formation and arborization (4.3.), AIS formation (4.1.), compartment-specific localization of TAU, MAP2 (4.3.), as well as abundance of neuronal (NeuN) and synaptic markers (VGLUT1, synaptophysin, PSD95) [186,221]. Here, we show that axonal enrichment of endogenous TAU rises in parallel with AIS assembly and is comparable to primary mouse neurons (4.3). We also demonstrate that iPSC-derived neurons are accessible for +TIP live-cell imaging (4.4.). Thus, iPSC-derived neurons are a powerful tool to recapitulate early mechanisms of neurodevelopment (e.g., AIS formation, neuronal polarization, MT rearrangements).

However, applications of iPSC-derived neurons can extend beyond this: iPSC-derived neurons can be differentiated into various neuronal subtypes and also astrocytes and glia, allowing subtype-specific and intercellular mechanisms of disease. Unlike rodent neurons, they effectively sort exogenous TAU constructs into the axon [147,211]. We found that iPSC-derived neurons are a fairly hard-to-transfect cell type (3.2.1.7, [232]), but showed that genetic manipulation is possible using lentiviral transduction (4.5) or CRISPR/Cas9 editing (human *MAPT*-KO iPSC [147]). Importantly, in iPSC-derived neurons all six human TAU isoforms are present in principle, allowing investigation of isoform-specific TAU functions in health and disease. In this study, we only investigated total TAU but Wang et al. showed presence of both 3R and 4R TAU isoforms in *NGN2*-induced iPSC-derived neurons after 4 weeks of differentiation, and TAU phosphorylation comparable to human brains after 8 weeks of differentiation [186], whereas other iPSC differentiation procedures [192] produced neurons with mature TAU isoform patterns after only 6 months. Even though we also worked with high-speed *NGN2* differentiation, the young age (1-3 weeks) of the iPSC-derived neurons in this study could suggest the predominance of TAU isoforms of early development, i.e., 0N3R TAU. To investigate the (mis)sorting of the more mature and longer isoforms – i.e., 1N3R, 1N4R, 2N4R – which are partly retained in the soma and dendrites, longer cultivation may be needed [10,147,251].

Even though iPSC differentiation procedures continue to accelerate and simplify, the slow rate of neuronal maturation is still one of the major obstacles in the generation of iPSC-derived neurons. Week-long differentiation procedures are time- and cost-consuming and bear practical risks like cell culture contamination or cell death. While we obtained individual polarized neurons with AIS assembly after 1.5 to 2 weeks of differentiation, the generation of functional neuronal networks of *NGN2*-induced iPSC-derived neurons takes up to 3 [202] to 8 weeks [186], whereas this is accomplished in rodent cultures within 3 weeks [252]. Still, already 40%, respectively 62% of 2-week-old iPSC-derived neurons from our laboratory show spontaneous network activity in Calcium signaling experiments when in mono- or co-culture with mouse glia [147].

The slow differentiation hinders specifically research on late neurodevelopment e.g., synaptogenesis or electrophysiological processes, as well as age-related diseases. However, iPSCs of sAD patients already exhibit cellular disease phenotypes, including elevated amyloid levels or TAU hyperphosphorylation, in early stages of differentiation (already after 6 weeks), possibly allowing insights into understudied pre-disease stages [253]. Moreover, the “slow-motion” differentiation allows observation of cellular processes in a higher temporal resolution, which already shed light on mechanisms that could possibly be overlooked in animal models, e.g., previously unknown intermediate stages of development [38].

Still, one could overcome the slow rate of maturation by co-cultivating the iPSC-derived neurons with astrocytes or growing them in a 3D environment, which is known to enhance maturity [251,252,254]. Co-culturing with astrocytes enhances functional maturation – in particular synaptic transmission – and could also permit insights into astrocyte-neuron contribution to AD pathology.

Another challenge is the cellular heterogeneity in stem cell-derived studies: differences in donor genetics and epigenetics after reprogramming, somatic mutations and, importantly, non-genetic experimental factors (differentiation procedures, culture conditions, co-culturing, passage number etc.) produce high variability and limit the comparability of the many iPSC-derived neurons recently generated [184,255]. Finally, it was shown that "directed differentiation" – that is, generation of iPSCs from fibroblasts, as used in this study – leads to an epigenetic rejuvenation of the cells, possibly not desired when studying age-related diseases. To prevent this, direct conversion of fibroblasts into neurons ("direct reprogramming" or "lineage conversion") would preserve age-associated signatures, such as epigenetic marks (methylation patterns), DNA damage, shortened telomeres or reduced mitochondrial metabolism [185,256,257]. Yet, directly reprogrammed neurons also come with distinct limitations, in particular very low differentiation efficiency, variability in neuronal identity, and limited maturity (i.e., reduced competence for synapse formation) preventing reproducible high-throughput experiments [258,259]. Their use is further hampered by the limited availability and renewability of fibroblasts as starting materials, in contrast to iPSCs [202].

Finally, despite costly and long maturation procedures, line-to-line variability, the need for human neuronal cell models for TAU studies persists. The enormous progress in the field of stem cell research offers hope to overcome these methodological obstacles soon.

SH-SY5Y-derived neurons have some advantages compared to iPSC-derived neurons. As a secondary cell line, they are highly proliferative and provide a great quantity of neuronal cells for experimental assays. They are more robust to cell stress in culture and their differentiation is faster and more economic [3,193].

Already after 2 to 3 weeks of differentiation, SH-SY5Y cells transition into polarized neurons with effective TAU sorting (4.3) and show neuronal markers like βIII-tubulin, MAP2, NeuN, neuron specific enolase (NSE) and synaptic proteins such as synaptophysin or SAP-97 [194]. All six human TAU isoforms are present in principle, but the pattern is dominated by the 0N3R TAU isoform, suggesting limited maturity [260]. Like iPSC-derived neurons, they effectively sort transfected exogenous TAU [8].

The assumption that SH-SY5Y-derived neurons have limited maturity is supported by further observations: they develop fewer, shorter and thinner dendrites than, e.g., iPSC-derived or primary neurons, and their neurite branching is less pronounced (4.3, [92,193]). Most likely they

lack an AIS as a structurally defined region (5.1.4). Finally, they do not reach full electrophysiological functionality or synaptic complexity as seen in primary rodent neurons [230,261].

Furthermore, the SH-SY5Y cell line is derived from a tumor, which is accompanied by chromosomal abnormalities, among them trisomies and copy number variations [262]. These genetic alterations challenge gene editing and may disturb signaling pathways investigated in disease models. Genomic evaluation of SH-SY5Y cells predicted that AD-specific pathways could be affected in particular [263].

Moreover, differentiated SH-SY5Y-derived neurons acquire noradrenergic, cholinergic or dopaminergic properties, depending on the substance used for differentiation [194,264]. These neuronal subtypes are all present in subcortical loci affected in AD. However, the phenotype of the differentiated SH-SY5Y neurons is often heterogeneous, so that they cannot be assigned to one of these corresponding loci and subtype-specific involvement in the AD cascade cannot be specifically investigated. The precise neuronal identity should be identified, using for example single-cell transcriptomics of differentiated SH-SY5Y cells.

Finally, SH-SY5Y-derived neurons are an established cell model in many CNS disease models, including PD, AD, ALS or Huntington's disease [263]. They are an easy-to-differentiate and proliferative cell line appropriate for basic TAU studies, addressing, for example, MT dynamics, but not AIS interactions, synaptic toxicity or isoform-specific function. Low differentiation efficiency, variability in neuronal identity and limited neuronal maturity are substantial limitations.

### 5.4.1. **Conclusion: AIM 4**

Both iPSC-derived and SH-SY5Y-derived neurons overcome limitations of rodent neurons by featuring all TAU isoforms in principle, showing axonal TAU enrichment of endogenous and exogenous TAU constructs and having the ethical advantage of not requiring animal sacrifice. We found that SH-SY5Y-derived neurons are a practical and proliferative cell line appropriate for basic TAU sorting studies and investigation of MT dynamics. Low differentiation efficiency, variability in neuronal identity and limited neuronal maturity are substantial limitations. IPSC-derived neurons outperform SH-SY5Y-derived neurons in many respects: They obtain a higher degree of neuronal polarity on both the morphologic and molecular level, i.e., robust abundance of AIS markers ANKG, TRIM46, more efficient TAU sorting, extensive neurite outgrowth and branching. They do not inherit tumor-related genetic alterations, can be derived from a large genetic pool of individuals (both healthy and affected by disease), can be transformed into all neuronal subtypes and, when co-cultured, even into functional neuronal networks and 3D brain organoids. To investigate isoform-specific TAU functions and synaptotoxicity associated with TAU missorting, longer differentiation periods may be needed.

Possibly they hold promise as a model not only for tauopathy disease-modeling but also drug testing, biomarker discovery or patient-specific personalized medicine.

## 5.5. Resumé and outlook

TAU pathology is a substantial and early mediator within the pathological cascade of Alzheimer's Disease (AD) and related tauopathies. The somatodendritic missorting of TAU leads to MT destabilization, transport deficits and synaptic toxicity. In order to target TAU missorting, we aimed to explore mechanisms that enable axonal TAU enrichment. We studied the axon initial segment (AIS) as well as the neuronal MT network, as both are (a) potentially involved in axonal TAU sorting and (b) directly affected by TAU pathology. We aimed to establish a human neuronal model as an alternative to conventional rodent models to address mechanisms of basic neurodevelopment (i.e., neuronal polarization, AIS development, MAP sorting) as well as TAU pathology. For that, we used the human WTC11 iPSC line, differentiated into glutamatergic cortical neurons via a doxycycline-inducible *NGN2* transgene, as well as RA/BDNF-treated SH-SY5Y-derived neurons.

Specifically, we showed that iPSC-derived neurons have an AIS with local enrichment of both ANKG and TRIM46, as seen in primary mouse neurons. In iPSC-derived neurons, axonal sorting of endogenous TAU augments in parallel with ANKG/TRIM46 enrichment, reaching a TAU sorting efficiency comparable to primary mouse neurons after 3 weeks of differentiation. We compared neurodevelopmental stages of iPSC-derived neurons and conventional rodent neurons, finding several discrepancies as the simultaneous, not successive, abundance of ANKG and TRIM46 or the overall slower rate of differentiation in the human model. Contrarily, we showed the absence of ANKG in SH-SY5Y-derived neurons. We demonstrated that despite differences in the AIS composition, all three cell models were able to sort TAU in the axon. We furthermore implemented quantitative measures of axonal TAU and MAP2 sorting. Using +TIP live-cell imaging, we demonstrated that both iPSC- and SH-SY5Y-derived neurons exhibit a polarized MT network, characterized by uniformly anterograde MT orientation in axons, in contrast to bidirectionally oriented MTs in dendrites. We also identified probable species-dependent differences in MT organization, i.e., faster polymerization speed and less pronounced MT polarity than in non-human animal models.

In conclusion, initial neuronal polarization, axonal TAU sorting and MT polarity are not primarily dependent on ANKG. Instead, we propose that TRIM46 controls MT polarity and hypothesize that this MT organization could be the foundation of axonal TAU sorting by means of active transport. Conversely, the AIS scaffold protein ANKG seems not to be directly involved in MT polarization and the establishment of neuronal polarity, which occurs normally in ANKG-deficient SH-SY5Y-derived neurons. However, we agree with previous data demonstrating that ANKG maintains AIS integrity, TRIM46 positioning, the polarized distribution of axonal and

somatodendritic membrane proteins and electric activity in mature neurons. This is reflected in the limited maturity of AIS-deficient SH-SY5Y derived neurons.

We found that SH-SY5Y derived neurons are a practical and proliferative cell line appropriate for basic TAU sorting studies, addressing, for example, MT dynamics, but not AIS interactions, synaptic toxicity or TAU isoform-specific functions. Low differentiation efficiency, variability in neuronal identity and limited neuronal maturity are substantial limitations. Instead, we consider iPSC-derived neurons as a suitable neuronal cell model for the investigation of the AIS, MT dynamics, and TAU sorting, as well as their interplay in the context of tauopathy disease modeling. IPSC-derived neurons greatly recapitulate these aspects of neuronal polarization known from conventional rodent models while promising to overcome drawbacks of animal models in human tauopathy research. They offer various applications for preclinical and clinical TAU research: selective expression of *MAPT* variants and isoforms in *MAPT*-KO neurons, subtype-specific neuronal differentiation, co-culturing with astrocytes and microglia, development of 3D brain organoids, identification of biomarkers and drug screening.

Finally, some questions about the human AIS, TAU (mis)sorting mechanisms and iPSC-derived neurons need to be addressed:

**1. Mechanistic Insights into TRIM46 and ANKG Functions:**

While current data propose TRIM46 as a key player in MT organization and ANKG as a stabilizer of neuronal polarity, future studies should investigate additional molecular pathways that contribute to their regulation: How is TRIM46 localized to the proximal axon if not through ANKG? Recent studies have identified potential TRIM46 interaction partners in biotinylation assays, which did not include known AIS proteins (i.e., ANKG, NF-186, $Na_v$), but – among many others – α2- and β2-spectrin and several Septins [49,225]. Septins are a group of scaffold proteins associating with actin, MTs and membranes and they are involved in neurite outgrowth and polarity of neuronal traffic [265]. Silencing of Septin 5 and 6 in early development reduced TRIM46 enrichment at the AIS [225], therefore they might be a potential candidate anchoring TRIM46 at the AIS. α2- and β2-spectrins were shown to be part of a periodic cytoskeletal scaffold at the AIS [227,228], thereby also possibly involved in TRIM46 localization. Future studies should explore the function of additional binding partners recently identified. Furthermore, we should identify the human AIS interactome in iPSC-derived neurons using biotin proximity labeling (as previous biotinylation assays were performed in rat hippocampal neurons or in HEK-293T cells incubated with rat brain extracts) but also affinity purification mass spectrometry or co-immunoprecipitation for stable interactions and validation.

Moreover, RNAi-mediated knockdown of *TRIM46* and *ANK3* could help to determine their specific roles in reciprocal anchoring, MT organization and axonal TAU sorting. Future studies should avoid inefficient liposomal transfection for shRNA delivery, while lentiviral transduction

with adapted shRNA sequences and optimized titers should be pursued. Importantly, we need to aim for inducible RNAi or CRISPRi to address AIS functions in TAU (mis)sorting in developing as well as mature neurons. However, most inducible lentiviral vectors for RNAi delivery in neuronal cultures are based on tetracycline or doxycycline as inducers, but the *NGN2*-induced differentiation of the iPSCs in this study requires constant maintenance in media containing doxycycline.

**2. Further investigations into TAU sorting mechanisms:**

In this study, we observed that compartmental TAU/MAP2 sorting rose in parallel with AIS development and correlated with MT directionality in axons and dendrites. However, these findings do not demonstrate any causalities but rather serve as a basic characterization providing a quantitative assessment of AIS implementation and axonal sorting of endogenous TAU. Importantly, we already observed axonal TAU sorting in young neurons (d7) before full implementation of the AIS, suggesting alternative mechanisms enabling initial TAU sorting into the axon. Previous studies reported that polarized transport occurs before the assembly of the AIS and even in *Ank3*-knockdown neurons, thus axonal TAU sorting could result from anterograde transport, already in young neurons. TAU was reported to interact with kinesin-1 via kinesin light chains 1 and 2 [199], which have a preference for anterograde MTs in the axon. FRAP experiments showed that there is a directional bias in TAU movement from the soma to the axon. To further address the hypothesis that axonal TAU sorting is mediated by anterograde transport mechanisms, which in turn depend on MT polarity, some open questions need to be addressed: Is axodendritic MT polarity established in iPSC-derived neurons already in young neurons (d7), before AIS implementation? Does *TRIM46* knockdown lead to loss of MT polarity and subsequent missorting of TAU? We observed MT polarity in SH-SY5Y-derived neurons in which TRIM46 is much less enriched than in iPSC-derived neurons and primary rodent neurons. Former studies have proposed that MT polarity is established through the cooperation of cross-linking proteins, such as TRIM46, and cytoplasmic dynein which sorts incorrectly orientated MTs out of the axon [243]. The identification of alternate MAPs responsible for MT polarization deserves further investigation.

Besides this, we should investigate the potential mechanisms of active TAU transport. Slow axonal transport, associated with cytoskeletal proteins (such as MTs) and small cytosolic proteins (such as TAU) are understudied in comparison to fast axonal transport of membranous vesicles [266]. TAU was shown to directly interact with kinesin-1 and disturbance of this interaction resulted in TAU accumulation and neurodegeneration [239,240]. Alternative motor proteins, adaptors and TAU domains involved in anterograde transport should be identified. Two recent studies showed that absence of TAU's proline-rich region 2 leads to TAU mislocalization and loss of biased anterograde movement in the axon [126,211]. We should thus

address whether this TAU domain could interact with axonal motors. Could TAU missorting, due to pathologic TAU mutations and/or altered isoform ratios, result from disturbed interaction of these variants with motors? Former studies disagreed whether *MAPT* mutations altered the rates of slow transport [5]. This matter deserves further investigation, using e.g., fluorescently tagged TAU constructs and photoactivatable forms of TAU, as done in previous studies [196,197,199,200,260]. We have recently established a *MAPT*-knockout version of our iPSC-derived neurons, in which we are able to introduce only certain TAU isoforms or variants, allowing to investigate their transport behavior individually.

**3. Challenges in iPSC-derived neuronal models:**

We showed that iPSC-derived neurons are a powerful tool to investigate early processes of neurodevelopment (e.g., neuronal polarization, AIS establishment, MT organization and TAU sorting) and thereby aimed to prove comparability to rodent neuronal models. However, other TAU-related functions known from rodent models remain to be validated in iPSC-derived neurons. Moreover, while this study focused on physiological TAU sorting mechanism and early neurodevelopment, addressing age-related cellular phenotypes and pathologic TAU missorting in AD and other tauopathies will require more advanced neuronal maturation. Given the relatively slow differentiation rate, it would be beneficial to assess the formation of functional synapses, dendritic spines and isoform-specific TAU enrichment in the iPSC-derived neurons of this study after several months of cultivation. This is imperative since synaptic toxicity and isoform-specific interactions have been shown to play a substantial role in AD pathophysiology. To avoid the epigenetic rejuvenation associated with iPSC reprogramming, unfavorable for the study of age-related pathomechanisms, an alternative strategy might be “lineage conversion”, though this method is still constrained by low efficiency and cellular heterogeneity. Finally, the *NGN2*-induced iPSC-derived neurons of this study correspond only to layer II/III cortical glutamatergic neurons. Thus, to identify subtype-specific involvement in AD and tauopathies, we have to adapt differentiation procedures. Future studies could explore co-culturing iPSC-derived neurons with astrocytes and oligodendrocytes, as well as using 3D brain organoids to better mimic the *in vivo* microenvironment. Finally, it would be interesting to determine whether alterations of the AIS or MT architecture are part of early cellular phenotypes in iPSC-derived neurons derived from patients affected with fAD, sAD and other tauopathies.

# 6. References


1. Guo T, Noble W, Hanger DP. Roles of tau protein in health and disease. *Acta Neuropathologica* 2017; **133**(5): 665-704.
2. Arendt T, Stieler JT, Holzer M. Tau and tauopathies. *Brain Research Bulletin* 2016; **126**: 238-92.
3. Breuer H, Bell-Simons M, Zempel H. Axodendritic targeting of TAU and MAP2 and microtubule polarization in iPSC-derived versus SH-SY5Y-derived human neurons. *Open Life Sciences* 2024; **19**(1).
4. Ballatore C, Lee VMY, Trojanowski JQ. Tau-mediated neurodegeneration in Alzheimer's disease and related disorders. *Nature Reviews Neuroscience* 2007; **8**: 663-72.
5. Goedert M, Spillantini MG, Jakes R, Rutherford D, Crowther RA. Multiple isoforms of human microtubule-associated protein tau: sequences and localization in neurofibrillary tangles of Alzheimer's disease. *Neuron* 1989; **3**(4): 519-26.
6. Trabzuni D, Wray S, Vandrovcova J, et al. MAPT expression and splicing is differentially regulated by brain region: Relation to genotype and implication for tauopathies. *Human Molecular Genetics* 2012; **21**(18): 4094-103.
7. Bullmann T, Holzer M, Mori H, Arendt T. Pattern of tau isoforms expression during development in vivo. *International Journal of Developmental Neuroscience* 2009; **27**(6): 591-7.
8. Bachmann S, Bell M, Klimek J, Zempel H. Differential Effects of the Six Human TAU Isoforms: Somatic Retention of 2N-TAU and Increased Microtubule Number Induced by 4R-TAU. *Frontiers in Neuroscience* 2021; **15**(May): 1-10.
9. Buchholz S, Zempel H. The six brain-specific TAU isoforms and their role in Alzheimer's disease and related neurodegenerative dementia syndromes. *Alzheimer's & Dementia* 2024; **20**(5): 3606-28.
10. Zempel H, Dennissen FJA, Kumar Y, et al. Axodendritic sorting and pathological missorting of Tau are isoform-specific and determined by axon initial segment architecture. *Journal of Biological Chemistry* 2017; **292**(29): 12192-207.
11. Liu C, Götz J. Profiling Murine Tau with 0N, 1N and 2N Isoform-Specific Antibodies in Brain and Peripheral Organs Reveals Distinct Subcellular Localization, with the 1N Isoform Being Enriched in the Nucleus. *PLOS ONE* 2014; **8**(12): e84849.
12. Liu C, Song X, Nisbet R, Götz J. Co-immunoprecipitation with Tau Isoform-specific Antibodies Reveals Distinct Protein Interactions and Highlights a Putative Role for 2N Tau in Disease*. *Journal of Biological Chemistry* 2016; **291**(15): 8173-88.
13. Adams SJ, DeTure MA, McBride M, Dickson DW, Petrucelli L. Three Repeat Isoforms of Tau Inhibit Assembly of Four Repeat Tau Filaments. *PLOS ONE* 2010; **5**(5): e10810.
14. Combs B, Voss K, Gamblin TC. Pseudohyperphosphorylation Has Differential Effects on Polymerization and Function of Tau Isoforms. *Biochemistry* 2011; **50**(44): 9446-56.
15. Dinkel P, Siddiqua A, Huynh H, Shah M, Margittai M. Variations in Filament Conformation Dictate Seeding Barrier between Three- and Four-Repeat Tau. *Biochemistry* 2011; **50**: 4330-6.
16. Boyarko B, Hook V. Human Tau Isoforms and Proteolysis for Production of Toxic Tau Fragments in Neurodegeneration. *Frontiers in Neuroscience* 2021; **15**: 702788.
17. Ittner A, Ittner LM. Dendritic Tau in Alzheimer's Disease. *Neuron* 2018; **99**: 13-27.
18. Sultan A, Nesslany F, Violet M, et al. Nuclear Tau, a key player in neuronal DNA protection. *Journal of Biological Chemistry* 2011; **286**(6): 4566-75.
19. Violet M, Delattre L, Tardivel M, et al. A major role for Tau in neuronal DNA and RNA protection in vivo under physiological and hyperthermic conditions. *Frontiers in Cellular Neuroscience* 2014; **8**(MAR).
20. Fletcher DA, Mullins RD. Cell mechanics and the cytoskeleton. *Nature* 2010; **463**(7280): 485-92.
21. Conde C, Cáceres A. Microtubule assembly, organization and dynamics in axons and dendrites. *Nature Reviews Neuroscience* 2009; **10**: 319-32.

22. Kapitein LC, Hoogenraad CC. Building the Neuronal Microtubule Cytoskeleton. *Neuron* 2015; **87**: 492-506.
23. Franker MAM, Hoogenraad CC. Microtubule-based transport – basic mechanisms, traffic rules and role in neurological pathogenesis. *Journal of Cell Science* 2013; **126**(11): 2319-29.
24. Blanquie O, Bradke F. Cytoskeleton dynamics in axon regeneration. *Current Opinion in Neurobiology* 2018; **51**: 60-9.
25. Jang E-H, Choi H, Hur E-M. Microtubule function and dysfunction in the nervous system. *Molecules and Cells* 2024; **47**(10): 100111.
26. Akhmanova A, Steinmetz MO. Tracking the ends: a dynamic protein network controls the fate of microtubule tips. *Nature Reviews Molecular Cell Biology* 2008; **9**(4): 309-22.
27. Oakley BR, Paolillo V, Zheng Y. gamma-Tubulin complexes in microtubule nucleation and beyond. *Mol Biol Cell* 2015; **26**(17): 2957-62.
28. Bowne-Anderson H, Hibbel A, Howard J. Regulation of Microtubule Growth and Catastrophe: Unifying Theory and Experiment. *Trends in Cell Biology* 2015; **25**: 769-79.
29. Muroyama A, Lechler T. Microtubule organization, dynamics and functions in differentiated cells. *Development (Cambridge)* 2017; **144**: 3012-21.
30. Wilkes OR, Moore AW. Distinct Microtubule Organizing Center Mechanisms Combine to Generate Neuron Polarity and Arbor Complexity. *Frontiers in Cellular Neuroscience* 2020; **14**.
31. Yau KW, Schätzle P, Tortosa E, et al. Dendrites In vitro and In vivo contain microtubules of opposite polarity and axon formation correlates with uniform plus-end-out microtubule orientation. *Journal of Neuroscience* 2016; **36**(4): 1071-85.
32. Yau Kah W, van Beuningen Sam FB, Cunha-Ferreira I, et al. Microtubule Minus-End Binding Protein CAMSAP2 Controls Axon Specification and Dendrite Development. *Neuron* 2014; **82**(5): 1058-73.
33. Ori-McKenney KM, Jan LY, Jan YN. Golgi Outposts Shape Dendrite Morphology by Functioning as Sites of Acentrosomal Microtubule Nucleation in Neurons. *Neuron* 2012; **76**(5): 921-30.
34. Sánchez-Huertas C, Freixo F, Viais R, Lacasa C, Soriano E, Lüders J. Non-centrosomal nucleation mediated by augmin organizes microtubules in post-mitotic neurons and controls axonal microtubule polarity. *Nature Communications* 2016; **7**.
35. Baas PW, Lin S. Hooks and comets: The story of microtubule polarity orientation in the neuron. *Developmental Neurobiology* 2011; **71**(6): 403-18.
36. Stone MC, Roegiers F, Rolls MM. Microtubules have opposite orientation in axons and dendrites of Drosophila neurons. *Mol Biol Cell* 2008; **19**(10): 4122-9.
37. Kleele T, Marinković P, Williams PR, et al. An assay to image neuronal microtubule dynamics in mice. *Nature Communications* 2014; **5**.
38. Lindhout FW, Kooistra R, Portegies S, et al. Quantitative mapping of transcriptome and proteome dynamics during polarization of human ipsc-derived neurons. *eLife* 2020; **9**: 1-25.
39. van Beuningen SFB, Hoogenraad CC. Neuronal polarity: Remodeling microtubule organization. *Current Opinion in Neurobiology* 2016; **39**: 1-7.
40. Nakata T, Hirokawa N. Microtubules provide directional cues for polarized axonal transport through interaction with kinesin motor head. *Journal of Cell Biology* 2003; **162**(6): 1045-55.
41. Kollins KM, Bell RL, Butts M, Withers GS. Dendrites differ from axons in patterns of microtubule stability and polymerization during development. *Neural Development* 2009; **4**(1).
42. Stepanova T, Slemmer J, Hoogenraad CC, et al. Visualization of Microtubule Growth in Cultured Neurons via the Use of EB3-GFP (End-Binding Protein 3-Green Fluorescent Protein). *Journal of Neuroscience* 2003; **23**(7): 2655-64.
43. Witte H, Neukirchen D, Bradke F. Microtubule stabilization specifies initial neuronal polarization. *Journal of Cell Biology* 2008; **180**(3): 619-32.
44. Baas PW, Slaughter T, Brown A, Black MM. Microtubule dynamics in axons and dendrites. *Journal of Neuroscience Research* 1991; **30**(1): 134-53.

45. Hammond JW, Huang C-F, Kaech S, Jacobson C, Banker G, Verhey KJ. Posttranslational Modifications of Tubulin and the Polarized Transport of Kinesin-1 in Neurons. *Molecular Biology of the Cell* 2010; **21**: 572-83.
46. Konishi Y, Setou M. Tubulin tyrosination navigates the kinesin-1 motor domain to axons. *Nature Neuroscience* 2009; **12**(5): 559-67.
47. Baas PW, Ahmad FJ, Pienkowski TP, Brown A, Black MM. Sites of microtubule stabilization for the axon. *The Journal of Neuroscience* 1993; **13**(5): 2177.
48. Harterink M, Vocking K, Pan X, et al. Trim46 organizes microtubule fasciculation in the axon initial segment. *Journal of Neuroscience* 2019; **39**(25): 4864-73.
49. Van Beuningen SFB, Will L, Harterink M, et al. TRIM46 Controls Neuronal Polarity and Axon Specification by Driving the Formation of Parallel Microtubule Arrays. *Neuron* 2015; **88**(6): 1208-26.
50. Lüders J. The Microtubule Cytoskeleton: Springer Vienna; 2016.
51. Akhmanova A, Hoogenraad CC. Microtubule minus-end-targeting proteins. *Current Biology* 2015; **25**: R162-R71.
52. Sferra A, Nicita F, Bertini E. Microtubule Dysfunction: A Common Feature of Neurodegenerative Diseases. *International Journal of Molecular Sciences* 2020; **21**(19).
53. De Vos KJ, Grierson AJ, Ackerley S, Miller CCJ. Role of axonal transport in neurodegenerative diseases. *Annu Rev Neurosci* 2008; **31**(1): 151-73.
54. McMurray CT. Neurodegeneration: diseases of the cytoskeleton? *Cell Death & Differentiation* 2000; **7**(10): 861-5.
55. Roy S, Zhang B, Lee VMY, Trojanowski JQ. Axonal transport defects: A common theme in neurodegenerative diseases. *Acta Neuropathologica* 2005; **109**: 5-13.
56. Ganne A, Balasubramaniam M, Ayyadevara H, et al. In silico analysis of TUBA4A mutations in Amyotrophic Lateral Sclerosis to define mechanisms of microtubule disintegration. *Scientific Reports* 2023; **13**(1).
57. Lasser M, Tiber J, Lowery LA. The role of the microtubule cytoskeleton in neurodevelopmental disorders. *Frontiers in Cellular Neuroscience* 2018; **12**.
58. Rasband MN. The axon initial segment and the maintenance of neuronal polarity. *Nature Reviews Neuroscience* 2010; **11**: 552-62.
59. Hedstrom KL, Ogawa Y, Rasband MN. AnkyrinG is required for maintenance of the axon initial segment and neuronal polarity. *Journal of Cell Biology* 2008; **183**(4): 635-40.
60. Sobotzik JM, Sie JM, Politi C, et al. AnkyrinG is required to maintain axo-dendritic polarity in vivo. *Proceedings of the National Academy of Sciences of the United States of America* 2009; **106**(41): 17564-9.
61. Leterrier C. The axon initial segment: An updated viewpoint. *Journal of Neuroscience* 2018; **38**(9): 2135-45.
62. Leterrier C, Potier J, Caillol G, Debarnot C, Rueda Boroni F, Dargent B. Nanoscale Architecture of the Axon Initial Segment Reveals an Organized and Robust Scaffold. *Cell Reports* 2015; **13**(12): 2781-93.
63. Jenkins PM, Kim N, Jones SL, et al. Giant ankyrin-G: A critical innovation in vertebrate evolution of fast and integrated neuronal signaling. *Proceedings of the National Academy of Sciences of the United States of America* 2015; **112**(4): 957-64.
64. Leterrier C, Vacher H, Fache MP, et al. End-binding proteins EB3 and EB1 link microtubules to ankyrin G in the axon initial segment. *Proceedings of the National Academy of Sciences of the United States of America* 2011; **108**(21): 8826-31.
65. Hedstrom KL, Xu X, Ogawa Y, et al. Neurofascin assembles a specialized extracellular matrix at the axon initial segment. *Journal of Cell Biology* 2007; **178**(5): 875-86.
66. Galiano MR, Jha S, Ho TSY, et al. A distal axonal cytoskeleton forms an intra-axonal boundary that controls axon initial segment assembly. *Cell* 2012; **149**(5): 1125-39.
67. Gutzmann A, Ergül N, Grossmann R, Schultz C, Wahle P, Engelhardt M. A period of structural plasticity at the axon initial segment in developing visual cortex. *Frontiers in neuroanatomy* 2014; **8**: 11.
68. Alpizar S, Baker A, Gulledge A, Hoppa M. Loss of Neurofascin-186 Disrupts Alignment of AnkyrinG Relative to Its Binding Partners in the Axon Initial Segment. *Frontiers in Cellular Neuroscience* 2019; **13**.

69. Zhou D, Lambert S, Malen PL, Carpenter S, Boland LM, Bennett V. AnkyrinG Is Required for Clustering of Voltage-gated Na Channels at Axon Initial Segments and for Normal Action Potential Firing. *Journal of Cell Biology* 1998; **143**(5): 1295-304.
70. Jenkins SM, Bennett V. Ankyrin-G coordinates assembly of the spectrin-based membrane skeleton, voltage-gated sodium channels, and L1 CAMs at Purkinje neuron initial segments. *Journal of Cell Biology* 2001; **155**(5): 739-46.
71. Short KM, Cox TC. Subclassification of the RBCC/TRIM Superfamily Reveals a Novel Motif Necessary for Microtubule Binding *<sup> </sup>. *Journal of Biological Chemistry* 2006; **281**(13): 8970-80.
72. Vuong JK, Ergin V, Chen L, Zheng S. Multilayered regulations of alternative splicing, NMD, and protein stability control temporal induction and tissue-specific expression of TRIM46 during axon formation. *Nature Communications* 2022; **13**(1): 2081.
73. Leterrier C, Dubey P, Roy S. The nano-architecture of the axonal cytoskeleton. *Nature Reviews Neuroscience* 2017; **18**(12): 713-26.
74. Fréal A, Rai D, Tas RP, et al. Feedback-Driven Assembly of the Axon Initial Segment. *Neuron* 2019; **104**(2): 305-21.e8.
75. Kneynsberg A, Vega I, Kanaan NM. Trim46 knockdown causes neuronal Tau redistribution and increases axosomatic Tau diffusion. Alzheimer's & Dementia 2019; **15**: 1622.
76. Curcio M, Bradke F. Microtubule Organization in the Axon: TRIM46 Determines the Orientation. *Neuron* 2015; **88**(6): 1072-4.
77. Angelides KJ, Elmer LW, Loftus D, Elson E. Distribution and lateral mobility of voltage-dependent sodium channels in neurons. *Journal of Cell Biology* 1988; **106**(6): 1911-25.
78. Schafer DP, Jha S, Liu F, Akella T, McCullough LD, Rasband MN. Disruption of the axon initial segment cytoskeleton is a new mechanism for neuronal injury. *Journal of Neuroscience* 2009; **29**(42): 13242-54.
79. Petersen AV, Cotel F, Perrier JF. Plasticity of the Axon Initial Segment: Fast and Slow Processes with Multiple Functional Roles. *Neuroscientist* 2017; **23**(4): 364-73.
80. Antón-Fernández A, León-Espinosa G, DeFelipe J, Muñoz A. Pyramidal cell axon initial segment in Alzheimer´s disease. *Scientific Reports* 2022; **12**(1): 8722.
81. Ma F, Xu J, Liu Y, et al. The amyloid precursor protein modulates the position and length of the axon initial segment offering a new perspective on Alzheimer's disease genetics. *bioRxiv* 2022: 2022.01.23.477413.
82. Sun X, Wu Y, Gu M, et al. Selective filtering defect at the axon initial segment in Alzheimer's disease mouse models. *Proceedings of the National Academy of Sciences of the United States of America* 2014; **111**(39): 14271-6.
83. Wang Y, Guan M, Wang H, et al. The largest isoform of Ankyrin-G is required for lattice structure of the axon initial segment. *Biochemical and Biophysical Research Communications* 2021; **578**: 28-34.
84. Liu C, Zhang L, Wu J, et al. AnkG hemizygous mice present cognitive impairment and elevated anxiety/depressive-like traits associated with decreased expression of GABA receptors and postsynaptic density protein. *Experimental Brain Research* 2017; **235**(11): 3375-90.
85. Iqbal Z, Vandeweyer G, Van der voet M, et al. Homozygous and heterozygous disruptions of ANK3: At the crossroads of neurodevelopmental and psychiatric disorders. *Human Molecular Genetics* 2013; **22**(10): 1960-70.
86. Morgan AR, Hamilton G, Turic D, et al. Association analysis of 528 intra-genic SNPs in a region of chromosome 10 linked to late onset alzheimer's disease. *American Journal of Medical Genetics, Part B: Neuropsychiatric Genetics* 2008; **147**(6): 727-31.
87. Hsu WCJ, Nilsson CL, Laezza F. Role of the axonal initial segment in psychiatric disorders: Function, dysfunction, and intervention. *Frontiers in Psychiatry* 2014; **5**(AUG): 1-11.
88. Wimmer VC, Reid CA, So EYW, Berkovic SF, Petrou S. Axon initial segment dysfunction in epilepsy. *Journal of Physiology* 2010; **588**(11): 1829-40.
89. Fujitani M, Otani Y, Miyajima H. Pathophysiological Roles of Abnormal Axon Initial Segments in Neurodevelopmental Disorders. *Cells* 2021; **10**(8).
90. Guan F, Gao S, Sheng H, et al. Trim46 knockout impaired neuronal architecture and caused hypoactive behavior in rats. *Developmental Dynamics* 2024; **253**(7): 659-76.

91. Barnes AP, Polleux F. Establishment of axon-dendrite polarity in developing neurons. *Annual Review of Neuroscience* 2009; **32**: 347-81.
92. Bell M, Bachmann S, Klimek J, Langerscheidt F, Zempel H. Axonal TAU Sorting Requires the C-terminus of TAU but is Independent of ANKG and TRIM46 Enrichment at the AIS. *Neuroscience* 2021: 1-17.
93. Dotti CG, Sullivan CA, Banker GA. The Establishment of Polarity by Hippocampal Neurons in Culture. *The Journal of Neuroscience* 1988; **8**(4): 1454-68.
94. Powell SK, Rivas RJ, Rodriguez-Boulan E, Hatten ME. Development of polarity in cerebellar granule neurons. *Journal of Neurobiology* 1997; **32**(2): 223-36.
95. Baron DM, Fenton AR, Saez-Atienzar S, et al. ALS-associated KIF5A mutations abolish autoinhibition resulting in a toxic gain of function. *Cell Rep* 2022; **39**(1): 110598.
96. Zhang L, Wei X. The Roles of Par3, Par6, and aPKC Polarity Proteins in Normal Neurodevelopment and in Neurodegenerative and Neuropsychiatric Disorders. *J Neurosci* 2022; **42**(24): 4774-93.
97. den Hoed J, Sollis E, Venselaar H, Estruch SB, Deriziotis P, Fisher SE. Functional characterization of TBR1 variants in neurodevelopmental disorder. *Sci Rep* 2018; **8**(1): 14279.
98. Hodgkinson CA, Goldman D, Jaeger J, et al. Disrupted in schizophrenia 1 (DISC1): association with schizophrenia, schizoaffective disorder, and bipolar disorder. *Am J Hum Genet* 2004; **75**(5): 862-72.
99. Saillour Y, Carion N, Quelin C, et al. LIS1-related isolated lissencephaly: spectrum of mutations and relationships with malformation severity. *Arch Neurol* 2009; **66**(8): 1007-15.
100. Braak H, Braak E. Neuropathological stageing of Alzheimer-related changes. *Acta Neuropathologica* 1991; **82**(4): 239-59.
101. Zhang B, Maiti A, Shively S, et al. Microtubule-binding drugs offset tau sequestration by stabilizing microtubules and reversing fast axonal transport deficits in a tauopathy model. *Proc Natl Acad Sci U S A* 2005; **102**(1): 227-31.
102. Harada A, Oguchi K, Okabe S, et al. Altered microtubule organization in small-calibre axons of mice lacking tau protein. *Nature* 1994; **369**(6480): 488-91.
103. Metcalfe MJ, Figueiredo-Pereira ME. Relationship between tau pathology and neuroinflammation in Alzheimer's disease. *Mount Sinai Journal of Medicine* 2010; **77**(1): 50-8.
104. Yoshiyama Y, Higuchi M, Zhang B, et al. Synapse Loss and Microglial Activation Precede Tangles in a P301S Tauopathy Mouse Model. *Neuron* 2007; **53**(3): 337-51.
105. SantaCruz K, Lewis J, Spires T, et al. Tau Suppression in a Neurodegenerative Mouse Model Improves Memory Function. *Science* 2005; **309**(5733): 476-81.
106. Zhang H, Cao Y, Ma L, Wei Y, Li H. Possible Mechanisms of Tau Spread and Toxicity in Alzheimer's Disease. *Front Cell Dev Biol* 2021; (2296-634X (Print)).
107. Hoover BR, Reed MN, Su J, et al. Tau Mislocalization to Dendritic Spines Mediates Synaptic Dysfunction Independently of Neurodegeneration. *Neuron* 2010; **68**(6): 1067-81.
108. Ittner LM, Ke YD, Delerue F, et al. Dendritic Function of Tau Mediates Amyloid-β Toxicity in Alzheimer's Disease Mouse Models. *Cell* 2010; **142**(3): 387-97.
109. Roberson ED, Scearce-Levie K, Palop JJ, et al. Reducing Endogenous Tau Ameliorates Amyloid β-Induced Deficits in an Alzheimer's Disease Mouse Model. *Science* 2007; **316**(5825): 750-4.
110. Zempel H, Luedtke J, Kumar Y, et al. Amyloid-β oligomers induce synaptic damage via Tau-dependent microtubule severing by TTLL6 and spastin. *EMBO Journal* 2013; **32**(22): 2920-37.
111. Qiang L, Yu W, Andreadis A, Luo M, Baas PW. Tau protects microtubules in the axon from severing by katanin. *Journal of Neuroscience* 2006; **26**(12): 3120-9.
112. Tai HC, Serrano-Pozo A, Hashimoto T, Frosch MP, Spires-Jones TL, Hyman BT. The synaptic accumulation of hyperphosphorylated tau oligomers in Alzheimer disease is associated with dysfunction of the ubiquitin-proteasome system. *Am J Pathol* 2012; **181**(4): 1426-35.
113. Koren SA, Hamm MJ, Meier SE, et al. Tau drives translational selectivity by interacting with ribosomal proteins. *Acta Neuropathol* 2019; **137**(4): 571-83.

114. Rossi G, Conconi D, Panzeri E, et al. Mutations in MAPT Gene Cause Chromosome Instability and Introduce Copy Number Variations Widely in the Genome. *Journal of Alzheimer's Disease* 2013; **33**(4): 969-82.
115. Li X, Kumar Y, Zempel H, Mandelkow EM, Biernat J, Mandelkow E. Novel diffusion barrier for axonal retention of Tau in neurons and its failure in neurodegeneration. *EMBO Journal* 2011; **30**(23): 4825-37.
116. Hanger DP, Anderton BH, Noble W. Tau phosphorylation: the therapeutic challenge for neurodegenerative disease. *Trends in Molecular Medicine* 2009; **15**(3): 112-9.
117. Stancu IC, Vasconcelos B, Terwel D, Dewachter I. Models of β-amyloid induced Tau-pathology: the long and "folded" road to understand the mechanism. *Molecular neurodegeneration* 2014; **9**: 51-.
118. Zempel H, Thies E, Mandelkow E, Mandelkow EM. Aβ oligomers cause localized Ca2+ elevation, missorting of endogenous Tau into dendrites, Tau phosphorylation, and destruction of microtubules and spines. *Journal of Neuroscience* 2010; **30**(36): 11938-50.
119. Zhang B, Higuchi M, Yoshiyama Y, et al. Retarded axonal transport of R406W mutant tau in transgenic mice with a neurodegenerative tauopathy. *Journal of Neuroscience* 2004; **24**(19): 4657-67.
120. Moore KM, Nicholas J, Grossman M, et al. Age at symptom onset and death and disease duration in genetic frontotemporal dementia: an international retrospective cohort study. *The Lancet Neurology* 2020; **19**(2): 145-56.
121. Elbaum-Garfinkle S, Cobb G, Compton JT, Li X-H, Rhoades E. Tau mutants bind tubulin heterodimers with enhanced affinity. *Proceedings of the National Academy of Sciences* 2014; **111**(17): 6311-6.
122. Dayanandan R, Van Slegtenhorst M, Mack TGA, et al. Mutations in tau reduce its microtubule binding properties in intact cells and affect its phosphorylation. *FEBS Letters* 1999; **446**(2-3): 228-32.
123. D'Souza I, Poorkaj P, Hong M, et al. Missense and silent tau gene mutations cause frontotemporal dementia with parkinsonism-chromosome 17 type, by affecting multiple alternative RNA splicing regulatory elements. *Proceedings of the National Academy of Sciences* 1999; **96**(10): 5598-603.
124. Hong M, Zhukareva V, Vogelsberg-Ragaglia V, et al. Mutation-Specific Functional Impairments in Distinct Tau Isoforms of Hereditary FTDP-17. *Science* 1998; **282**(5395): 1914-7.
125. Rodriguez Martin T, Pooler A, Lau D, et al. Reduced number of axonal mitochondria and tau hypophosphorylation in mouse P301L tau knockin neurons. *Neurobiology of disease* 2015; **85**.
126. Iwata M, Watanabe S, Yamane A, Miyasaka T, Misonou H. Regulatory mechanisms for the axonal localization of tau protein in neurons. *Molecular Biology of the Cell* 2019; **30**(19): 2441-57.
127. Zhang B, Higuchi M, Yoshiyama Y, et al. Retarded Axonal Transport of R406W Mutant Tau in Transgenic Mice with a Neurodegenerative Tauopathy. *The Journal of Neuroscience* 2004; **24**(19): 4657.
128. Hartmann C, Anskat M, Ehrlich M, Sterneckert J, Pal A, Hermann A. MAPT Mutations V337M and N297K Alter Organelle Trafficking in Frontotemporal Dementia Patient-Specific Motor Neurons. *Biomedicines* 2024; **12**(3).
129. Chang E, Kim S, Yin H, Nagaraja HN, Kuret J. Pathogenic missense MAPT mutations differentially modulate tau aggregation propensity at nucleation and extension steps. *Journal of Neurochemistry* 2008; **107**(4): 1113-23.
130. Rossi G, Tagliavini F. Frontotemporal lobar degeneration: old knowledge and new insight into the pathogenetic mechanisms of tau mutations. *Frontiers in aging neuroscience* 2015; **7:192**.
131. Gauthier-Kemper A, Weissmann C, Golovyashkina N, et al. The frontotemporal dementia mutation R406W blocks tau's interaction with the membrane in an annexin A2–dependent manner. *The Journal of cell biology* 2011; **192**: 647-61.
132. Zhang Y, Wu KM, Yang L, Dong Q, Yu JT. Tauopathies: new perspectives and challenges. *Molecular Neurodegeneration* 2022; **17**.

133. Moreira PI, Smith MA, Zhu X, Nunomura A, Castellani RJ, Perry G. Oxidative Stress and Neurodegeneration. *Ann NY Acad Sci* 2005; **1043**: 545-52.
134. Zhao X, Kotilinek LA, Smith B, et al. Caspase-2 cleavage of tau reversibly impairs memory. *Nature Medicine* 2016; **22**(11): 1268-76.
135. Katsumoto A, Takeuchi H, Tanaka F. Tau Pathology in Chronic Traumatic Encephalopathy and Alzheimer's Disease: Similarities and Differences. *Frontiers in Neurology* 2019; **10**.
136. Tsushima H, Emanuele M, Polenghi A, et al. HDAC6 and RhoA are novel players in Abeta-driven disruption of neuronal polarity. *Nature Communications* 2015; **6**(1): 7781.
137. Marin MA, Ziburkus J, Jankowsky J, Rasband MN. Amyloid-β plaques disrupt axon initial segments. *Experimental Neurology* 2016; **281**: 93-8.
138. Sohn PD, Tracy TE, Son HI, et al. Acetylated tau destabilizes the cytoskeleton in the axon initial segment and is mislocalized to the somatodendritic compartment. *Molecular Neurodegeneration* 2016; **11**(1).
139. Aronov S, Aranda G, Behar L, Ginzburg I. Axonal Tau mRNA Localization Coincides with Tau Protein in Living Neuronal Cells and Depends on Axonal Targeting Signal. *The Journal of Neuroscience* 2001; **21**(17): 6577-.
140. Hirokawa N, Funakoshi T, Sato-Harada R, Kanai Y. Selective stabilization of tau in axons and microtubule-associated protein 2C in cell bodies and dendrites contributes to polarized localization of cytoskeletal proteins in mature neurons. *Journal of Cell Biology* 1996; **132**(4): 667-79.
141. Noble W, Hanger DP, Miller CC, Lovestone S. The importance of tau phosphorylation for neurodegenerative diseases. *Front Neurol* 2013; **4**: 83.
142. Boucher D, Larcher J-C, Gros F, Denoulet P. Polyglutamylation of Tubulin as a Progressive Regulator of in Vitro Interactions between the Microtubule-Associated Protein Tau and Tubulin. *Biochemistry* 1994; **33**(41): 12471-7.
143. Scholz T, Mandelkow E. Transport and diffusion of Tau protein in neurons. *Cellular and Molecular Life Sciences* 2014; **71**: 3139-50.
144. Farías GG, Guardia CM, Britt DJ, Guo X, Bonifacino JS. Sorting of Dendritic and Axonal Vesicles at the Pre-axonal Exclusion Zone. *Cell Reports* 2015; **13**(6): 1221-32.
145. Song Ah, Wang D, Chen G, et al. A Selective Filter for Cytoplasmic Transport at the Axon Initial Segment. *Cell* 2009; **136**(6): 1148-60.
146. Nakada C, Ritchie K, Oba Y, et al. Accumulation of anchored proteins forms membrane diffusion barriers during neuronal polarization. *Nature Cell Biology* 2003; **5**(7): 626-32.
147. Buchholz S, Kabbani MAA, Bell-Simons M, et al. The tau isoform 1N4R confers vulnerability of MAPT knockout human iPSC-derived neurons to amyloid beta and phosphorylated tau-induced neuronal dysfunction. *Alzheimer's & Dementia* 2025; **n/a**(n/a): e14403.
148. Kovacs GG. Tauopathies. *Handbook of Clinical Neurology* 2018; **145**: 355-68.
149. Niu H, Álvarez-Álvarez I, Guillén-Grima F, Aguinaga-Ontoso I. Prevalencia e incidencia de la enfermedad de Alzheimer en Europa: metaanálisis. *Neurologia* 2017; **32**(8): 523-32.
150. Nichols E, Steinmetz JD, Vollset SE, et al. Estimation of the global prevalence of dementia in 2019 and forecasted prevalence in 2050: an analysis for the Global Burden of Disease Study 2019. *The Lancet Public Health* 2022; **7**(2): e105-e25.
151. Prince M. World Alzheimer Report 2015: The Global Impact of Dementia | Alzheimer's Disease International. *World Alzheimer's Report* 2015: 1-87.
152. McKee AC, Abdolmohammadi B, Stein TD. The neuropathology of chronic traumatic encephalopathy. 1 ed: Elsevier B.V.; 2018.
153. Buée L, Delacourte A. Comparative biochemistry of tau in progressive supranuclear palsy, corticobasal degeneration, FTDP-17 and Pick's disease. *Brain Pathology* 1999; **9**(4): 681-93.
154. Knopman DS, Amieva H, Petersen RC, et al. Alzheimer disease. *Nature Reviews Disease Primers* 2021; **7**(1).
155. Ke YD, Suchowerska AK, van der Hoven J, et al. Lessons from Tau-Deficient Mice. *International Journal of Alzheimer's Disease* 2012; **2012**(1): 873270.

156. De Felice FG, Velasco PT, Lambert MP, et al. Aβ Oligomers Induce Neuronal Oxidative Stress through an N-Methyl-D-aspartate Receptor-dependent Mechanism That Is Blocked by the Alzheimer Drug Memantine*. *Journal of Biological Chemistry* 2007; **282**(15): 11590-601.
157. Maezawa I, Zimin P, Wulff H, Jin L-W. Amyloid- Protein Oligomer at Low Nanomolar Concentrations Activates Microglia and Induces Microglial Neurotoxicity. *The Journal of biological chemistry* 2010; **286**: 3693-706.
158. Söllvander S, Nikitidou E, Brolin R, et al. Accumulation of amyloid-β by astrocytes result in enlarged endosomes and microvesicle-induced apoptosis of neurons. *Molecular Neurodegeneration* 2016; **11**(1): 38.
159. Umeda T, Tomiyama T, Sakama N, et al. Intraneuronal amyloid β oligomers cause cell death via endoplasmic reticulum stress, endosomal/lysosomal leakage, and mitochondrial dysfunction in vivo. *Journal of Neuroscience Research* 2011; **89**(7): 1031-42.
160. Cummings J, Lee G, Zhong K, Fonseca J, Taghva K. Alzheimer's disease drug development pipeline: 2021. *Alzheimer's and Dementia: Translational Research and Clinical Interventions* 2021; **7**(1).
161. Budd Haeberlein S, Aisen PS, Barkhof F, et al. Two Randomized Phase 3 Studies of Aducanumab in Early Alzheimer's Disease. *The Journal of Prevention of Alzheimer's Disease* 2022; **9**(2): 197-210.
162. van Dyck CH, Swanson CJ, Aisen P, et al. Lecanemab in Early Alzheimer's Disease. *New England Journal of Medicine* 2022; **388**(1): 9-21.
163. Sims JR, Zimmer JA, Evans CD, et al. Donanemab in Early Symptomatic Alzheimer Disease: The TRAILBLAZER-ALZ 2 Randomized Clinical Trial. *JAMA* 2023; **330**(6): 512-27.
164. Leqembi: The Case for Long-Term Dosing. Newton (MA): Alzforum. https://www.alzforum.org/news/conference-coverage/leqembi-case-long-term-dosing. (Zuletzt abgerufen am 08.07.2025)
165. Raket LL, Cummings J, Moscoso A, Villain N, Schöll M. Scenarios for the long-term efficacy of amyloid-targeting therapies in the context of the natural history of Alzheimer's disease. *Alzheimer's & Dementia* 2024; **20**(9): 6374-83.
166. European Medicines Agency (EMA). Leqembi: EPAR – Public assessment report. Amsterdam (NL): European Medicines Agency. https://www.ema.europa.eu/en/medicines/human/EPAR/leqembi (Zuletzt abgerufen am 08.07.2025)
167. Biotechnology Innovation Organization, Informa Pharma Intelligence, QLS Advisors. Clinical development success rates and contributing factors 2011–2020. London: Informa UK Ltd. https://go.bio.org/rs/490-EHZ-999/images/ClinicalDevelopmentSuccessRates2011_2020.pdf (Zuletzt abgerufen am 12.08.2025)
168. Miller G. Is pharma running out of brainy ideas? *Science* 2010; **329**(5991): 502-4.
169. Drummond E, Wisniewski T. Alzheimer's disease: experimental models and reality. *Acta Neuropathologica* 2017; **133**.
170. Granzotto A, Vissel B, Sensi SL. Lost in translation: Inconvenient truths on the utility of mouse models in Alzheimer's disease research. *eLife* 2024; **13**: e90633.
171. Fisher EMC, Bannerman DM. Mouse models of neurodegeneration: Know your question, know your mouse. *Science Translational Medecine* 2019; **11**(493): 1818-.
172. Götz J, Ittner LM. Animal models of Alzheimer's disease and frontotemporal dementia. *Nature Reviews Neuroscience* 2008; **9**(7): 532-44.
173. Alzforum. Research Models. https://www.alzforum.org/research-models/alzheimers-disease (Zuletzt abgerufen am 28.05.2025)
174. Hernández F, Merchán-Rubira J, Vallés-Saiz L, Rodríguez-Matellán A, Avila J. Differences Between Human and Murine Tau at the N-terminal End. *Frontiers in Aging Neuroscience* 2020; **12**(January): 1-6.
175. Marro SG, Chanda S, Yang N, et al. Neuroligin-4 Regulates Excitatory Synaptic Transmission in Human Neurons. *Neuron* 2019; **103**(4): 617-26.e6.
176. Penney J, Ralvenius WT, Tsai LH. Modeling Alzheimer's disease with iPSC-derived brain cells. *Molecular Psychiatry* 2020; **25**: 148-67.

177. Hernández F, Cuadros R, Ollá I, et al. Differences in structure and function between human and murine tau. *Biochim Biophys Acta Mol Basis Dis* 2019; **1865**(8): 2024-30.
178. Kavanagh T, Halder A, Drummond E. Tau interactome and RNA binding proteins in neurodegenerative diseases. *Molecular Neurodegeneration* 2022; **17**(1): 66.
179. Goode BL, Chau M, Denis PE, Feinstein SC. Structural and Functional Differences between 3-Repeat and 4-Repeat Tau Isoforms: IMPLICATIONS FOR NORMAL TAU FUNCTION AND THE ONSET OF NEURODEGENERATIVE DISEASE*. *Journal of Biological Chemistry* 2000; **275**(49): 38182-9.
180. Panda D, Samuel JC, Massie M, Feinstein SC, Wilson L. Differential regulation of microtubule dynamics by three- and four-repeat tau: Implications for the onset of neurodegenerative disease. *Proceedings of the National Academy of Sciences* 2003; **100**(16): 9548-53.
181. Rösler TW, Tayaranian Marvian A, Brendel M, et al. Four-repeat tauopathies. *Progress in Neurobiology* 2019; **180**(June): 101644-.
182. Andorfer C, Kress Y, Espinoza M, et al. Hyperphosphorylation and aggregation of tau in mice expressing normal human tau isoforms. *Journal of Neurochemistry* 2003; **86**(3): 582-90.
183. Webster SJ, Bachstetter AD, Nelson PT, Schmitt FA, Van Eldik LJ. Using mice to model Alzheimer's dementia: an overview of the clinical disease and the preclinical behavioral changes in 10 mouse models. *Frontiers in Genetics* 2014; **Volume 5 - 2014**.
184. Ichida JK, Kiskinis E. Probing disorders of the nervous system using reprogramming approaches. *The EMBO Journal* 2015; **34**(11): 1456-77.
185. Mertens J, Marchetto MC, Bardy C, Gage FH. Evaluating cell reprogramming, differentiation and conversion technologies in neuroscience. *Nature Reviews Neuroscience* 2016; **17**(7): 424-37.
186. Wang C, Ward ME, Chen R, et al. Scalable Production of iPSC-Derived Human Neurons to Identify Tau-Lowering Compounds by High-Content Screening. *Stem Cell Reports* 2017; **9**(4): 1221-33.
187. Allroggen N, Breuer H, Bachmann S, Bell M, Zempel H. Studying Microtubule Dynamics in Human Neurons: Two-Dimensional Microtubule Tracing and Kymographs in iPSC- and SH-SY5Y-Derived Neurons for Tau Research. In: Smet-Nocca C, ed. Tau Protein: Methods and Protocols. New York, NY: Springer US; 2024: 561-80.
188. Barak M, Fedorova V, Pospisilova V, et al. Human iPSC-Derived Neural Models for Studying Alzheimer's Disease: from Neural Stem Cells to Cerebral Organoids. *Stem Cell Reviews and Reports* 2022; **18**(2): 792-820.
189. Fleeman RM, Proctor EA. Astrocytic Propagation of Tau in the Context of Alzheimer's Disease. *Frontiers in Cellular Neuroscience* 2021; **15**.
190. Miao J, Ma H, Yang Y, et al. Microglia in Alzheimer's disease: pathogenesis, mechanisms, and therapeutic potentials. *Frontiers in Aging Neuroscience* 2023; **Volume 15 - 2023**.
191. Verkhratsky A, Olabarria M, Noristani HN, Yeh C-Y, Rodriguez JJ. Astrocytes in Alzheimer's Disease. *Neurotherapeutics* 2010; **7**(4): 399-412.
192. Beevers JE, Lai MC, Collins E, et al. MAPT Genetic Variation and Neuronal Maturity Alter Isoform Expression Affecting Axonal Transport in iPSC-Derived Dopamine Neurons. *Stem Cell Reports* 2017; **9**(2): 587-99.
193. Bell M, Zempel H. SH-SY5Y-derived neurons: A human neuronal model system for investigating TAU sorting and neuronal subtype-specific TAU vulnerability. *Reviews in the Neurosciences* 2022; **33**(1): 1-15.
194. Kovalevich J, Langford D. Considerations for the use of SH-SY5Y neuroblastoma cells in neurobiology. *Methods in Molecular Biology* 2013; **1078**: 9-21.
195. Langerscheidt F, Bell-Simons M, Zempel H. Differentiating SH-SY5Y Cells into Polarized Human Neurons for Studying Endogenous and Exogenous Tau Trafficking: Four Protocols to Obtain Neurons with Noradrenergic, Dopaminergic, and Cholinergic Properties. In: Smet-Nocca C, ed. Tau Protein: Methods and Protocols. New York, NY: Springer US; 2024: 521-32.

196. Hinrichs MH, Jalal A, Brenner B, Mandelkow E, Kumar S, Scholz T. Tau protein diffuses along the microtubule lattice. *Journal of Biological Chemistry* 2012; **287**(46): 38559-68.
197. Konzack S, Thies E, Marx A, Mandelkow EM, Mandelkow E. Swimming against the tide: Mobility of the microtubule-associated protein tau in neurons. *Journal of Neuroscience* 2007; **27**(37): 9916-27.
198. Kuznetsov IA, Kuznetsov AV. Modeling tau transport in the axon initial segment. *Mathematical Biosciences* 2020; **329**: 108468-.
199. Utton MA, Noble WJ, Hill JE, Anderton BH, Hanger DP. Molecular motors implicated in the axonal transport of tau and α-synuclein. *Journal of Cell Science* 2005; **118**(20): 4645-54.
200. Utton MA, Connell J, Asuni AA, et al. The Slow Axonal Transport of the Microtubule-Associated Protein Tau and the Transport Rates of Different Isoforms and Mutants in Cultured Neurons. *The Journal of Neuroscience* 2002; **22**(15): 6394.
201. Buchholz S, Bell-Simons M, Cakmak C, Klimek J, Gan L, Zempel H. Cultivation, Differentiation, and Lentiviral Transduction of Human-Induced Pluripotent Stem Cell (hiPSC)-Derived Glutamatergic Neurons for Studying Human Tau. In: Smet-Nocca C, ed. Tau Protein: Methods and Protocols. New York, NY: Springer US; 2024: 533-49.
202. Zhang Y, Pak CH, Han Y, et al. Rapid single-step induction of functional neurons from human pluripotent stem cells. *Neuron* 2013; **78**(5): 785-98.
203. Kang S, Chen X, Gong S, et al. Characteristic analyses of a neural differentiation model from iPSC-derived neuron according to morphology, physiology, and global gene expression pattern. *Scientific Reports* 2017; **7**(1): 12233.
204. National Center for Biotechnology Information (NCBI). Primer-BLAST. Bethesda (MD): National Library of Medicine. https://www.ncbi.nlm.nih.gov/tools/primer-blast/ (Zuletzt abgerufen am 07.07.2025)
205. Broad Institute. Genetic Perturbation Platform – sgRNA Sequence Lookup. Cambridge (MA): Broad Institute. https://portals.broadinstitute.org/gpp/public/seq/search (Zuletzt abgerufen am 07.07.2025)
206. Thermo Fisher Scientific. BLOCK-iT™ RNAi Designer. Waltham (MA): Thermo Fisher Scientific. https://rnaidesigner.thermofisher.com/rnaiexpress/setOption.do?designOption=sirna (Zuletzt abgerufen am 07.07.2025)
207. National Center for Biotechnology Information (NCBI). Reference Sequence (RefSeq). Bethesda (MD): National Library of Medicine. https://www.ncbi.nlm.nih.gov/refseq (Zuletzt abgerufen am 07.07.2025)
208. Kibbe WA. OligoCalc: Oligonucleotide Properties Calculator. Chicago (IL): Northwestern University. http://biotools.nubic.northwestern.edu/OligoCalc.html (Zuletzt abgerufen am 10.03.2025)
209. Tjiang N, Zempel H. A mitochondria cluster at the proximal axon initial segment controls axodendritic TAU trafficking in rodent primary and human iPSC-derived neurons. *Cellular and Molecular Life Sciences* 2022; **79**(2): 120.
210. Schützmann MP, Hasecke F, Bachmann S, et al. Endo-lysosomal Aβ concentration and pH trigger formation of Aβ oligomers that potently induce Tau missorting. *Nature Communications* 2021; **12**(1): 4634.
211. Bell-Simons M, Buchholz S, Klimek J, Zempel H. Axonal Tau sorting depends on the PRR2 domain and 0N4R-specific interactions hint at distinct roles of Tau isoforms in synaptic plasticity. *bioRxiv* 2024: 2024.06.28.601286.
212. Alzforum. Therapeutics. https://www.alzforum.org/therapeutics (Zuletzt abgerufen am 07.07.2025)
213. Zempel H, Mandelkow E. Lost after translation: Missorting of Tau protein and consequences for Alzheimer disease. *Trends in Neurosciences* 2014; **37**(12): 721-32.
214. Petersen JD, Kaech S, Banker G. Selective microtubule-based transport of dendritic membrane proteins arises in concert with axon specification. *Journal of Neuroscience* 2014; **34**(12): 4135-47.
215. Oakley BR, Paolillo V, Zheng Y. γ-Tubulin complexes in microtubule nucleation and beyond. *Molecular Biology of the Cell* 2015; **26**(17).

216. Le Bras B, Fréal A, Czarnecki A, et al. In vivo assembly of the axon initial segment in motor neurons. *Brain Structure and Function* 2014; **219**(4): 1433-50.
217. Maniar TA, Kaplan M, Wang GJ, et al. UNC-33 (CRMP) and ankyrin organize microtubules and localize kinesin to polarize axon-dendrite sorting. *Nature Neuroscience* 2012; **15**(1): 48-56.
218. Zmuda JF, Rivas RJ. The Golgi apparatus and the centrosome are localized to the sites of newly emerging axons in cerebellar granule neurons in vitro. *Cell Motil Cytoskeleton* 1998; **41**(1): 18-38.
219. Acharyya D, Norman V. Amyloid Precursor Protein Can Cause Changes in Neuronal Firing Rates via Axon Initial Segment. *The Journal of Neuroscience* 2023; **43**(48): 8088.
220. Baj G, Patrizio A, Montalbano A, Sciancalepore M, Tongiorgi E. Developmental and maintenance defects in Rett syndrome neurons identified by a new mouse staging system in vitro. *Frontiers in Cellular Neuroscience* 2014; **8**(FEB).
221. Buchholz S, Linde J, Bell-Simons M, Spehr M, Zempel H, Zimmer-Bensch G. DNA Methyltransferase 1 (DNMT1) Shapes Neuronal Activity of Human iPSC-Derived Glutamatergic Cortical Neurons. *International Journal of Molecular Sciences* 2021; **22**.
222. Han Y, Hacker D, Donders BC, et al. Unveiling the cell biology of hippocampal neurons with dendritic axon origin. *Journal of Cell Biology* 2024; **224**(1): e202403141.
223. Wahle P, Sobierajski E, Gasterstädt I, et al. Neocortical pyramidal neurons with axons emerging from dendrites are frequent in non-primates, but rare in monkey and human. *eLife* 2022; **11**: e76101.
224. Gumy LF, Katrukha EA, Grigoriev I, et al. MAP2 Defines a Pre-axonal Filtering Zone to Regulate KIF1- versus KIF5-Dependent Cargo Transport in Sensory Neurons. *Neuron* 2017; **94**(2): 347-62.e7.
225. Hamdan H, Lim BC, Torii T, et al. Mapping axon initial segment structure and function by multiplexed proximity biotinylation. *Nature Communications* 2020; **11**(1).
226. Melton AJ, Palfini VL, Ogawa Y, et al. TRIM46 Is Required for Microtubule Fasciculation In Vivo But Not Axon Specification or Axon Initial Segment Formation. *The Journal of Neuroscience* 2024; **44**(42): e0976242024.
227. Huang Y-M, Zhang C, Ho T, et al. αII Spectrin Forms a Periodic Cytoskeleton at the Axon Initial Segment and Is Required for Nervous System Function. *The Journal of Neuroscience* 2017; **37**: 2112-17.
228. Lazarov E, Dannemeyer M, Feulner B, et al. An axon initial segment is required for temporal precision in action potential encoding by neuronal populations. *Science Advances* 2018; **4**(11): eaau8621.
229. Ichinose S, Ogawa T, Jiang X, Hirokawa N. The Spatiotemporal Construction of the Axon Initial Segment via KIF3/KAP3/TRIM46 Transport under MARK2 Signaling. *Cell Reports* 2019; **28**(9): 2413-26.e7.
230. Cai A, Lin Z, Liu N, et al. Neuroblastoma SH-SY5Y Cell Differentiation to Mature Neuron by AM580 Treatment. *Neurochemical Research* 2022; **47**.
231. Tosetti P, Taglietti V, Toselli M. Functional Changes in Potassium Conductances of the Human Neuroblastoma Cell Line SH-SY5Y During In Vitro Differentiation. *Journal of Neurophysiology* 1998; **79**(2): 648-58.
232. Chong ZX, Yeap SA-O, Ho WY. Transfection types, methods and strategies: a technical review. *PeerJ* 2021; **9**(2167-8359 (Print)).
233. Silverman MA, Kaech S, Jareb M, et al. Sorting and directed transport of membrane proteins during development of hippocampal neurons in culture. *PNAS* 2001; **98**(13).
234. Nelson A. Axonal Membranes and Their Domains: Assembly and Function of the Axon Initial Segment and Node of Ranvier. *Frontiers in Cellular Neuroscience* 2017; **11**.
235. Lamoureux P, Ruthel G, Buxbaum RE, Heidemann SR. Mechanical tension can specify axonal fate in hippocampal neurons. *Journal of Cell Biology* 2002; **159**(3): 499-508.
236. Schelski M, Bradke F. Neuronal polarization: From spatiotemporal signaling to cytoskeletal dynamics. *Molecular and Cellular Neuroscience* 2017; **84**: 11-28.
237. Mercken M, Fischer I, Kosik KS, Nixon RA. Three distinct axonal transport rates for tau, tubulin, and other microtubule-associated proteins: evidence for dynamic interactions of tau with microtubules in vivo. *The Journal of Neuroscience* 1995; **15**(12): 8259.

238. Bentley M, Banker G. The cellular mechanisms that maintain neuronal polarity. *Nature Reviews Neuroscience* 2016; **17**(10): 611-22.
239. Falzone TL, Gunawardena S, McCleary D, Reis GF, Goldstein LSB. Kinesin-1 transport reductions enhance human tau hyperphosphorylation, aggregation and neurodegeneration in animal models of tauopathies. *Human Molecular Genetics* 2010; **19**(22): 4399-408.
240. Falzone TL, Stokin GB, Lillo C, et al. Axonal stress kinase activation and tau misbehavior induced by kinesin-1 transport defects. *Journal of Neuroscience* 2009; **29**(18): 5758-67.
241. LaPointe NE, Morfini G, Pigino G, et al. The amino terminus of tau inhibits kinesin-dependent axonal transport: Implications for filament toxicity. *Journal of Neuroscience Research* 2009; **87**(2): 440-51.
242. Winckler B, Forscher² P, Mellman I. A diffusion barrier maintains distribution of membrane proteins in polarized neurons. *Nature* 1999; **397**(6721): 698-701.
243. Rao AN, Patil A, Black MM, et al. Cytoplasmic Dynein Transports Axonal Microtubules in a Polarity-Sorting Manner. *Cell Reports* 2017; **19**(11): 2210-9.
244. Hsu MT, Guo CL, Liou AY, et al. Stage-Dependent Axon Transport of Proteasomes Contributes to Axon Development. *Developmental Cell* 2015; **35**(4): 418-31.
245. Boecker CA, Olenick MA, Gallagher ER, Ward ME, Holzbaur ELF. ToolBox: Live Imaging of intracellular organelle transport in induced pluripotent stem cell-derived neurons. *Traffic* 2020; **21**(1): 138-55.
246. Harterink M, Edwards SL, de Haan B, et al. Local microtubule organization promotes cargo transport in C. elegans dendrites. *Journal of Cell Science* 2018; **131**(20): jcs223107-jcs.
247. Yogev S, Cooper R, Fetter R, Horowitz M, Shen K. Microtubule Organization Determines Axonal Transport Dynamics. *Neuron* 2016; **92**(2): 449-60.
248. Jakobs MAH, Zemel A, Franze K. Unrestrained growth of correctly oriented microtubules instructs axonal microtubule orientation. *eLife* 2022; **11**.
249. Kempf M, Clement A, Faissner A, Lee G, Brandt R. Tau binds to the distal axon early in development of polarity in a microtubule- and microfilament-dependent manner. *Journal of Neuroscience* 1996; **16**(18): 5583-92.
250. Xia D, Gutmann JM, Götz J. Mobility and subcellular localization of endogenous, gene-edited Tau differs from that of over-expressed human wild-type and P301L mutant Tau. *Scientific Reports* 2016; **6**(1): 29074.
251. de Leeuw SM, Davaz S, Wanner D, et al. Increased maturation of iPSC-derived neurons in a hydrogel-based 3D culture. *Journal of Neuroscience Methods* 2021; **360**.
252. Izsak J, Seth H, Andersson M, et al. Robust generation of person-specific, synchronously active neuronal networks using purely isogenic human iPSC-3D neural aggregate cultures. *Frontiers in Neuroscience* 2019; **13**(APR).
253. Ochalek A, Mihalik B, Avci HX, et al. Neurons derived from sporadic Alzheimer's disease iPSCs reveal elevated TAU hyperphosphorylation, increased amyloid levels, and GSK3B activation. *Alzheimer's Research and Therapy* 2017; **9**(1).
254. Hedegaard A, Monzón-Sandoval J, Newey SE, Whiteley ES, Webber C, Akerman CJ. Pro-maturational Effects of Human iPSC-Derived Cortical Astrocytes upon iPSC-Derived Cortical Neurons. *Stem Cell Reports* 2020; **15**(1): 38-51.
255. Volpato V, Webber C. Addressing variability in iPSC-derived models of human disease: Guidelines to promote reproducibility. *Disease Models & Mechanisms* 2020; **13**: dmm042317.
256. Huh CJ, Zhang B, Victor MB, et al. Maintenance of age in human neurons generated by microRNA-based neuronal conversion of fibroblasts. *eLife* 2016; **5**: e18648.
257. Mertens J, Paquola ACM, Ku M, et al. Directly Reprogrammed Human Neurons Retain Aging-Associated Transcriptomic Signatures and Reveal Age-Related Nucleocytoplasmic Defects. *Cell Stem Cell* 2015; **17**(6): 705-18.
258. Bocchi R, Masserdotti G, Götz M. Direct neuronal reprogramming: Fast forward from new concepts toward therapeutic approaches. *Neuron* 2022; **110**(3): 366-93.
259. Carter JL, Halmai J, Fink KD. The iNs and Outs of Direct Reprogramming to Induced Neurons. *Frontiers in Genome Editing* 2020; **2**.

260. Agholme L, Lindström T, Kågedal K, Marcusson J, Hallbeck M. An In Vitro Model for Neuroscience: Differentiation of SH-SY5Y Cells into Cells with Morphological and Biochemical Characteristics of Mature Neurons. *Journal of Alzheimer's Disease* 2010; **20**(4): 1069-82.
261. D'Aloia A, Pastori V, Blasa S, et al. A new advanced cellular model of functional cholinergic-like neurons developed by reprogramming the human SH-SY5Y neuroblastoma cell line. *Cell Death Discovery* 2024; **10**(1): 24.
262. Yusuf M, Leung K, Morris K, Volpi E. Comprehensive cytogenomic profile of the in vitro neuronal model SH-SY5Y. *Neurogenetics* 2012; **14**.
263. Krishna A, Biryukov M, Trefois C, et al. Systems genomics evaluation of the SH-SY5Y neuroblastoma cell line as a model for Parkinson's disease. *BMC Genomics* 2014; **15**(1): 1154.
264. Xie HR, Hu LS, Li GY. SH-SY5Y human neuroblastoma cell line: In vitro cell model of dopaminergic neurons in Parkinson's disease. *Chinese Medical Journal* 2010; **123**: 1086-92.
265. Radler MR, Spiliotis ET. Right place, right time - Spatial guidance of neuronal morphogenesis by septin GTPases. *Current Opinion in Neurobiology* 2022; **75**: 102557.
266. Millecamps S, Julien J-P. Axonal transport deficits and neurodegenerative diseases. *Nature reviews Neuroscience* 2013; **14**(3): 161-76.

# 7. Appendix

## 7.1. List of Figures



## 7.2. List of Tables

# 8. Publications / Vorabveröffentlichung von Ergebnissen

The results of this thesis have been partly published in the following publications:

| | **Contribution** | **Year** | **Status** | **Publication** |
|---|---|---|---|---|
| Article #1 | First Author | 2024 | Published | **Title**: Studying Microtubule Dynamics in Human Neurons: Two-Dimensional Microtubule Tracing and Kymographs in iPSC- and SH-SY5Y-Derived Neurons for Tau Research.<br>**Authors**: Allroggen N, Breuer H, Bachmann S, Bell M, Zempel H<br>**Journal**: Methods in Molecular Biology: Tau series<br>**Publisher**: Springer Nature<br>**DOI**: 10.1007/978-1-0716-3629-9_33<br><br>Reproduced with permission from Springer Nature. |
| Article #2 | First Author | 2024 | Published | **Title**: Axodendritic targeting of TAU and MAP2 and microtubule polarization in iPSC-derived versus SH-SY5Y-derived human neurons<br>**Authors**: Breuer H, Bell-Simons M, Zempel H<br>**Journal**: Open Life Sciences<br>**Publisher**: Walter de Gruyter<br>**DOI**: 10.1515/biol-2022-1010 |

| | | | | |
|---|---|---|---|---|
| Article #3 | Co-Author | 2025 | Published | **Title**: Tau axonal sorting and interaction with synaptic plasticity modulators is domain- and isoform-dependent in human iPSC-derived neurons<br>**Authors**: Bell-Simons M, Breuer H, Wunderlich L, Chmes H, Adam D, Klimek J, Buchholz S, Zempel H<br>**Journal**: Aging Cell<br>**Publisher**: Wiley<br>**DOI**: 10.1111/acel.70215 |